Dissertation

submitted to the

Combined Faculties for the Natural Sciences and for Mathematics

of the Ruperto-Carola University of Heidelberg, Germany

for the degree of

Doctor of Natural Sciences

presented by

Dipl.-Phys. Gerhard Brandt

born in Stuttgart (Baden-Württemberg)

Oral examination: 7 February 2007

Analysis of Events with Isolated Leptons

and Missing Transverse Momentum

in *ep* Collisions at HERA

Kurzfassung

Eine Studie von Ereignissen mit isolierten Leptonen und fehlendem Transversal-Impuls in ep Kollisionen wird vorgestellt. Im Standardmodell (SM) werden Ereignisse mit dieser Topologie vorwiegend durch Produktion reeller W Bosonen mit anschliessendem leptonischen Zerfall erwartet. In der vorliegenden Arbeit wird die Suche solcher Ereignisse im HERA-1 Datensatz fortgeführt, wo gegenüber der Erwartung im SM ein Überschuss an Ereignissen mit hohem hadronischen Transversal-Impuls $P_T^X > 25$ GeV gefunden wurde. Dieser Analyse werden neue Daten aus der HERA-2 Datennahmeperiode hinzugefügt. Der analysierte Datensatz von aufgezeichneten e^+p Kollisionen entspicht damit einer integrierten Luminosität von 220 pb^{-1}, was etwa doppelt so viel ist wie in HERA-1. Der e^-p Datensatz entspricht 186 pb^{-1}, was etwa dreizehnmal so viel ist wie in HERA-1.

Es wurden alle drei Lepton-Generationen (Elektronen, Myonen und Tau-Leptonen) analysiert. Im Elektron- und Myon-Kanal werden insgesamt 53 Ereignisse in 406 pb^{-1} beobachtet. Dies stimmt gut mit der Erwartung von 53.7 ± 6.5 Ereignissen im SM überein, die durch die Produktion reeller W Bosonen dominiert ist. Bei unterschiedlicher Ladung des Elektron-Strahls werden jedoch unterschiedliche Ereignisraten beobachtet. Während im e^+p Datensatz der Überschuss von Ereignissen mit $P_T^X > 25$ GeV nach wie vor besteht, stimmt der e^-p Datensatz mit der Erwartung im SM überein.

Im Tau-Kanal werden im gesamten HERA Datensatz 18 Ereignisse bei einer Erwartung von 20 ± 3 Ereignissen im SM beobachtet. Sie werden durch irreduziblen Untergrund aus geladenen Strömen dominiert. Der Anteil an reeller W Produktion beträgt dabei etwa 22%. Es wurde ein Ereignis mit $P_T^X > 25$ GeV bei einer Erwartung von 1.4 ± 0.3 Ereignissen im SM beobachtet.

Abstract

A study of events with isolated leptons and missing transverse momentum in ep collisions is presented. Within the Standard Model (SM) such topologies are expected mainly from production of real W bosons with subsequent leptonic decay. This thesis continues the analysis of such events done in the HERA-1 period where an excess over the SM prediction was observed for events with high hadronic transverse momentum $P_T^X > 25$ GeV. New data of the HERA-2 period are added. The analysed data sample recorded in e^+p collisions corresponds to an integrated luminosity of 220 pb^{-1} which is a factor of two more with respect to the HERA-1 analysis. The e^-p data correspond to 186 pb^{-1} which is a factor of 13 more with respect to HERA-1.

All three lepton generations (electrons muons and tau leptons) are analysed. In the electron and muon channels a total of 53 events are observed in 406 pb^{-1}. This compares well to the SM expectation of 53.7 ± 6.5 events, dominated by W production. However a difference in the event rate is observed for different electron beam charges. In e^+p data the excess of events with $P_T^X > 25$ GeV is sustained, while the e^-p data agree with the SM.

In the tau channel 18 events are observed in all HERA data, with 20 ± 3 expected from the SM. The events are dominated by irreducible background from charged currents. The contribution from W production amounts to about 22%. One event with $P_T^X > 25$ GeV is observed, where 1.4 ± 0.3 are expected from the SM.

Für Annika

Contents

Introduction

Events with high-P_T isolated leptons and missing transverse momentum in high-energy particle collisions are sensitive to new physics beyond the Standard Model (BSM) [1]. The observation of the first $ep \to \mu X$ event at HERA by the H1 experiment [2] at high $P_T^X = 76$ GeV where the SM expectation is small, has therefore created considerable interest in the high-energy physics community [3]. Since then, the search for isolated leptons has been continuously updated by the H1 [4, 5] and ZEUS [6, 7] collaborations as new data became available. At the end of the HERA-1 running period, a total of 19 events were observed by H1, with an SM expectation of 14.5 ± 1.6 events in a data sample corresponding to an integrated luminosity of 118.4 pb^{-1}. In the SM such events are mostly expected from production of real W bosons with subsequent leptonic decay. Overall the distributions of the events were compatible with W production in the SM. However, 11 of these events were observed at $P_T^X > 25$ GeV, where the SM expectation is only 3.4 ± 0.4. This observation, corresponding to an excess of almost 3σ significance, was considered HERA's best chance for the discovery of new physics. The most popular model to explain such an excess is anomalous single *top* production via flavour changing neutral currents (FCNC). The events were analysed to test this assumption, trying to separate contributions from W boson production and single *top* production [8, 9]. In H1, 5 of the events were considered compatible with a *top* decay rather than a SM W decay in a region where 1.3 ± 0.2 events were expected within the SM. In absence of a clear signal for *top* production exclusion limits were set, significantly improving the constraints obtained from other colliders [10, 11, 12].

Due to lepton universality in the SM the tau channel is expected to behave identical to the electron and muon channels. It therefore presents an important cross check even though a search for events with hadronic tau decays and missing transverse momentum is more challenging than the electron and muon channel. The extraction of a significant signal is difficult due to a large background from the hadronic final state. In the HERA-1 data taking period, ZEUS reported 3 tau candidates with 0.4 ± 0.1 expected [13]. Two of these were seen at high $P_T^X > 25$ GeV where only 0.2 ± 0.05 were expected. H1 reported a total of 6 tau candidates, while 9.9 ± 2.7 are expected from the SM [14]. None of these events was seen at high P_T^X. Like the electron and muon channels, the tau channel is being constantly updated as new data become available [15].

The HERA-2 data include a large e^-p data sample of 186 pb^{-1} which is about 13 times as big as the HERA-1 e^-p data sample. For this thesis, the complete e^-p data was available and could be analysed. A HERA-2 e^+p sample of 113 pb^{-1} could be analysed, which is about the same amount as available in HERA-1. Data taking is still going on for the e^+p data. At the current rate, another sample of ~ 100 pb^{-1} can be hoped for at the end of the HERA programme. The current status of the search for isolated electron, muon and tau leptons is discussed in the present work.

1. Physics Processes

1.1. Introduction

A physics process that leads to energetic leptons and genuine missing transverse momentum due to undetected particles in the final state is considered as signal in the present analysis. Other processes, where a lepton is imitated or an apparent imbalance detected due to fluctuations in the measurement are called backgrounds.

The signal processes considered in this analysis are production of real W and Z^0 bosons in the SM and any possible BSM process with a similar signature. As template for such a BSM process the production of single *top* quarks via FCNC is used. All cuts are designed to maximise acceptance for these processes. All other processes are considered background. The most important SM backgrounds are neutral and charged currents in deep inelastic scattering (DIS) and jets in photoproduction because of their large cross sections. The event sample is selected in a phase space with missing transverse momentum $P_T^{\mathrm{miss}} > 12$ GeV and high lepton transverse momentum $P_T^l > 10$ GeV, where the expectation for the SM background processes is already low. In this region, the normalisation of the background processes is controlled using dedicated control samples.

1.2. Signal Processes

1.2.1. W and Z^0 Production

The main source for events with isolated leptons and missing transverse momentum is the production of real W bosons

$$ep \rightarrow eWX$$

Decay Channel	Branching Ratio	Signature
$W \rightarrow e\nu_e$	10.7%	$e + P_T^{\mathrm{miss}}$
$W \rightarrow \mu\nu_\mu$	10.6%	$\mu + P_T^{\mathrm{miss}}$
$W \rightarrow \tau\nu_\tau \hookrightarrow h\bar{\nu}_\tau$	$11.2\% \cdot 50\%$	τ-jet$+P_T^{\mathrm{miss}}$
$W \rightarrow q\bar{q}$	67.96%	2 jets

Table 1.1.: W boson decay modes. All leptonic decay modes are covered in this thesis. $\tau \hookrightarrow h\bar{\nu}_\tau$ denotes hadronic 1-prong tau decays. Values taken from [16].
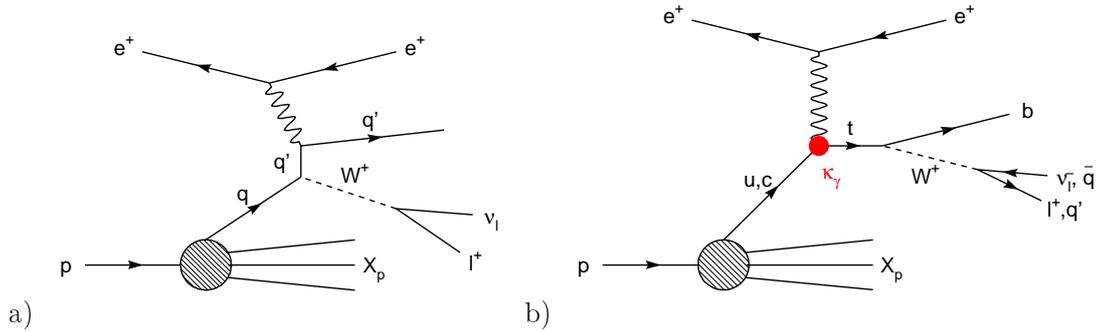
Figure 1.1.: Signal processes in the search for events with isolated leptons and missing transverse momentum. a) Real W production in the SM via resolved photoproduction. b) Anomalous single *top* production via FCNC, used as template for events from BSM processes with large hadronic transverse momentum P_T^X.

with subsequent leptonic decay of the W boson [17]. Table 1.1 recalls the W decay channels. Real W production proceeds mostly via resolved photon interactions in photoproduction, where the transverse momentum of the W boson P_T^W is typically small. In the production via direct photon interactions P_T^W may be larger. The transverse momentum of the decay lepton is large due to the large W mass, while the transverse momentum of the hadronic final state P_T^X is typically small.

The total cross section for real W production is about 1.3 pb at $\sqrt{s} = 319$ GeV. All contributions to the process are modelled in the framework of the EPVEC event generator [18]. In Fig. 1.1a the radiation of a W boson off the scattered quark is shown, which is the dominant contribution to the total cross section. All eight leading order diagrams, including W radiation off the final state quark, W radiation off the initial and final state lepton, triple boson coupling ($WW\gamma$ vertex) and boson gluon fusion are taken into account. A smaller contribution of less than 7% to the total cross section from charged current W production $ep \to \nu W X$ is also taken into account.

Next-to-leading order (NLO) QCD corrections are also calculated [19]. The theoretical uncertainty of 30% in leading order is reduced to 15%. The corrections are applied by weighing generated EPVEC events by a factor that depends on P_T^W and the rapidity of the W boson, such that the resulting cross section corresponds to the NLO calculation [20]. The effect on the leading order cross section is found to be 30% at low P_T^W and 10% at high P_T^W.

Also Z^0 boson production $ep \to eZX$ with subsequent decay $Z^0 \to \nu\bar{\nu}$ is included where the Z^0 is produced via Z^0-strahlung or the Cabbibo-Parisi-process. The contribution to the signal rate is less than 3% calculated using the EPVEC generator [21].

Subsequent decays of the W boson to leptons $W \to l\nu$ and hadrons $W \to q\bar{q}$ are covered in the event generation. Final state parton showers are simulated in the PYTHIA framework [22].

1.2.2. Anomalous Single *top* Production

Anomalous Single *top* production via FCNC shown in Fig. 1.1b is one of the most prominent candidates for explaining an excess over the SM prediction of events with an isolated lepton

and large P_T^X. Throughout this thesis, this process is used as template for any BSM process with this final state. While single *top* production is allowed kinematically and possible within the SM at HERA, the cross section is too low to see a signal in the available data samples. An observation would therefore hint at new physics. Anomalous *top* production is modelled with the ANOTOP event generator [23]. ANOTOP uses matrix elements of the complete process $e + q \rightarrow e + t \rightarrow e + b + W$ obtained from the CompHEP program [24]. The shape of kinematical distributions of ANOTOP events is used where appropriate to optimise the acceptance of such events.

1.3. Background Processes

1.3.1. Deep Inelastic Scattering

The most prominent background processes at HERA are neutral currents (NC)

$$ep \rightarrow eX$$

and charged currents (CC)

$$ep \rightarrow \nu X$$

in deep inelastic scattering (DIS) in the SM framework. Figure 1.2 shows the general kinematics of DIS and the notation used in this thesis. The Feynman diagrams for NC and CC processes are shown in Figs. 1.3a and 1.3b, respectively. In NC either a photon or Z^0 boson is exchanged between the incident electron and the scattered quark. In charged currents (CC) a (virtual) W boson is exchanged.

The kinematics of a NC event at high Q^2 can be reconstructed most precisely with the electron method as described in table 1.2. A NC final state consists of the scattered electron and a jet from the scattered quark. At high Q^2 the scattered electron has typically high transverse momentum and is isolated from the hadronic final state. In the transverse plane the electron and the jet are back-to-back due to momentum conservation. Second jets are possible due to radiation of hard gluons in the final state. Missing energy in the event can only be produced by fluctuations in the energy measurement of the detector response and limited geometric acceptance (energy losses close to the beam pipe and in the calorimeter cracks).

A CC final state consists of a single jet and real missing energy from the neutrino which escapes undetected. Additional jets are possible due to NLO contributions to the cross section, like in Fig. 1.3c. Also photons can be radiated in the final state. These additional jets, radiated photons or other hadrons in the final state can be misidentified as leptons. The kinematics of a CC event have to be reconstructed using the hadron method as described in table 1.2.

NC and CC processes in DIS are modelled with the DJANGO [26] and RAPGAP [27] event generators in the region $Q^2 > 4$ GeV. DJANGO is used to model DIS events in the electron and muon channels. In these channels the background can be estimated from the inclusive distributions. In the tau channel RAPGAP is used because it was found to better describe dijet topologies which are an important background there. To correct for remaining deficiencies in the simulation of multi-jet topologies a "k-factor" weight of $(1. + 0.2 * (n_{jet} - 1))$ is applied to all RAPGAP events, where n_{jet} is the number of reconstructed jets in the event.

Kinematics of Deep Inelastic Scattering
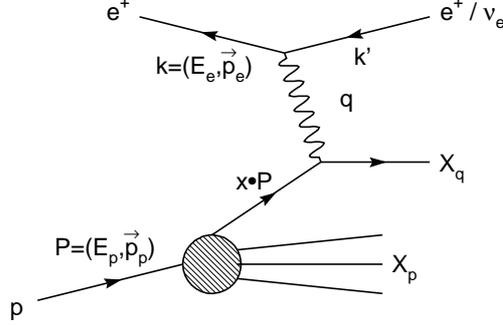
Incident electron	$k = (E_e, \vec{p_e})$
Incident proton	$p = (E_p, \vec{p_p})$
Scattered electron	$k' = (E'_e, \vec{p'_e})$
Hadronic final state	$X \quad (X^2 = (q+p)^2 \approx q^2 + ys)$
Total momentum balance	$k + p = k' + X$

Centre-of-mass energy (squared)	$s = (k+p)^2 \approx 2pk = 4E_pE_e$
Momentum transfer	$q = k - k' = X - p \ (Q^2 = -q^2 \approx sxy)$
Inelasticity y	$y = \frac{p \cdot q}{p \cdot k} \approx \frac{2pq}{s}$
Bjorken-x	$x = \frac{-q^2}{2p \cdot q} = \frac{Q^2}{ys}$
Inclusive hadronic angle	$\gamma_h = 2\arctan(\frac{E_X - P_z^X}{P_T^X})$

Figure 1.2.: Kinematic observables of DIS. The notation in this figure is used throughout this thesis.

Method	Q^2	y	Resolution
Hadron	$Q_h^2 = \frac{pt_h^2}{1-y_h}$	$y_h = \frac{E_h - p_z^h}{2E_e}$	$\frac{\delta Q_h^2}{Q_h^2} \sim \frac{1}{1-y_h}$
Electron	$Q_e^2 = 2E_e E'_e(1 + \cos\theta)$	$y_e = 1 - \frac{E'_e}{E_e}\sin^2\frac{\theta}{2}$	$\frac{\delta y_e}{y_e} \sim \frac{1}{y_e}$
Double Angle	$Q_{DA}^2 =$ $\frac{4E_e^2 \sin\gamma_h(1+cos\theta_e)}{\sin\gamma_h + \sin\theta_e - \sin(\theta_e + \gamma_h)}$	$y_{DA} =$ $\frac{\sin\theta_e(1 - \cos\gamma_h)}{\sin\gamma_h + \sin\theta_e - \sin(\theta_e + \gamma_h)}$	$\frac{\delta\gamma_h}{\sin\gamma_h} \oplus \frac{\delta\theta_e}{\sin\theta_e}$

Table 1.2.: Reconstruction Methods for the kinematics of DIS events [25]. Bjorken-x is derived from y, Q^2 via $x = Q^2/s$. The notation in this table is used throughout this thesis.
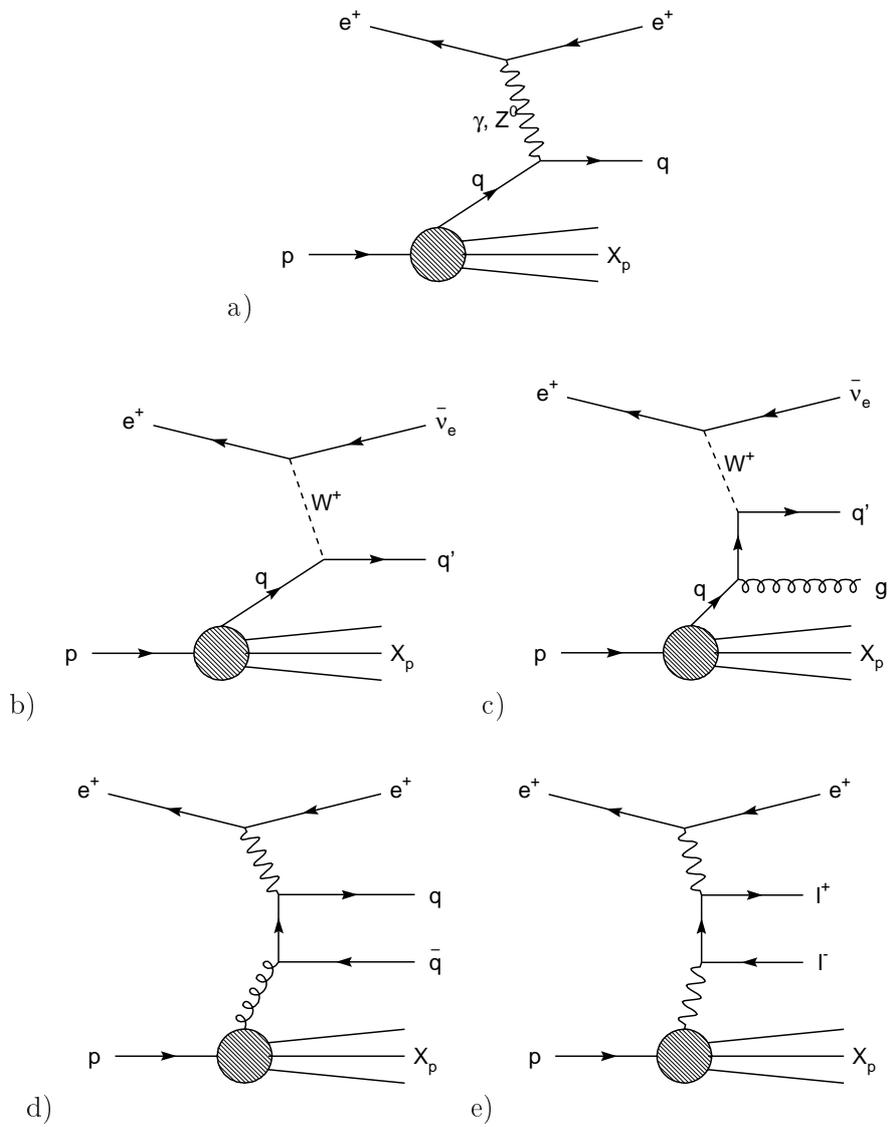
Figure 1.3.: The main SM background processes to events with isolated leptons and missing transverse momentum. a) Neutral current in DIS; b) Charged current in DIS; c) Charged current dijets in DIS; d) Dijets in photoproduction; d) Lepton pair production.

1.3.2. Photoproduction

Jets can be produced in hard scattering photoproduction processes via boson-gluon-fusion as shown in Fig. 1.3d. The scattered electron leaves the main detector undetected along the beam-pipe. The topology of photoproduction events consists of two jets back-to-back in the transverse plane. Additional jets are possible due to contributions from NLO processes. Photoproduction events may enter the isolated leptons selection because of missing energy due to fluctuations in the detector response and limited acceptance, and because of misidentification of a jet as isolated lepton.

Jets in Photoproduction are modelled with the PYTHIA 6.1 event generator [22] in the regime $Q^2 < 4$ GeV. Because the cross section of LO and NLO photoproduction processes is not so well known, "k-factors" were estimated from a photoproduction sample (described in section A.3). For every jet a factor $(1. + 0.2 * n_{jet})$ is applied to the event, where n_{jet} is the number of jets in the event in agreement with previous studies [28]. To account for a further observed deficiency of PYTHIA to simulate jets with low transverse momentum in the forward region, an additional correction factor of 1.4 is applied to events where the highest jet transverse momentum is below 15 GeV.

1.3.3. Lepton Pair Production

Lepton pair production proceeds mainly via $\gamma\gamma$-interactions in the SM as shown in Fig. 1.3e. The final state of lepton pair production consists of up to three isolated leptons, with a possible hadronic final state from the proton remnant, depending on the kinematic region (elastic or inelastic). If one of the leptons is not detected and a fluctuation affects the energy measurement, the event may enter the selection due to the real lepton and the apparent missing energy. Pair production of leptons is modelled with the GRAPE event generator [29]. GRAPE is based on a full calculation of all electroweak diagrams (including Drell-Yan-processes and Z^0-bremsstrahlung) taking into account intermediate photons and final state interferences. All three lepton generations are considered.

1.3.4. Wide-Angle Bremsstrahlung

QED Compton scattering leads to events with photons in the detection region $1° < \theta_\gamma < 178°$ in elastic $ep \to ep\gamma$ or inelastic $ep \to eX\gamma$ events called wide-angle bremsstrahlung (WAB). WAB can contribute to the background due to misidentification of the photon as a lepton together with apparent missing transverse momentum from fluctuations in the measurement. It is modelled with the WABGEN event generator [30]. Radiation corrections to the incident electron, the value of the electron mass and the structure of the proton are taken into account.

2. Experimental Conditions

2.1. The HERA Accelerator

The HERA (Hadron Elektron Ring Anlage) at DESY, Hamburg is the worlds unique ep collider. It started operation in 1992 and is scheduled to end operation in July 2007. HERA consists of an electron[1] accelerator and a proton accelerator with a circumference of 6.3 km. A schematic drawing of the accelerator complex is shown in Fig. 2.1. Particles are collided with a centre-of-mass energy of 319 GeV (300 GeV before 1997). The beams are organised in up to 220 particle bunches crossing every 96 ns.

HERA running is divided in the HERA-1 period from 1994 to 2000 and the HERA-2 period from 2003 to 2007. A machine upgrade was performed for HERA-2. The luminosity was increased by installing quadrupole focusing magnets close to the interaction points within H1 and ZEUS. Spin rotators were installed to provide the interaction regions with a longitudinally polarised electron beam.

A new feature at HERA-2 is the possibility to deliver a longitudinally polarised electron beam in the interaction regions. The longitudinal polarisation P_e of the electron beam is defined as $P_e = (N_R - N_L)/(N_R + N_L)$ where N_R (N_L) is the fraction of right (left) handed electrons. The magnitude of the polarisation generally increases with beam lifetime and the helicity is flipped every few weeks to get positive and negative polarisation values. Figure 2.2 shows the polarisation profiles for the analysed HERA-2 periods. The profiles are taken from runs where polarisation measurement was available and normalised to unit area.

2.2. The H1 Experiment

This section outlines the H1 detector, highlighting components important for the analyses discussed in this thesis, focusing on the HERA-2 setup. The setup of the H1 detector in HERA-1 is described in [31]. A drawing of the H1 detector is shown in Fig. 2.3. H1 is a general purpose detector to study ep collisions. The nominal interaction point is the origin of the H1 coordinate system. The z-axis is the nominal beam axis. It is negative in the backward (electron beam) direction, and positive in forward direction. All polar angles θ are defined with respect to the forward direction. Because the centre-of-mass system of the ep collision is boosted along the proton direction, the H1 detector is better equipped in the forward direction. Particularly, the calorimetry is more finely segmented in that area. The detector is designed to provide coverage over most of the 4π solid angle, thus being able to measure the total visible energy in each event. This ability is impaired by energy lost close to

---

[1] HERA can run with electrons or positrons. Unless explicitly stated *electron* refers to electrons and positrons in this thesis.
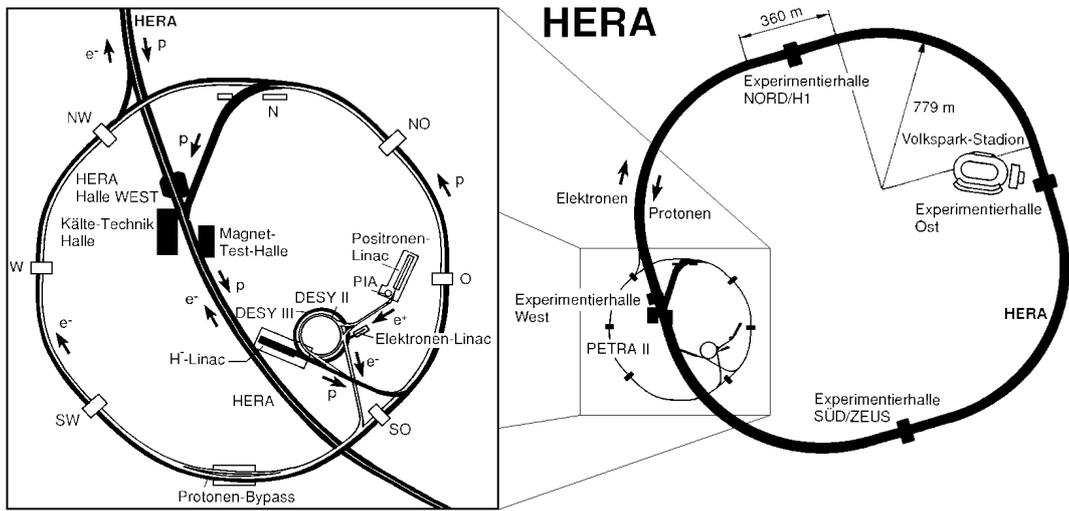
Figure 2.1.: The HERA accelerator complex.

| 2003-04, e^+p | 2004-06, e^-p | 2006, e^+p |

$\bar{P}_e = 0\%$ $\bar{P}_e = -6\%$ $\bar{P}_e = +29\%$
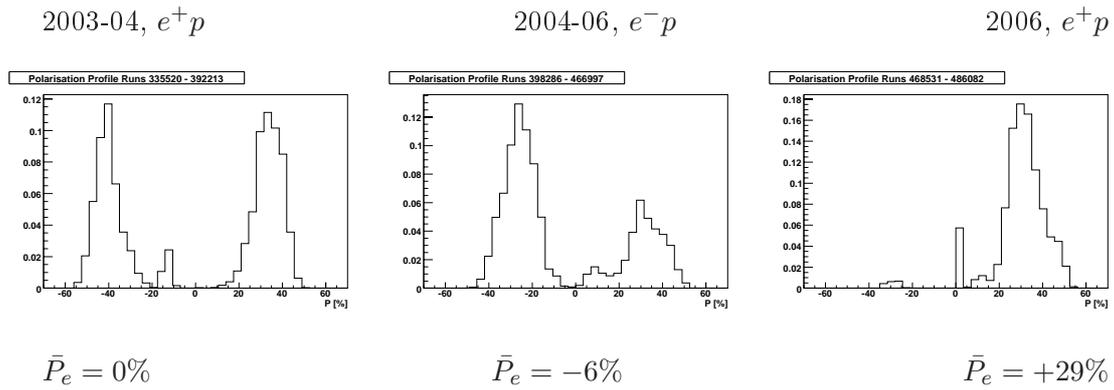
Figure 2.2.: Longitudinal electron beam polarisation profiles for the analysed HERA-2 running periods. The average polarisation $\bar{P}_e$ for each period is indicated below.
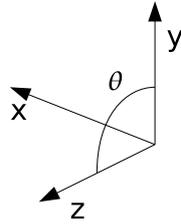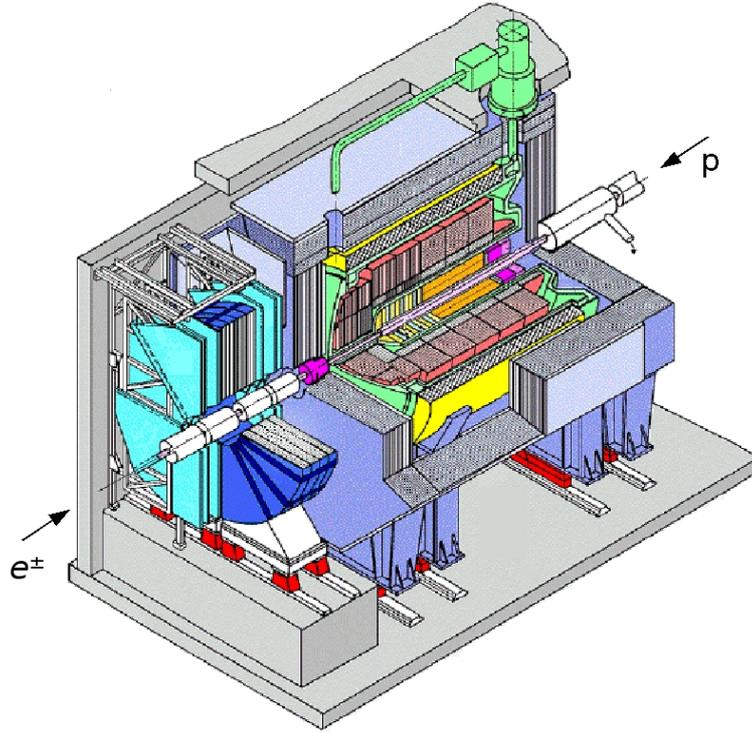
Figure 2.3.: The H1 Detector. The origin of the H1 coordinate system is in the centre of the tracking chambers (orange). Visible sub-detectors are the LAr calorimeter (red), SpaCal (pink), instrumented iron (violet) and forward muon system (turquoise).

the beam pipe, in calorimeter cracks and dead material in front of the calorimeter, particularly in the forward direction.

The pseudo-rapidity is defined as $\eta = -\ln \tan(\theta/2)$. A very common measure for distances between two objects is their distance in the $\eta\varphi$-plane defined as

$$D_{\eta\phi} = \sqrt{\Delta\eta^2 + \Delta\varphi^2}$$

where $\Delta\eta$ and $\Delta\varphi$ are the difference in pseudo-rapidity η and azimuthal angle φ of the two object's four-vectors.

2.2.1. Tracking Detectors

The tracking system is used for triggering, final state reconstruction and particle identification. A drawing of the layout of the central tracking detectors in HERA-2 is shown in Fig. 2.4. A superconducting coil surrounding the LAr calorimeter cryostat produces a magnetic field of 1.16 T strength along the z-axis which bends charged particle trajectories and allows measuring their transverse momentum.

The main subdetectors of the central tracking detector CTD are the central jet chambers CJC covering the polar angle range $10° < \theta < 170°$. Single measurement points (hits) are resolved with a resolution of $170\,\mu$m in the transverse plane, and 2.2 cm in the z-direction. The momentum resolution is $\sigma_p/p < 0.01\,p/$GeV. The forward tracking detector FTD covers the polar angular range $7° < \theta < 25°$. It provides additional information for charged particles detected in the forward part of the calorimeter. Trigger information is provided by the central and forward inner proportional chambers.

2.2.2. Calorimeters

The energy of hadrons and electromagnetic particles in the final state is measured in the forward and barrel regions by a LAr calorimeter [32]. The LAr calorimeter covers the polar angle range $4° < \theta < 154°$. A profile of the LAr calorimeter is shown in Fig. 2.5. The upper half shows the segmentation of the calorimeter in barrels. The lower half shows the segmentation in individual cells. It contains an electromagnetic section made of lead plates with a depth corresponding to 20–30 radiation lengths, depending on the polar angle. A hadronic section made of steel plates with a depth corresponding to 4.5–8 interaction lengths surrounds it in the same cryostat. For electromagnetic showers the energy resolution of the calorimeter measured in a test beam was $\sigma_E/E = 12\%/\sqrt{E(\mathrm{GeV})} \oplus 1\%$ and for hadronic showers $\sigma_E/E = 50\%/\sqrt{E(\mathrm{GeV})} \oplus 2\%$ [33]. The LAr calorimeter can also provide a time estimate of energy deposits. This can be used to identify energy deposits not in time with the bunch crossing time T_0. A tail catcher made of cathode pads on the inner face of the surrounding iron yoke measures particles not stopped by the LAr calorimeter. The backward region is covered by a lead-fibre spaghetti calorimeter SpaCal [34]. It allows the precise measurement of the scattered electron in the polar angular range $153° \leq \theta \leq 177.5°$.

2.2.3. Muon Detectors

Muons escaping the calorimeter are detected by the central muon detector CMD (or instrumented iron) and the forward muon detector FMD [35]. The CMD consists of 10 layers of limited streamer tubes embedded between sheets of iron of the magnetic flux return yoke, and 6 layers of pad and strip detectors. The FMD consists of 6 double layers of drift chambers on the faces of a toroid magnet in front of the iron yoke endcap. The CMD covers an angular range of $5° < \theta < 175°$, and the FMD covers $3° < \theta < 17°$. The momentum measurement of the CMD is poor and the CTD momentum is used for muons reconstructed in the central region. For muons detected in the FMD the momentum resolution is $\sigma_p/p = 24\% - 36\%$ for $p = 5 - 200$ GeV.
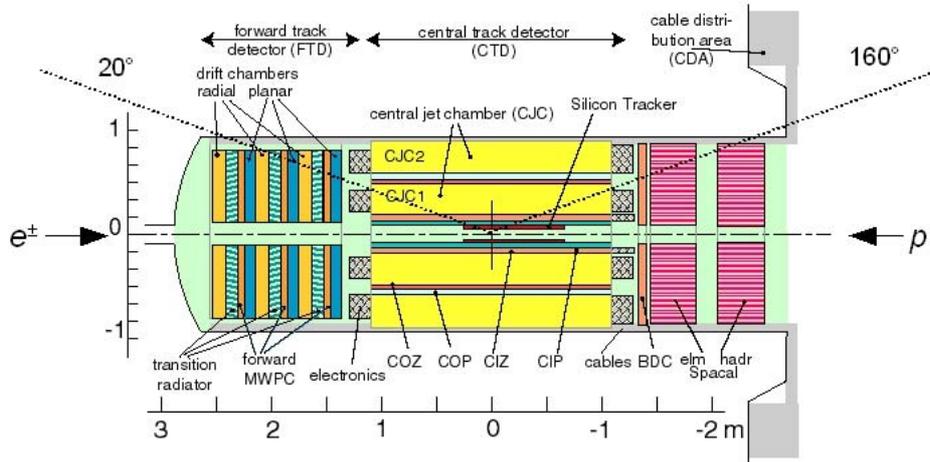
Figure 2.4.: Overview of H1 tracking detectors. The main detectors are the central jet chambers CJC1 and CJC2 (yellow). Trigger information is provided by the CIP.
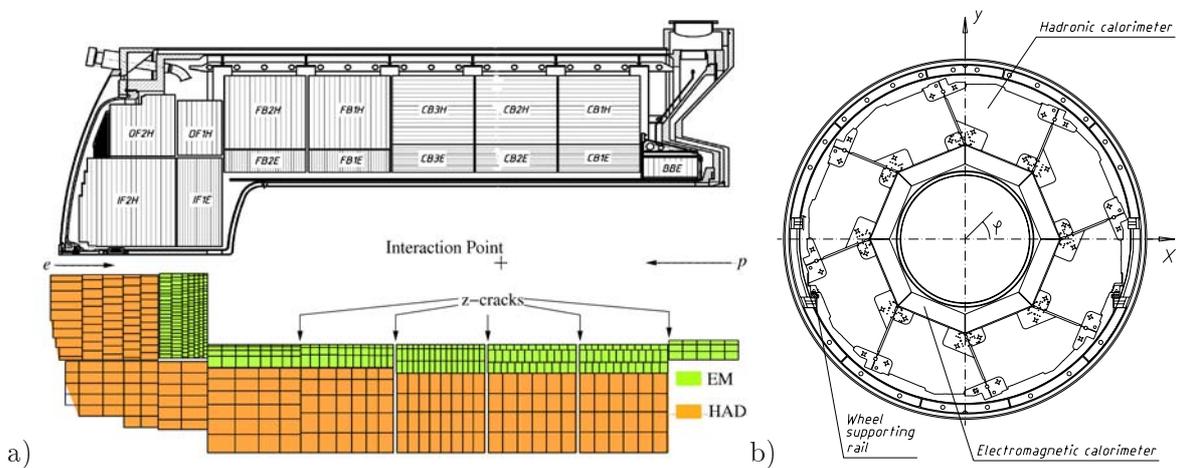
Figure 2.5.: Profiles of the LAr calorimeter. a) Longitudinal profile. The top half shows the division in calorimeter barrels. The bottom half shows the calorimeter as seen in the event display. Individual cells are visible. b) Transverse profile of a calorimeter barrel. Each barrel is composed of octants.

2.2.4. Luminosity

The luminosity delivered by HERA to H1 is determined from the rate of the Bethe-Heitler process $ep \rightarrow e\gamma p$. In the HERA-2 setup of the luminosity system the rate of photons with an energy greater than 10 GeV is measured in a photon detector. The systematic uncertainty on the luminosity measurement is dominated by the geometric acceptance of this photon detector. After offline corrections the total systematic error on the luminosity measurement is 2% in HERA-2.

2.2.5. Trigger and Data Acquisition

Triggering and Data Acquisition DAQ are realised in a multilayer system. The event rate of $\sim$100 kHz is reduced to a readout frequency of $\sim$47-50 Hz. Data from the subdetectors is constantly read into a pipeline. On the first trigger level L1 hardware trigger elements are combined by the central trigger logic into subtriggers. If a subtrigger fires, the readout is stopped. The decision to pass the event on is taken within 2.3 μs. If trigger rates are above their respective bandwidth budget, they are prescaled. That means only every n-th event is accepted if n is the prescale factor of the respective subtrigger. Most triggers used in high-P_T analyses, such as those in this thesis, are not prescaled. The second trigger level (L2) consists of the Level 2 Topological Trigger (L2TT) and the Level 2 Neural Network Trigger (L2NN). These are devices capable of making more informed trigger decisions based on topological information in the $\eta\varphi$-plane or on neural network decisions, respectively. The decision to pass the event on to the next level is made within 20 μs. The third trigger level (L3) can be used to make detailed track-based trigger decisions. The rate after L2/3 is called the L4 input rate and is around 40 Hz. The fourth trigger level (L4) is implemented on a computer farm outside the DAQ hardware. It reconstructs the complete event in software and assigns it to one or more event classes. It can take a decision in about 100 ms, reducing the event rate of finally selected events to about 10 Hz. These events are stored persistently on tape and are available for offline analysis.

2.2.6. Software

The H1 detector response to the events generated by the Monte Carlo programs is simulated in H1SIM, a software based on GEANT [36]. The simulated events are then subjected to the same reconstruction and analysis chain as the data. The reconstruction software H1REC is FORTRAN based and stores its output in BOS (bank object storage) format. All information on the event can be accessed via BOS banks. The analysis part of the software has been completely rewritten in C++ for HERA-2 [37] and is based on ROOT [38].

3. Final State Reconstruction

3.1. Introduction

The final state reconstruction algorithm uses detector measurements to evaluate the four-vectors of the final state particles. From these four-vectors the global kinematics are determined. The reconstruction begins with tracks measured in the tracking detectors and clusters of calorimetric energy deposits in the calorimeters. First electromagnetic particles (electrons and photons) and muons are identified. Electromagnetic particles are defined by compact isolated electromagnetic clusters. For muons, signals in the muon detectors are required. The remaining information is associated to hadrons. Clusters are combined with tracks to form hadron candidates. Non-isolated electromagnetic particles and muons are attributed to hadron decays and included in the hadronic final state. Hadronic final state particles are combined into jets. Finally, the energy scale of electrons and jets is calibrated. Using the fully reconstructed and calibrated final state, global event observables may be measured, for instance missing transverse momentum using the total four-vector sum of all identified particles.

Hadronic tau decays are identified via their decay products, called tau jet. Tau jets are defined based on calibrated jets and matching isolated tracks. Their identification is described in section 6.3.

3.2. Clusters

Clusters are reconstructed from neighbouring calorimeter cells with energy significantly above the noise threshold of 300 MeV. Cells not associated to clusters are suppressed to reduce noise. Clusters are defined to be electromagnetic or hadronic, depending in which section of the calorimeter they are predominantly found. The energy scale of the clusters is then corrected by factors $E_h/E_{em} \simeq 1.1 - 1.3$ typical for non-compensating calorimeters. Finally dead material corrections based on the calorimeter geometry are applied. The cluster energy still needs to be calibrated relatively between data and simulation, and shifted to the correct absolute energy scale to correctly determine the invariant masses of measured particles. These steps are carried out after jet reconstruction. Cluster four-vectors are defined on an axis through the vertex and the barycentre of the cluster.

3.3. Tracks

For track reconstruction multiple fits and tracking detector combinations are used:

- Non-vertex-fitted tracks are stored in the DTNV bank. These tracks can be short, making the momentum measurement and even direction uncertain.

- Vertex-fitted tracks are stored in the DTRA bank. These are reconstructed from DTNV tracks after a common fit to the event vertex. There can be two DTRA track hypotheses for one DTNV track, or the DTRA track can be very far away from the original DTNV track.

- Good quality tracks are selected from vertex-fitted tracks. Selected tracks are preferably used for lepton identification and are the only tracks used in the hadronic final state reconstruction. Tracks are good quality if they meet the following requirements:

  - $p_T > 70$ MeV,
  - $|\text{dca'}| \cdot \sin(\theta) \leq 2$ cm,
  - $R_{start} \leq 50$cm,
  - $R_{length} \geq 10$ cm for $\theta \leq 150°$ and
  - $R_{length} \geq 5$ cm for $\theta > 150°$

    where p_T is the transverse momentum of the track, θ the polar angle, dca' the distance of closest approach to the vertex in the transverse plane, R_{start} the track start radius from the nominal vertex position and R_{length} the length of the measured track segment in the transverse plane.

Tracks are calibrated during reconstruction, and no further calibration is applied at the analysis level. The error Δm_{K^0} on the K^0 invariant mass m_{K^0} reconstructed from $K^0 \to \pi^+\pi^-$ is directly proportional to the error on track momentum Δp. The deviation of m_{K^0} from the PDG value is less than 1% in the current software giving confidence that the track momentum is reliably measured [39].

The track efficiency is determined with NC events by the ratio of events where a track is required for the scattered electron to events where no track is required. It is measured in different detector regions and it was found that the simulation overestimates the tracking efficiency. To correct for this, tracks are rejected randomly from Monte Carlo events to correct the agreement of data and Monte Carlo track multiplicities. The probability to identify a track rises linearly from $\sim 50\%$ for $\theta_{track} \simeq 15°$ to a maximum of 95% at $\theta_{track} \simeq 30°$. A dependence of a difference in track efficiency on the track transverse momentum is neglected.

3.4. Electromagnetic Particles

3.4.1. Identification

Electromagnetic particles are identified as compact and isolated electromagnetic clusters in the LAr calorimeter [40]. They are reconstructed starting from seed clusters with an energy above 2 GeV of which at least 90% must be contained in the LAr calorimeter, and with an electromagnetic energy fraction of at least 50%. Around these seed clusters a shower envelope is defined by a cone of 7.5° opening around the cluster axis. Neighbouring clusters are merged to the seed cluster if at least 50% of their energy is contained in the shower envelope. The resulting total electromagnetic particle cluster candidate has to have a transverse momentum above 3 GeV and a total energy $E > 5$ GeV. The shower has to be spread over at least three calorimeter cells to avoid that single "hot" calorimeter cells, produced by noise in the readout electronics are misidentified as electromagnetic particles. The electromagnetic energy fraction $f_{em} = E_{em}/E$ must be $f_{em} \gtrsim 95\%(\theta)$[1]. Compactness is ensured by requiring the transverse cluster radius to be $\sigma_R \lesssim 5(\theta)$ cm. Also the energy fraction of the "hot core", defined by the energy E_{hot} of the $N = 4(\theta)$ hottest cells around the most energetic cell, has to be at least $50\%(\theta)$. Isolation against other clusters is ensured by defining an isolation cone with radius $R_{iso} = 0.25$ in the $\eta\varphi$-plane around the cluster axis, and requiring at least 98% of the total energy to be contained in this cone. If the hadronic energy in the isolation cone is less than 300 MeV at least 95% of the total energy has to be contained in the cone. If all these criteria are met, the total cluster four-vector defines the electromagnetic particle four-vector.

The electromagnetic particle is defined to be isolated against hadrons, if the energy in an isolation cone of $R_{iso}^{had} = 0.5$ in the $\eta\varphi$-plane around the particle is less than 3% of the total energy. In this case, the electromagnetic particle is excluded from the hadronic final state.

The isolated electron with the highest energy is taken to be the scattered electron and can be used to determine the event kinematics using the electron method shown in Tab. 1.2. In the electron channel, the isolated electron with the second highest energy is defined to be the scattered electron because the highest energy electron is assumed to come from the W-decay.

Tracks are associated to electromagnetic particles by requiring a track-cluster match. All selected, vertex-fitted and non-vertex-fitted tracks are tested to match the cluster. A track matches if the closest distance of approach between the extrapolated LAr calorimeter face impact position of the track and the centre-of-gravity of the electromagnetic particle is less than 12 cm. If a matching track is found, the charge of the electron is determined from the track curvature direction. The error on the curvature is used as the charge measurement significance. If no matching track is found, the electromagnetic particle is considered a photon.

Another algorithm is used to identify electrons in the SpaCal. It is based on clusters detected in the SpaCal with an energy greater than 5 GeV and a radius of less than 4 cm. All electromagnetic particles found by these algorithms are considered and called electron candidates in the following.

The identification efficiency for electromagnetic particles with a transverse momentum $P_T > 10$ GeV is close to 100%. The trigger efficiency was shown to be around 98% using NC events [41].

---

[1] Here and in the following the "(θ)" reminds that the requirements are optimised as a function of the polar angle of the electron candidate and only a typical numerical value is given.
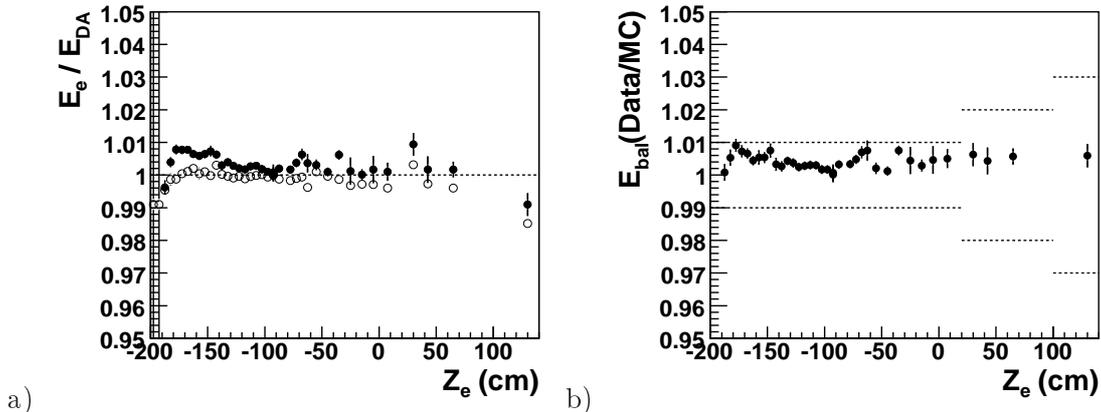
Figure 3.1.: Test of the electron calibration. Shown are tests in an inclusive NC sample for the 2005 e^-p data. a) The ratio $E_{\mathrm{bal}} = E_e/E_{\mathrm{DA}}$ of the calibrated electron energy E_e and the double angle electron energy E_{DA} as a function of electron z-impact position z_e for data (black points) and Monte Carlo (open points) testing the absolute electromagnetic energy scale. b) The ratio $E_{\mathrm{bal}}(\mathrm{Data})$ / $E_{\mathrm{bal}}(\mathrm{Monte}$ Carlo) testing the relative electromagnetic energy scale.

3.4.2. Calibration

The energy of the electromagnetic particle E_e is calibrated to correct the relative energy scale between data and simulation, and to bring it to the absolute energy scale [42, 43]. In NC events, the double angle electron energy

$$E_{\mathrm{DA}} = \frac{2E_e^0 \sin\gamma_h}{\sin\gamma_h + \sin\theta_e - \sin(\theta_e + \gamma_h)}$$

can be determined from the polar angle of the electron θ_e and the inclusive polar angle of the hadronic final state γ_h only. Calibration constants are determined in a tight NC sample with a well-measured electron, hadronic final state and suppressed initial state radiation by constraining the ratio $E_{\mathrm{bal}} = E_e/E_{DA}$ to one. The constants depend on the impact z-position z_e of the electron on the LAr calorimeter face and the calorimeter octant and are determined for all time periods where the conditions are potentially different. Figure 3.1 shows tests of the electron calibration for 2005 e^-p data. From Fig. 3.1a can be read that after calibration the absolute energy scale of the electron is known to better than 1% in the LAr calorimeter barrel region. Figure 3.1b demonstrates that the relative electromagnetic energy scale of data and Monte Carlo simulation agrees to better than 1% in the barrel region and to better than 2% in the forward region where the statistical error is larger.

3.4.3. Misidentified Electrons

Hadrons misidentified as electrons are a main source of background in the electron channel. The description of such electrons is controlled using the inclusive NC sample described in section A.1 and requiring a second electron. This electron is almost always a misidentified
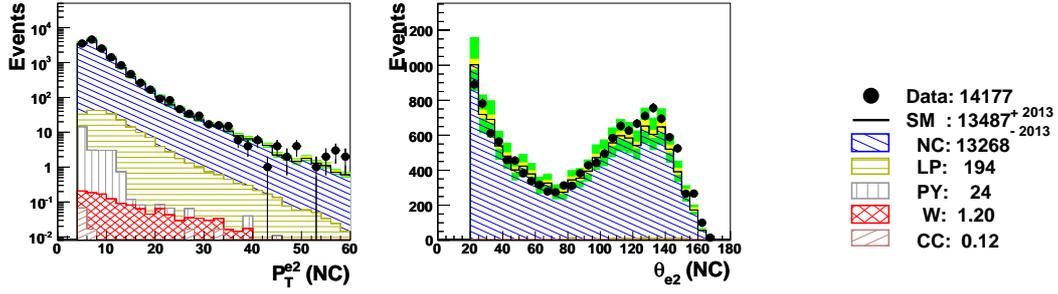
Figure 3.2.: Description of secondary identified electrons in the 2004-06 e^-p inclusive NC sample. These electrons are mainly misidentified hadrons.

hadron. About 3% of all NC events contain such fake electrons. Figure 3.2 shows the distributions for transverse momentum P_T^{e2} and polar angle θ_{e2} of these second electrons for 2004-06 e^-p data. They are well described within the uncertainties of the simulation up to high P_T^{e2}, giving confidence that this background source is correctly described.

3.5. Muons

3.5.1. Identification

Muons are identified based on their typical signature in a combination of subdetectors [37, 44]. While traversing the LAr calorimeter they behave like minimally ionising particles with $dE/dx \simeq 10$ MeV/cm for muons of energy above 200 MeV, leaving a narrow trace of energy depositions. Outside the hadronic part of the LAr calorimeter only muon signals are measured. They leave traces in the CMD and FMD, referred to as outer tracks in the following. Additional tracks in the CJC, referred to as inner tracks, can be linked to the outer tracks during reconstruction. Depending on how well these signatures are observed, there are five quality grades of muons defined by the muon identification algorithm. In descending order of quality the definitions of the grades are:

Grade 1 muons are of highest quality requiring an inner and outer track linked by the reconstruction.

Grade 2 muons also have an inner and outer track, but the tracks are only required to match at the analysis level. To match, the extrapolated inner track has to be closer than 0.5 to the outer track in the $\eta\varphi$-plane.

Grade 3 muons have no outer track, but only signals in the tail catcher matching the extrapolated inner track within 0.5 in the $\eta\varphi$-plane.

Grade 4 muons are based on estimators calculated from energy deposits in the LAr calorimeter. The estimators try to characterise patterns typical for MIPs.

Grade 5 Muons are based on outer tracks in the FMD without associated inner track.
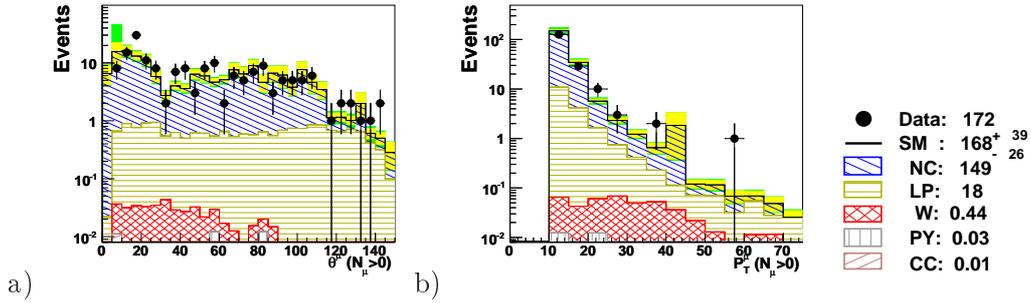
Figure 3.3.: Description of identified muons with $P_T^\mu > 10$ GeV in the 2004-05 e^-p inclusive NC sample. Most of these muons are falsely identified.

This analysis uses muons of grades 1, 2, 3 and 5 in the range $P_T^\mu > 2$ GeV and $5° < \theta^\mu < 175°$ only. Because hadrons are easily identified as grade 4 muons they are not used in the present analysis.

A muon is defined to be isolated against hadrons, if the calorimetric energy in a cylinder of radius 35 cm (75 cm) in the electromagnetic (hadronic) LAr calorimeter part around the extrapolated muon track is below 8 GeV, and if there is no other track within a distance of 0.5 in the $\eta\varphi$-plane. Isolated muons are excluded from the hadronic final state.

The efficiency to detect muons is checked with elastic muon pair production events and found to be well above 90% in the angular region $\theta_\mu > 20°$.

3.5.2. Misidentified Muons

Muons in inclusive NC, CC and photoproduction samples arise mostly from misidentified hadrons of the final state, together with signals in the muon detectors due to either electronic noise or cosmic radiation. The description of such misidentified muons was checked by requiring a muon with a transverse momentum $P_T^\mu > 10$ GeV in the inclusive NC sample described in section A.1. Figure 3.3 shows the description of identified muon candidates in the 2004-05 e^-p data. Roughly 0.2% of NC events contain muon candidates. This is about half of the fraction seen in a similar check in HERA-1 [4]. The difference is due to advances in the muon identification algorithm, specifically the stricter requirements for outer tracks. Real muon pair production contributes about 8% to the total SM prediction. The θ_μ distribution is well described in the region $\theta_\mu > 20°$, and described within the errors in the forward region (a). The transverse momentum distribution P_T^μ is described up to high values (b). In summary, misidentified muons are well estimated.

3.6. Hadronic Final State

3.6.1. Identification

The algorithm to identify the hadronic final state in H1 is based on identifying combinations of tracks and clusters as particles, taking the most precise information from either to get the best

resolution possible while avoiding double-counting of energy. The algorithm, called HADROO-2, is based on the best experience with several competing hadronic final state algorithms used during HERA-1 and constitutes now the unified H1 hadronic final state algorithm. While it is comparable to previous algorithms in the low momentum region, the identification was improved in the high momentum region [39].

Hadronic final state identification starts with selected tracks and calorimeter clusters not yet identified as components of isolated electrons or muons. The definition of hadronic final state particle candidates starts by assuming every track originates from a pion (the invariant mass of the particle candidate four-vector is set to m_π). The track measurement is compared to that of calorimetric energy in the LAr calorimeter behind the track and the more precise information is used to define the hadronic final state particle four-vector. The track measurement quality is quantified by the relative error on the track energy E_{track} and is compared to the expected relative LAr resolution. If the condition

$$\frac{\sigma_{Etrack}}{E_{track}} < \frac{0.5}{\sqrt{E_{track}}}$$

is satisfied, the calorimetric energy in a cone behind the track impact position is subtracted from the clusters and the track information used as particle four-vector. The cone is defined such that a hadronic shower can be fully contained in it. In case the condition is not met, the calorimetric energy measurement is preferred. In this case the compatibility of track and cluster energy taking into account fluctuations of the energy measurement is used to identify any neutral components in the cluster. If the track information can still be used, the cluster energy is taken as the hadronic final state particle four-vector, but only the track energy is subtracted from the hadronic shower cone. Residual neutral clusters are left untouched. In case the track information is completely unreliable, only the calorimeter cluster information is used to define the hadronic final state particle four-vector and the track is removed. In the central region, the track energy can be more precise than the calorimeter energy up to 25 GeV. In this region typically 60% of the total hadronic transverse momentum is measured from track information.

After all tracks have been associated to clusters defining all charged hadronic final state particles, the residual clusters are considered to be neutral hadronic final state particles. The four-vectors of these particles are rescaled to be massless.

3.6.2. Jet Reconstruction

Jets are reconstructed from hadronic final state particles using an inclusive-k_T jet finder algorithm [45]. The jet finder identifies jets with a minimum transverse momentum of 2 GeV. Only jets in the polar angular range $5^0 < \theta_{jet} < 170^0$ are used. In the electron and muon channel the misidentification of electromagnetic particles as jets is suppressed by requiring the jet radius to be $R_{jet} > 0.1$ in the $\eta\varphi$-plane and the electromagnetic fraction to be below 90%. All jets not satisfying these requirements are added to the four-vector of energy not contained in jets.

3.6.3. Jet Calibration

The energy scale of hadronic final state particles needs to be calibrated in two ways. Relative agreement between data and simulation is necessary to correctly compare observations to predictions. This relative agreement is achieved by calibrating data and Monte Carlo to the absolute scale independently. Absolute calibration of the energy scale is necessary to correctly determine the invariant mass of reconstructed particles. The available calibration procedure was developed for jets with transverse momenta above 10 GeV [39, 46]. The calibration is considered to be absolute if the transverse momentum balance

$$P_T^{bal} = \frac{P_T^h}{P_T^{\mathrm{DA}}}$$

is one, where

$$P_T^h = \sqrt{(\sum_h P_z^h)^2 + (\sum_h P_y^h)^2}$$

is the total hadronic transverse momentum calculated from all hadronic final state particles h and

$$P_T^{\mathrm{DA}} = \frac{2E_e^0}{\tan \frac{\theta_e}{2} + \tan \frac{\gamma_h}{2}}.$$

is the total transverse momentum measured by the double angle method. To a good approximation P_T^{DA} is independent of the energy scale and the relative data and Monte Carlo calibration. A high-Q^2 NC sample with suppressed initial state radiation is used to determine P_T^{DA}. An iterative procedure is applied to determine calibration constants $C(\theta, P_T^{\mathrm{DA}})$ separately for every data period and in every polar angle region shown in Fig. 3.4a. The calibration is applied to the energy fraction of the uncalibrated jet four-vector measured with clusters. The fraction measured with tracks is already calibrated and left untouched. Figure 3.4b shows the overall P_T^{bal} for the 2004-06 e^-p inclusive NC sample. The distribution peaks at one, verifying that the calibration procedure works overall. Figure 3.4c shows P_T^{bal} as a function of the inclusive hadronic polar angle θ_h^e calculated from the electron variables via

$$\tan(\theta_h^e/2) = \frac{2E_e^0 - (E_e - P_z^e)}{P_T^e}.$$

The plot demonstrates that the absolute energy scale of jets is known to better than 2% over the covered polar angle region of the calorimeter. Figure 3.4d shows that the relative energy scale of data and Monte Carlo agree to better than 2% over the covered region.

Calibration of the most forward jets below $\theta_{jet} < 7°$ was not available per default in the HERA-2 software and only added in this analysis. Jets in the very forward region of the LAr calorimeter suffer from losses in the non-instrumented part of the detector close to the beam pipe and a lot of dead material in front of the LAr calorimeter (contained in the CJC endcap and forward tracker). In HERA-1, jets were calibrated also in this region using the standard procedure and additional factors were applied to account for the energy losses. The barycentre of the jet

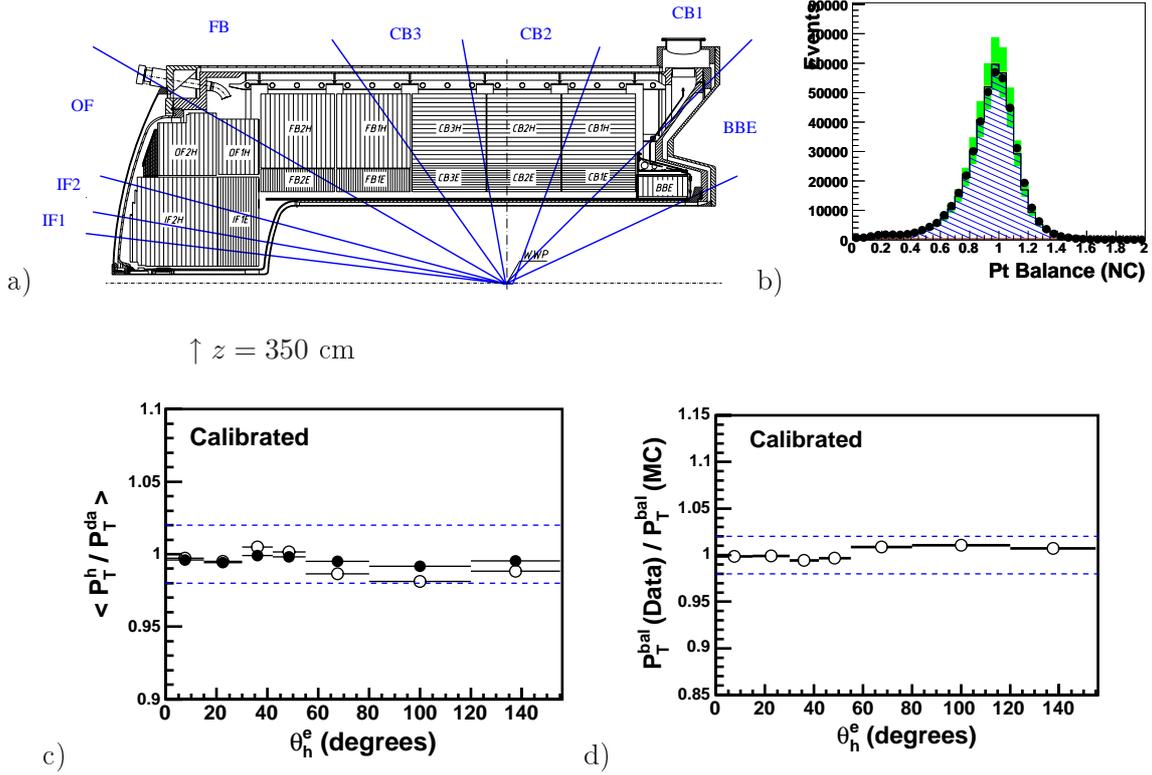$$\vec{cog}_{jet} = \sum_i \frac{\vec{x_i} E_i}{\sum_j E_j},$$

Figure 3.4.: Test of the absolute hadronic jet calibration. a) Calibration regions from $\theta = 7°$ to $155°$ and forward calibration regions at $z < (>)350$ cm in the LAr calorimeter. b) Distribution of the transverse momentum balance $P_T^{\mathrm{bal}} = P_T^h / P_T^{\mathrm{DA}}$ of data selected in the 2004-06 $e^- p$ period in the inclusive NC sample. c) Test of the absolute jet calibration for data (black circles) and Monte Carlo simulation (open circles) showing the mean of P_T^{bal} as a function of θ_h^e. d) Test of the relative calibration of data and Monte Carlo simulation showing the ratio P_T^{bal} (Data)$/P_T^{\mathrm{bal}}$ (MC) as a function of θ_h^e.

Uncalibrated   Calibrated   Loss Corrected

a)   b)   c)
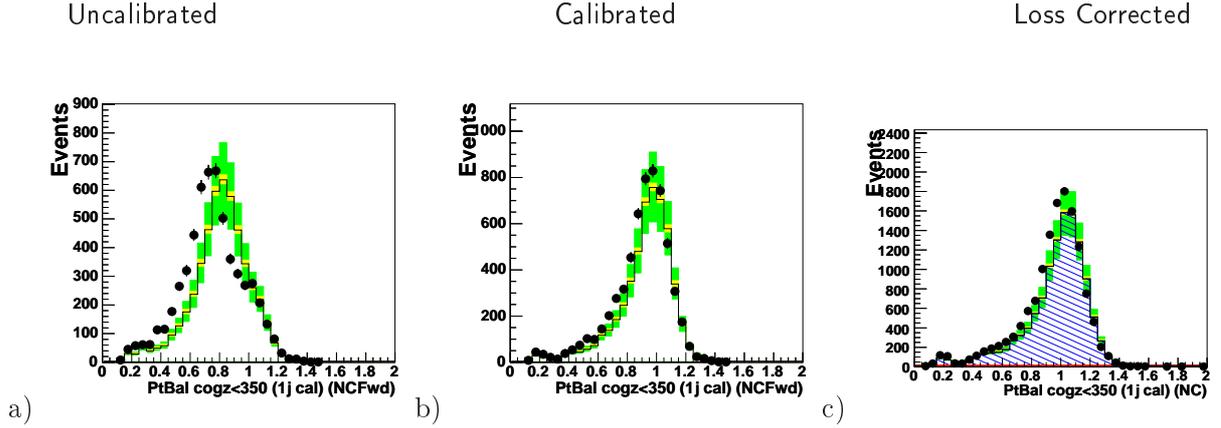
Jet barycentre cog_{jet} at $z < 350$ cm (IF region).

d)   e)   f)
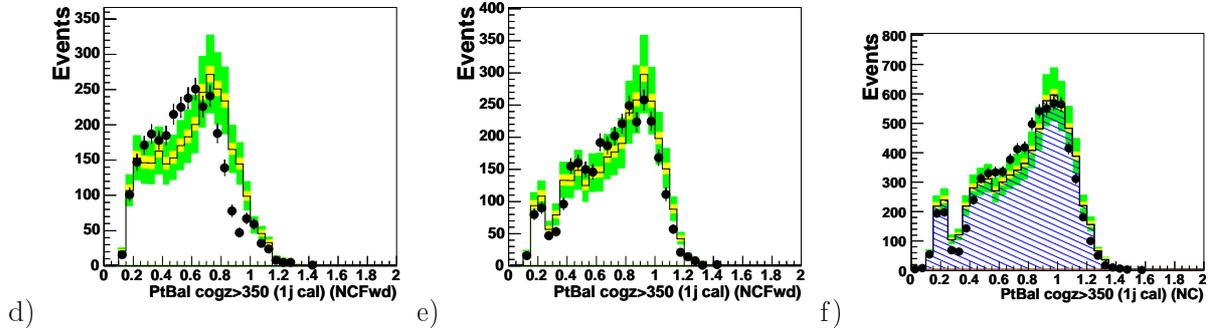
Jet barycentre at cog_{jet} $z > 350$ cm (OF region).

Figure 3.5.: Forward jet calibration at $\theta_{jet} < 7°$. Shown are the $P_T^{\textbf{bal}}$ distributions of uncalibrated jets (a,d); Jets calibrated like jets $7° < \theta_{jet} < 10°$ (b,e); Calibrated and loss corrected jets (c,f) in the 2003-06 e^+p data.

where i runs over all clusters in the jet and $\vec{x}_i$ is the barycentre of cluster i, was used to estimate the amount of energy lost from the jet. For cog_{jet} $z < 350$ cm and $z > 350$ cm a loss correction factor of 1.1 and 1.2, respectively, was applied. The position $z = 350$ cm corresponds roughly to the division between the IF and OF LAr calorimeter barrels, as indicated in Fig. 3.4a.

To test calibration of the forward region for HERA-2, NC events with exactly one forward jet $\theta_{jet} < 7°$ were selected in 2005 e^-p data. Figures 3.5a and 3.5d show the P_T^{bal} distributions of uncalibrated forward jets for cog_{jet} $z < 350$ cm and $z > 350$ cm, respectively. The distributions peak below one, hinting at a too low hadronic energy scale for the jets. The broad tail to very low P_T^{bal} hints at lost energy. The relative calibration of data and Monte Carlo simulation is also off. First a calibration of this region was tested, using the hypothesis that the calibration factors used for $7° < \theta_{jet} < 10°$ might be similar to those needed at $\theta_{jet} < 7°$. The true calibration constants in the very forward region cannot be determined, precisely because the energy of forward jets is not fully contained in the detector. Figures 3.5b and 3.5e show the calibrated P_T^{bal} distributions. The P_T^{bal} peak is closer to one and the relative data and Monte Carlo simulation accordance is improved. An additional factor to account for the energy losses is then additionally applied. This factor is estimated conservatively by not over-calibrating well-contained jets. This means the peak of the P_T^{bal} distribution is shifted to one, but not the mean of the distribution. An additional loss correction factor 1.1 is applied for both regions. The final P_T^{bal} distributions of forward jets are shown in Figs. 3.5c and 3.5f for the inclusive NC sample selected in 2003-06 e^-p data.

3.7. Observables for Event Selection

Several common observables are used throughout this thesis to select events with isolated leptons and missing transverse momentum. In the transverse plane, the following balances are used to measure missing transverse momentum:

- P_T^{calo} is the net transverse momentum of all calorimeter clusters. This quantity is uncalibrated and corresponds to the quantity used in the trigger to decide if missing transverse momentum is present in the event.

- P_T^X is the transverse momentum of the inclusive hadronic final state, calculated from all hadronic final state particles. Leptons are not included. In particular, in the tau channel the tau jet is subtracted from the hadronic final state.

- P_T^{miss} is the net transverse momentum of all reconstructed particles. It uses the calibrated electron, muon and calibrated hadronic final state four-vectors.

The difference between P_T^{miss} and P_T^{calo} is mostly due to muons which can have high momentum but deposit little energy in the calorimeter. In case there are no muons in the event, P_T^{miss} is very similar to P_T^{calo}. In case there is a muon with high transverse momentum in the event, P_T^{calo} is very similar to P_T^X. The requirement $P_T^{\text{calo}} > 12$ GeV is used throughout this thesis to select data samples with uniform trigger conditions in the phase space of the final selections.

The following observables related to missing transverse momentum are also used:

- $(E - P_z) = \sum_i (1 - \cos\theta_i)$ is the longitudinal energy balance summed over all particles i. $(E - P_z)$ is often rewritten as

$$\delta^{\text{miss}} = 2 \cdot E_e^0 - (E - P_z)$$

  to denote the missing difference from the double incident electron energy $2 \cdot E_e^0 = 55$ GeV. For events where only momentum in the proton direction goes undetected, δ^{miss} is zero. This variable is mainly used to select NC events by requiring $\delta^{\text{miss}} < 8$ GeV as illustrated in Fig. 3.6a (The full NC selection is described in section A.1).

- V_{ap}/V_p is used as a measure for the balance of the event in the direction of the total missing energy four-vector. It is the ratio of energy components (anti-)parallel to the total calorimetric four-vector calculated as

$$V_{ap} = -\sum_i \frac{\vec{P_T^X} \cdot \vec{P_{T,i}^X}}{P_T^X} \qquad \text{for} \qquad \vec{P_T^X} \cdot \vec{P_{T,i}^X} < 0$$

  and

$$V_p = \sum_i \frac{\vec{P_T^X} \cdot \vec{P_{T,i}^X}}{P_T^X} \qquad \text{for} \qquad P_T^X \cdot \vec{P_{T,i}^X} > 0,$$
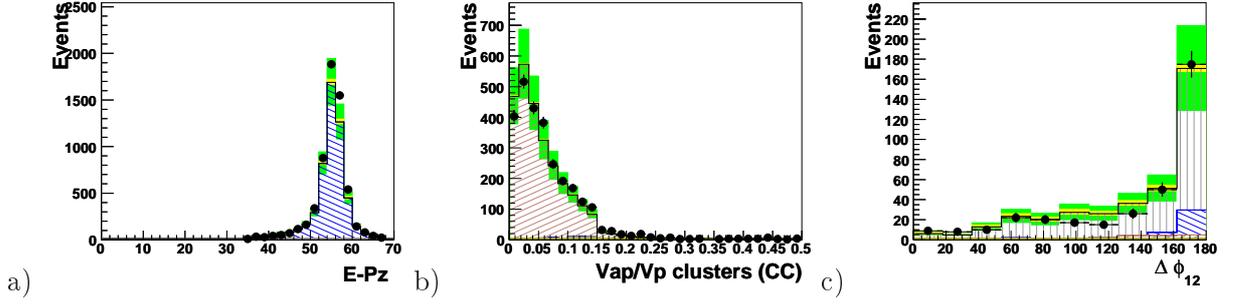
Figure 3.6.: Typical observables used to select different SM processes. Shown are distributions from the inclusive selections described in appendix A in the phase space $P_T^{\text{calo}} > 12$ GeV. a) NC peaks at $\delta^{\text{miss}} = 2 \cdot E_e^0 - (E - P_z) < 8$ GeV. b) CC peaks at low V_{ap}/V_p. c) Photoproduction dijets peak at $\Delta\phi(jet1, jet2) = 180°$.

where i runs over all particles in the event. The default is to calculate V_{ap}/V_p from all reconstructed particles, but in the tau channel some pathological events have been observed where the hadronic final state is badly reconstructed and the resulting V_{ap}/V_p is too high. It was apparent that these events are in fact photoproduction events. To suppress these topologies, the V_{ap}/V_p calculated from clusters directly is used as a safeguard. All cuts on V_{ap}/V_p have to pass both versions of V_{ap}/V_p. In NC and photoproduction events V_{ap}/V_p is typically around 0.5 within the resolution because of the balanced back-to-back topology. When requiring missing energy, V_{ap}/V_p will be lower, but can still be used to discriminate NC and photoproduction events from those with a real momentum imbalance. Events with high energetic particles that do not deposit much energy in the calorimeter, like muons and neutrinos, have typically a low V_{ap}/V_p. CC events can be selected by requiring $V_{ap}/V_p < 0.15$ as illustrated in Fig. 3.6b (The full CC selection is described in section A.2).

- $\Delta\phi(l, X)$, the azimuthal angle difference between the lepton l and the hadronic system X, is a measure for acoplanarity. $\Delta\phi(l, X)$ can be used to measure if any neutrinos were produced along with the lepton. In NC and photoproduction events the lepton and the hadronic system are expected to be back-to-back, or $\Delta\phi(l, X) \approx 180°$ within the resolution, as illustrated for photoproduction in Fig. 3.6c (The full photoproduction selection is described in section A.3). In the case of photoproduction the lepton is generally a misidentified hadron. If there are neutrinos produced along with the lepton, like in decays of W bosons and tau leptons a value of $\Delta\phi(l, X)$ significantly below 180° is expected.

- ζ_e^2 is calculated as

$$\zeta_e^2 = 4 \cdot E_e^0 E_e \cos^2 \theta_e/2.$$

For real NC events ζ_e^2 is equivalent to Q_e^2. In this case, ζ_e^2 is expected to fall steeply with the NC cross section like Q^2. In case the isolated electron candidate is not the scattered electron, but coming from a W decay, high values of ζ_e^2 are expected since the W decay electron tends to go more forward.

4. Preselection

4.1. Data Samples

Figure 4.1a shows the integrated luminosity collected by H1 during HERA running. Running periods with different HERA machine parameters used in this thesis are listed in Tab. 4.1. In this thesis data from HERA-1 are reanalysed and extended by HERA-2 data up to November 11th 2006[1]. Data taken before 1994 are neglected. The combined e^-p data from the 1998-99 and 2004-06 periods contains the complete HERA e^-p data and corresponds to a integrated luminosity of 186.4 pb^{-1}. This is comparable with the total e^+p data sample from the 1994-97, 1999-2000, 2003-04 and 2006 periods of 220.2 pb^{-1}. The given values are valid for the electron and muon channels. The luminosity in the tau channel is slightly lower because of a stricter vertex requirement and additionally listed in table 4.1. In total, the present analysis uses a data sample larger by a factor of four compared to the previous published results. In particular, the e^-p data sample has increased by a factor of 13. Figure 4.1b shows that additional ~ 100 pb^{-1} of e^+p data are expected until the end of data taking in July 2007, about half of which is expected to be recorded in the high energy run lasting until March 2006.

The preselection requirements for a clean data sample consisting mostly of ep collision events are very similar for all channels. They are described in the following, and the high data quality of the HERA-2 data samples is demonstrated afterwards.

4.2. Technical Requirements

The integrated luminosity of a data sample depends on the availability of necessary detector components, general quality of the runs and the operation of required triggers during data taking. Only runs meeting the same requirements as used for calculating the luminosity are accepted in the analysis. The run quality is an attribute assigned to runs by hand after the general run conditions during data taking have been evaluated. Only runs determined to be of *good* and *medium* quality are considered, while *poor* runs are rejected. The LAr calorimeter, SpaCal, ToF and luminosity system are required to be operational. The high voltage settings for the tracking chambers CJC1, CJC2 and CIP2000 were required to be at full voltage ("100%") to ensure optimal efficiency.

4.3. Trigger Requirements

All channels are triggered by electron, missing energy or muon triggers. Electrons and missing energy are triggered by subtriggers 66, 67 and 77 [47]. Subtriggers 66 and 77 require missing

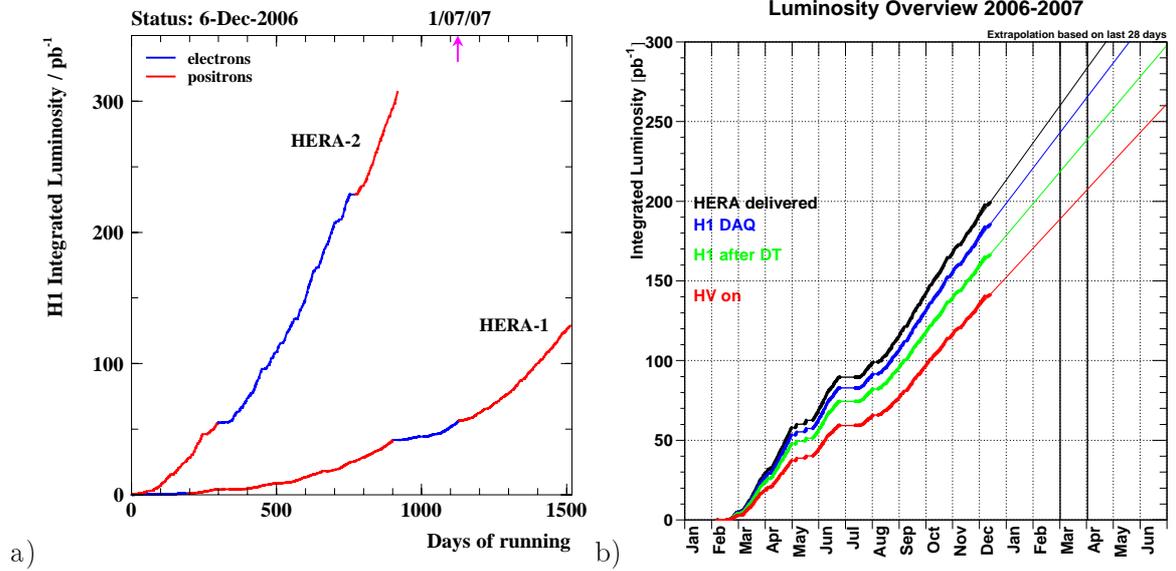---

[1]Up to file DST #5961.

Figure 4.1.: The integrated luminosity collected by H1. a) Total integrated luminosity collected by H1 in HERA-1 and HERA-2. b) Luminosity collected in 2006-2007. This thesis includes all data taken up to November 11th 2006. Data taking will continue until July 2007 providing another projected ~ 100 pb^{-1} of e^+p data, about half of which will be taken during the high energy run until March 2006.

Period	Years	Collisions	E_p	$\int \mathcal{L}$ e, μ channel	$\int \mathcal{L}$ τ channel
HERA-1	1994-97	e^+p	820 GeV	37.7 pb^{-1}	36.4 pb^{-1}
	1998-99	e^-p	920 GeV	13.9 pb^{-1}	13.7 pb^{-1}
	1999-2000	e^+p	920 GeV	68.8 pb^{-1}	65.8 pb^{-1}
HERA-2	2003-04	e^+p	920 GeV	54.4 pb^{-1}	53.7 pb^{-1}
	2004-06	e^-p	920 GeV	172.5 pb^{-1}	169.9 pb^{-1}
	2006	e^+p	920 GeV	59.3 pb^{-1}	58.7 pb^{-1}
Total				**406.6 pb^{-1}**	398.2 pb^{-1}

Table 4.1.: Integrated luminosity for the HERA running periods analysed in this thesis. E_p denotes the energy of the incident proton. The electron energy is always $E_e = 27.6$ GeV. The integrated luminosity in the tau channel is slightly lower than for the electron and muon channels due to a stricter vertex requirement.

transverse energy $E_T > 2$ GeV together with tracks for correct timing. Subtrigger 67 triggers on energetic trigger cells with a lower threshold of 6 GeV in the LAr calorimeter. None of these subtriggers are prescaled. Subtrigger 18 is used as muon trigger. Its efficiency was shown to be about 80% in the central region. This trigger is expected to slightly increase the detection efficiency of the muon signal by about 5%. To ensure uniform trigger conditions for all channels, all selections are made in the phase space $P_T^{calo} > 12$ GeV. The missing energy trigger efficiency is determined as a function of (P_T^{miss}, γ_h) from pseudo-CC events for every data period and applied as a weight to simulated events. At $P_T^{miss} \approx 12$ GeV the CC trigger efficiency is about 50%, rising to 100% for $P_T^{miss} > 25$ GeV.

4.4. Timing

The time of the ep interaction is required to be in a certain time window around the nominal bunch crossing time T_0^{nom}, provided by the HERA clock. Interaction time measurements based on tracks in the CJC and energy depositions in the LAr calorimeter are available. The T_0^{CJC} is measured using the time of hits on the wires in the CJC. At least one selected track in the event is required for the T_o^{CJC} to be reliable. Else, no T_o^{CJC} requirement is applied. The accepted timing window depends on the data period and is $\pm$ 30 ticks wide in HERA-2, where 500 ticks ($\equiv$ 96 ns) correspond to 1 bunch crossing. The peak of the T_0^{CJC} is centred on 458 ticks (in HERA-2) after T_0^{nom} due to a delay from the charge drift time on the wires. In a brief period of the early 2003-04 data sample (up to run 368000) the window had to be widened to $\pm$55 ticks around 430 ticks due to a second peak arising from technical problems in the readout electronics. Apart from this feature the time dependence of T_0^{CJC} has been checked to be negligible in HERA-2. Events in the T_0^{CJC} window one or two bunch crossings earlier/later than the nominal bunch crossing are also accepted.

The T_0^{LAr} is determined using the time of energy deposits in the LAr calorimeter. This time is estimated from LAr calorimeter trigger information. In HERA-1, T_0^{LAr} is determined based on the energy-weighted mean time of depositions [48]. A new method based on finding a peak in the same information was developed for the HERA-2 period in the framework of this thesis [49]. For all periods, the requirement to keep an event is $T_0^{LAr} < 0.7$ bunch crossings.

4.5. Vertex

All analyses in this thesis require a vertex reconstructed using tracks measured in the CJC only. This requirement implies that there is at least one central vertex-fitted track in an event. For the tau channel the z-position vtx_z of the vertex is required to be within 35 cm of the nominal interaction point. This corresponds to a width of about 3σ of the vtx_z distribution. For the electron and muon channels, this requirement is relaxed to the range $-40 < vtx_z < 100$ cm in order to keep events where a nuclear interaction takes place in the detector material and the reconstructed vertex is misplaced from the real vertex. For such events, electrons or muons can still be reliably reconstructed. These different vertex ranges explain the higher integrated luminosity for the electron and muon channels with respect to the tau channel listed in table 4.1.
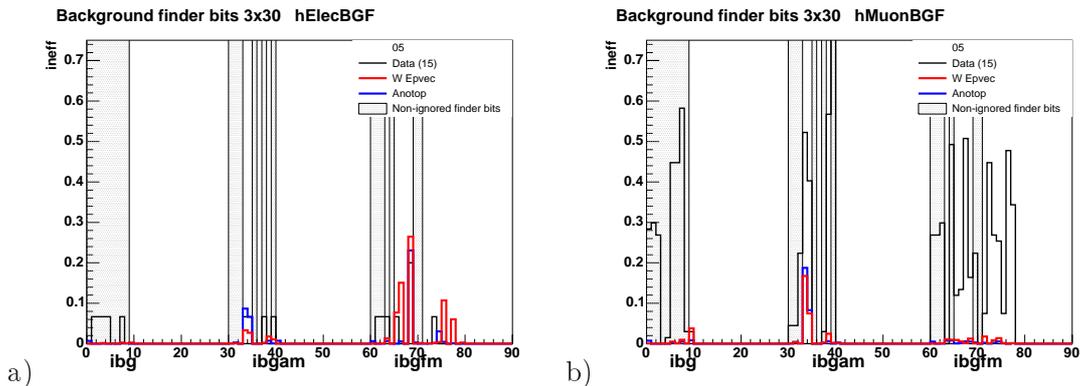
a)   b)

Figure 4.2.: Fraction of background finder bits firing for 2005 e^-p data (black), EPVEC (red) and ANOTOP (blue) when run through the complete electron (a) and muon (b) channel analysis. The background finders are arranged in three sets of bit-coded flags starting at bin 0, 30 and 60. The finder bits, which were later masked out for the full analysis because they are too inefficient on the signal are shown as hatched columns.

4.6. Non-*ep* Background Suppression

A set of topological background finders has been developed in H1 to detect signatures in the detector that do not come from ep collisions [50]. They are based on the detection of topologies typical for muons from the interactions of protons in the beam halo with material in front of the detector, and for muons from cosmic background radiation. The rates observed for individual background finders in the data and the EPVEC and ANOTOP signal Monte Carlo generators were checked for each channel by running the complete analysis with transparent background finders. Figure 4.2 illustrates this method for the electron and muon channels. A set of background finders that represents a good compromise between suppression of background and high acceptance of signal topologies is defined for each channel. Only background finders are used that do no yet reject more than 1% of either signal MC generator, unless the background observed in the data is overwhelming and must be suppressed.

The background conditions at HERA-2 have proven to be more difficult than at HERA-1. One of the main reasons is increased synchrotron radiation in the backward region of the detector because of the more cramped geometry after installation of the new focusing magnets. The measures described so far where not sufficient to suppress non-*ep*-background, mainly from beam-gas interactions. Additional cuts to suppress this background have been developed for the inclusive measurement of the CC cross section at HERA-2 [51]. Because the analyses described here are based on a similar phase space, these conditions can be largely adopted:

- If there is hadronic activity in the central region of the calorimeter, at least one good quality track is required in the event to ensure that the energy deposit comes from charged particles originating in the event vertex. Events are rejected if there are no good quality tracks in the event, but $\gamma_h > 40°$ or $\theta_{LAr} > 20°$, where θ_{LAr} is the inclusive polar angle of activity in the LAr calorimeter calculated from clusters. This cut removes mostly events with cosmic muons.

41

- The number of non-vertex-fitted tracks N_{DTNV} should not exceed the number of vertex-fitted tracks N_{DTRA} in the event by more than a factor of 20 to ensure that most tracks actually come from the vertex. This cut removes mostly events with beam-gas interactions.

- To reject events with badly measured muons, P_T^{miss} and P_T^{calo} are required to be reasonably comparable. Events are rejected, if $P_T^{\text{miss}}/P_T^{\text{calo}} > 5$.

- At least one charged particle is required in all events. For this, at least one vertex-fitted track in the event is required to be linked to a cluster. The minimal distance between any track and any cluster dct in the event is calculated. Events are rejected if $dct > 0.5$ in the $\eta\varphi$-plane. For polar angles $\theta < 20°$ the tracking efficiency is lower. If $\theta_{cluster} < 20°$ the required track-cluster match is only $dct < 1.0$ in the $\eta\varphi$-plane.

4.7. Quality of the HERA-2 Data Samples

Figures 4.3 and 4.4 show data quality control distributions for the 2003-06 e^+p and 2004-06 e^-p data, respectively, preselected in the $P_T^{\text{calo}} > 12$ GeV phase space passing the requirements described in this chapter. The z_{vertex} distributions (a) show no baseline offset in the tails, indicating the absence of large amounts of non-ep-background. The hadronic final state ϕ distribution (b) is flat within the errors. The eightfold pattern that is visible can be explained by non-instrumented cracks between the LAr calorimeter octants. Electronic noise in the LAr calorimeter readout would show up as a prominent peak in this distribution. The contribution of events from NC, CC and photoproduction processes in this sample is of the same order of magnitude. The typical efficiency of this preselection for EPVEC events is 70%, and for ANOTOP events 90%.
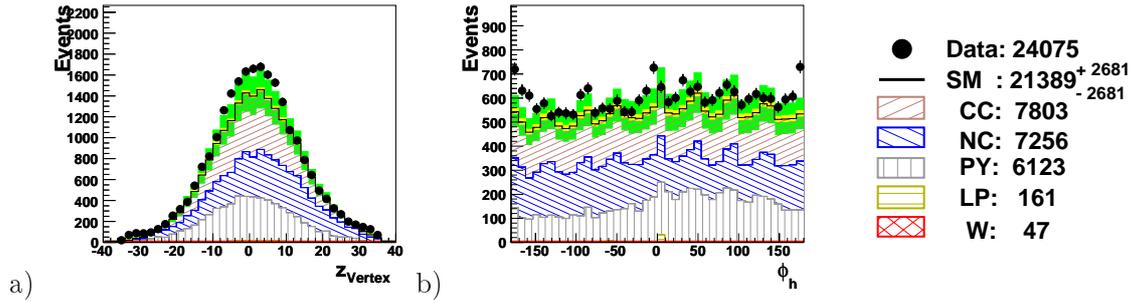
Preselected Data at $P_T^{\mathrm{calo}} > 12$ GeV (2003-06, e^+p)
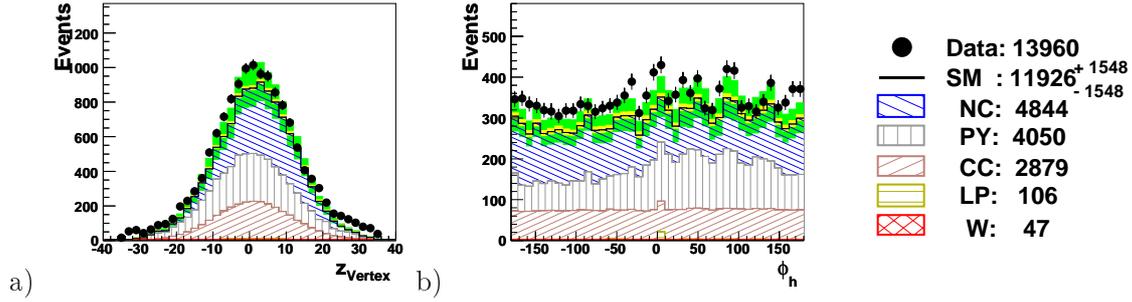
Figure 4.3.: Data quality control distributions in the preselected data at $P_T^{\mathrm{calo}} > 12$ GeV for the 2003-06 e^+p data. The data are shown as points. The SM total prediction (SM) contains contributions from neutral currents in DIS (NC), photoproduction (PY) and charged currents in DIS (CC) of the same order of magnitude. Lepton pair production (LP) and the signal W production (W) contribute little at this level. a) The z_{vertex} shows no excess in the tails. b) The hadronic final state ϕ distribution is flat within the errors where measured.

Preselected Data at $P_T^{\mathrm{calo}} > 12$ GeV (2004-06 e^-p)

Figure 4.4.: Data quality control distributions in the preselected data at $P_T^{\mathrm{calo}} > 12$ GeV for the 2004-06 e^-p data.

5. Analysis of Isolated Electrons and Muons

5.1. Selection

5.1.1. Common Phase Space

The selection in the electron and muon channel is based on the data samples preselected with the requirements of chapter 4. Electron and muon events are then selected in following phase space:

- $P_T^{\text{calo}} > 12$ GeV is required to ensure uniform missing transverse momentum trigger conditions.

- $P_T^{\text{miss}} > 12$ GeV ensures missing transverse momentum using the fully reconstructed and calibrated final state. In the muon channel additionally $P_T^{\text{X}} > 12$ GeV is required.

- $P_T^l > 10$ GeV. For leptons from a W decay a high transverse momentum is expected due to the high mass of the W boson. Generally, leptons with lower transverse momentum are unlikely to come directly from the hard process.

- $5° < \theta_l < 140°$ in order to ensure containment within the LAr calorimeter acceptance. Larger polar angles correspond to the kinematic region $Q^2 \lessapprox 100$ GeV where the NC cross section is large and the scattered electron is expected in that region. Muons in the backward direction are hard to detect because leakage of hadrons through the SpaCal into the instrumented iron is high, imitating a muon signature.

For the final data selection, good isolation and quality of the lepton candidates are required to optimise the signal selection and suppress background from SM processes as far as possible. All selection criteria are summarised in Tab. 5.1 and discussed in the following. The criteria are the same as for the HERA-1 analysis [4]. To verify that the SM backgrounds are well estimated, control samples are selected which enrich the largest background contributions in the individual channels. These background studies are described in section 5.3.

Observable	Electron Channel	Muon Channel
Phase Space		
θ_l	$5° < \theta_l < 140°$	
P_T^l	> 10 GeV	
P_T^{calo}	> 12 GeV	
P_T^{miss}	>12 GeV	
P_T^X	-	> 12 GeV
Isolation		
D_{jet}	> 1.0	
D_{track}	> 0.5	
Anti-NC		
ζ_l^2	> 5000 GeV^2 for $P_T^{calo} < 25$ GeV	-
V_{ap}/V_p	< 0.5	< 0.5
	(<0.15 for $P_T^e < 25$ GeV)	(<0.15 for $P_T^{calo} < 25$ GeV)
$\Delta\phi(l, X)$	$< 160°$	$< 170°$
δ_{miss}	> 5 GeV	-

Table 5.1.: Summary of selection requirements for the electron and muon channels. All details of the selection are described in the text.

5.1.2. Electron Channel

Events in the common phase space with one or two electron candidates are used in the electron channel. More than two are not allowed, in order to suppress multi-electron topologies. No muon candidates are allowed in the event to be exclusive against the muon channel. To suppress misidentification of neutral particles as electron, a reliable track has to be associated with the electron:

- $P_T^{\text{track}} > 1$ GeV. The transverse momentum of the best associated track has to be above 1 GeV. This is not required if the expected transverse length of the track through the CJC is $l^{\text{track}} < 10$ cm. In this case the track momentum may not be reliably measured.

- If the best associated track is a vertex-fitted track, the track-cluster distance of closest approach has to be $dca_{DTRA} < 12$ cm.

- If the best associated track is a non-vertex-fitted track, the track-cluster dca has to be $dca_{DTNV} < 12$ cm and there has to be a vertex-fitted track within $dca_{DTRA} < 90$ cm. This requirement increases acceptance of events where the vertex-fitted track hypothesis is pulled away from the original non-vertex-fitted track by a fit through a displaced vertex.

- If the associated track is a central or combined track, the track start radius must be $R_{start} < 30$ cm. For tracks starting later it is probable that they come from photoconversion.

- The electron cluster must be away from cracks in the calorimeter acceptance to make sure the shower is fully contained in the fiducial calorimeter volume and the energy measurement is not distorted by dead material. In the barrel region ($z < 292$ cm), the electron azimuthal angle φ_e has to be at least 2° from cracks between the calorimeter octants. The z-position of the cluster barycentre has to be at least 5 cm from the crack between CB2 and CB3 wheels at $z = 24$ cm that is impacted at steep angles.

To suppress CC events the following isolation requirements are applied to the electron candidate:

- In the region $\theta_e > 45°$ the number of good quality tracks matched to the electron must be exactly one. Tracks match if the track-cluster distance of closest approach is less than 12 cm. The distance to other vertex-fitted tracks must be at least $D_{DTRA} > 0.5$ in the $\eta\varphi$-plane. For electrons with a lower polar angle track isolation cannot be reliably determined and is not required.

- $D_{jet} > 1.0$. The distance of the electron to the nearest jet must be $D_{jet} > 1.0$ in the $\eta\varphi$-plane. D_{jet} is calculated as the minimal distance between the electron four-vector and the four-vector of any jet meeting the requirements defined in 3.6.2. If there are no selected jets in the event, D_{jet} is defined with respect to the total hadronic final state four-vector. If the total hadronic transverse momentum is below 1 GeV, the cut is not applied. This cut rejects electrons which are parts of jets or misidentified radiated photons and mainly reduces background from CC processes.

Electron Channel		H1 Data	SM Expectation	SM Signal	Other SM Processes
2003-06 e^+p	All P_T^X	11	11.60 ±1.47	7.91 ±1.20	3.68 ±0.27
113.7 pb^{-1}	$P_T^X > 25$ GeV	5	1.98 ±0.29	1.47 ±0.23	0.51 ±0.07
2004-06 e^-p	All P_T^X	11	18.09 ±2.29	12.00 ±1.82	6.09 ±0.47
172.5 pb^{-1}	$P_T^X > 25$ GeV	1	4.02 ±0.61	2.24 ±0.34	1.79 ±0.27

Table 5.2.: Observed and predicted number of events in the electron channel for the 2003-06 e^+p and 2004-06 e^-p data. The error contains systematic and statistical uncertainties added in quadrature.

The NC contribution is suppressed by the following cuts:

- $V_{ap}/V_p < 0.5$. If $P_T^e < 25$ GeV it is required that $V_{ap}/V_p < 0.15$. NC events are expected at higher V_{ap}/V_p because of their balanced topology.

- $\zeta_e^2 > 5000$ GeV^2 is required for events with $P_T^e < 25$ GeV where the NC contribution is largest.

- $\Delta\varphi(e, X) < 160°$ suppresses NC topologies where the electron and the jet are back-to-back.

- $\delta^{\mathrm{miss}} > 5$ GeV. For NC events, δ^{miss} is expected to be compatible with zero within the resolution. This condition is not required if there are two electrons in the event, or if the isolated electron has the opposite electron beam charge. For NC events, only the scattered electron is expected in the detector, and it has the same charge as the electron beam.

Figure 5.1 shows the distributions of the final selection in the electron channel for the HERA-2 data. Table 5.2 lists the observed and predicted numbers of events in the final selection. In the 2003-06 e^+p sample 11 events are selected with 11.6 ± 1.5 expected from the SM. At $P_T^X > 25$ GeV 5 events are observed for only 2 ± 0.3 predicted. Four of the events at high P_T^X are selected in the 2003-04 e^+p data. In the 2006 e^+p data one electron event at high P_T^X has been seen so far. In the 2004-06 e^-p sample 11 events are selected, with 18.1 ± 2.3 expected from the SM. At $P_T^X > 25$ GeV one event is observed while 4 ± 0.6 are predicted. In the e^-p data there is a deficit of events at high P_T^X in comparison to the e^+p data, especially the e^+p data before 2004. The kinematics of all events selected in the electron and muon channels are shown in Tab. 5.4. Event displays of two of the electron events selected in HERA-2 e^+p data are shown in Fig. 5.7.
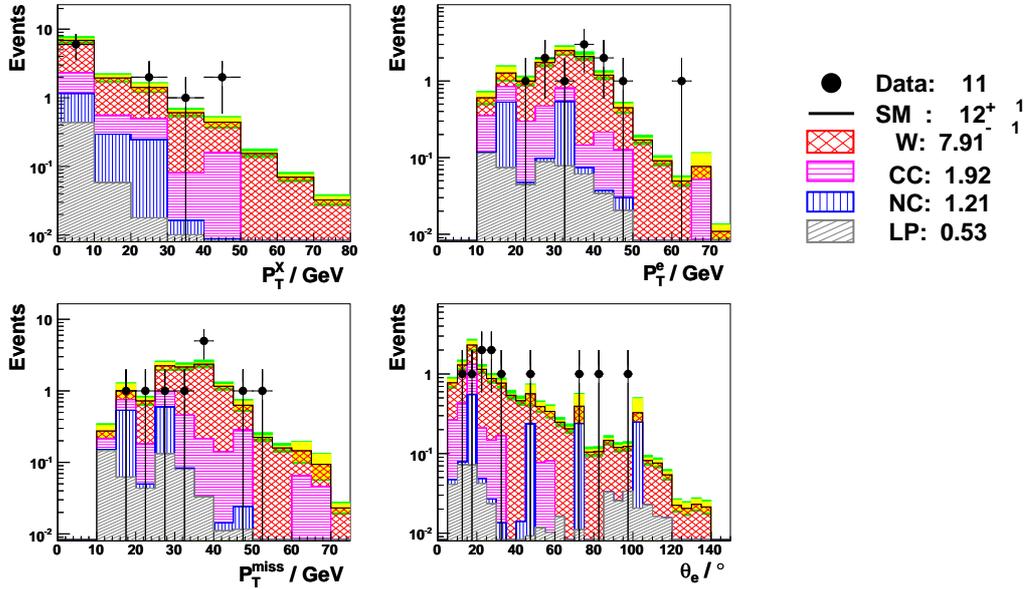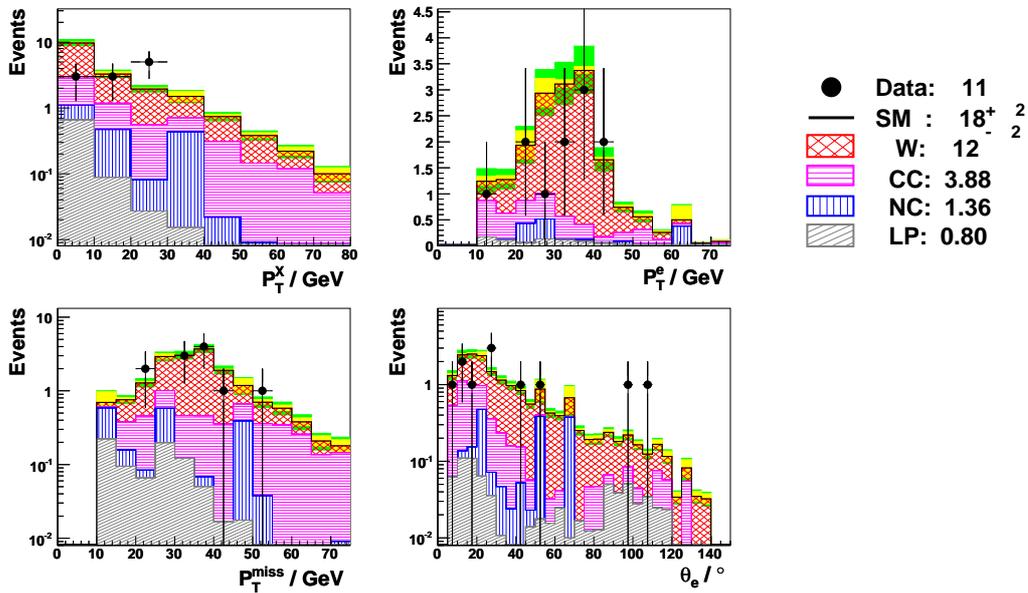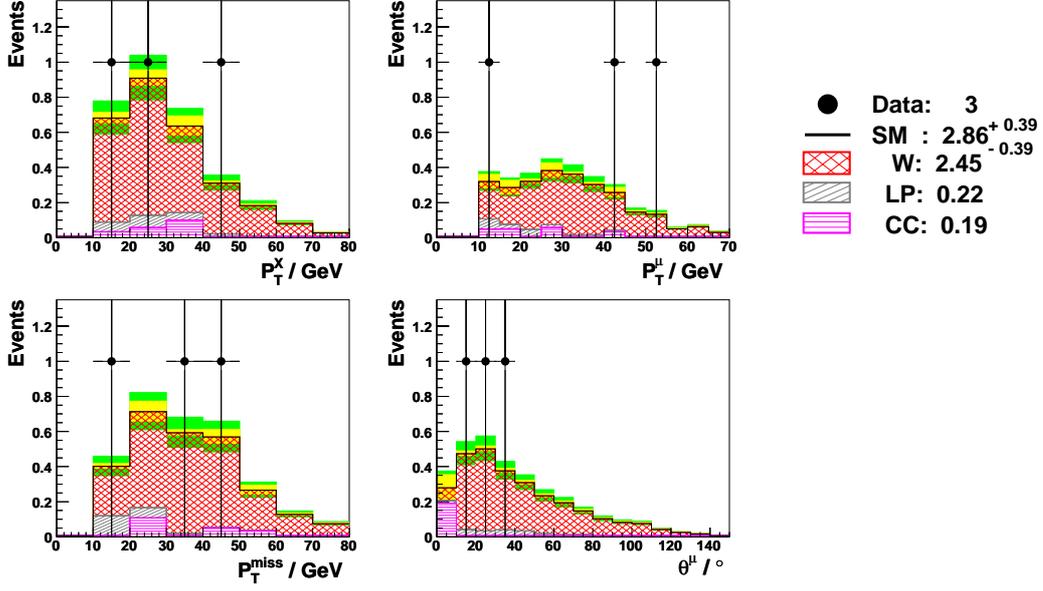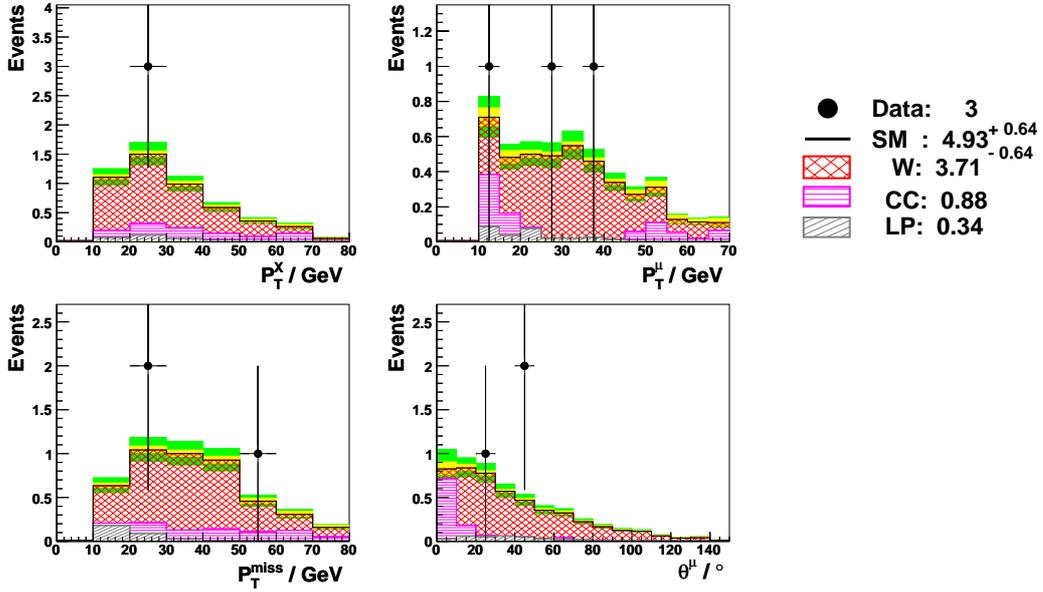
Figure 5.1.: The final data selection in the electron channel for the 2003-06 e^+p and 2004-06 e^-p samples compared to the SM expectation. The total error (systematic and statistical uncertainties combined in quadrature) on the SM expectation is given by the green shaded band. The statistical error is given by the yellow band. "Data" is the number of events observed in the data, "SM" the sum of the SM contributions listed below and displayed separately in each of the plots. The signal component (W) is given by the red hatched histogram.

Muon Channel		H1 Data	SM Expectation	SM Signal	Other SM Processes
2003-06 e^+p	All P_T^X	3	3.13 ±0.43	2.69 ±0.41	0.44 ±0.02
113.7 pb^{-1}	$P_T^X > 25$ GeV	1	1.76 ±0.24	1.51 ±0.23	0.25 ±0.01
2004-06 e^-p	All P_T^X	3	5.40 ±0.70	4.09 ±0.62	1.31 ±0.08
172.5 pb^{-1}	$P_T^X > 25$ GeV	1	3.16 ±0.42	2.29 ±0.35	0.86 ±0.07

Table 5.3.: Observed and predicted number of events in the muon channel for the 2003-06 e^+p and 2004-06 e^-p data. The error contains systematic and statistical uncertainties added in quadrature.

5.1.3. Muon Channel

Events in the common phase space with a muon candidate are used in the muon channel. Only one muon is allowed in the event to suppress muon pair production. SM background processes are suppressed by the following cuts:

- $D_{jet} > 1.0$ in the $\eta\varphi$-plane isolates the muon additionally from jets.

- $V_{ap}/V_p < 0.5$. If $P_T^{\text{calo}} < 25$ GeV it is required that $V_{ap}/V_p < 0.15$. This rejects remaining NC events.

- $\Delta\varphi(\mu, X) < 170°$ ensures acoplanarity, suppressing remaining lepton pair production and NC events.

Figure 5.2 shows the distributions of events selected in the muon channel. Table 5.3 lists the observed and predicted numbers of events in the final selection. In the 2003-06 e^+p sample 3 events are selected with 3 ± 0.4 expected from the SM. In the 2004-06 e^-p sample 3 events are selected, with 5 ± 0.7 predicted. In each of the samples one event with high $P_T^X > 25$ GeV is selected. Figure 5.5 shows that this rate of events at high P_T^X is low compared to the six events observed in the HERA-1 data. Figure 5.8 shows two of the muon events selected in HERA-2. The kinematics of all events selected in HERA-2 in the electron and muon channels are shown in Tab. 5.4.

Figure 5.2.: The final data selection in the muon channel for the 2003-06 e^+p and 2004-06 e^-p samples compared to the SM expectation. The total error (systematic and statistical uncertainties combined in quadrature) on the SM expectation is given by the green shaded band. The statistical error is given by the yellow band. "Data" is the number of events observed in the data, "SM" the sum of individual contributions listed below and displayed separately for each of the plots. The signal component (W) is given by the red hatched histogram.

Run	Event	Lepton	P_T^l / GeV	θ_l / $^\circ$	φ_l / $^\circ$	P_T^X / GeV	P_T^{miss} / GeV	γ_h / $^\circ$
03-04 e^+p								
364631	64013	e	$45.9^{+1.9}_{-1.9}$	$80.5^{+0.25}_{-0.25}$	$-41.2^{+0.30}_{-0.30}$	< 2	$45.9^{+1.9}_{-1.9}$	< 5
369241	**6588**	**e**	$\mathbf{27.0^{+1.0}_{-1.0}}$	$\mathbf{20.2^{+0.22}_{-0.22}}$	$\mathbf{124.5^{+0.46}_{-0.46}}$	$\mathbf{42.5^{+5.7}_{-5.7}}$	$\mathbf{55.4^{+5.0}_{-5.0}}$	$\mathbf{46.5^{+0.0}_{-0.0}}$
377311	80405	e	$41.6^{+1.5}_{-1.5}$	$29.3^{+0.22}_{-0.22}$	$-94.6^{+0.46}_{-0.46}$	< 2	$41.6^{+1.5}_{-1.5}$	< 5
378826	30420	e	$39.3^{+1.5}_{-1.5}$	$30.6^{+0.25}_{-0.25}$	$69.9^{+0.30}_{-0.30}$	$3.7^{+1.3}_{-1.3}$	$38.0^{+1.5}_{-1.5}$	< 5
385422	**76666**	**e**	$\mathbf{28.1^{+1.3}_{-1.3}}$	$\mathbf{96.4^{+0.25}_{-0.25}}$	$\mathbf{-59.6^{+0.30}_{-0.30}}$	$\mathbf{27.4^{+3.5}_{-3.5}}$	$\mathbf{40.7^{+2.7}_{-2.7}}$	$\mathbf{< 5}$
386075	93702	e	$39.2^{+1.7}_{-1.7}$	$72.6^{+0.25}_{-0.25}$	$113.6^{+0.30}_{-0.30}$	< 2	$36.9^{+1.7}_{-1.7}$	< 5
389826	**2783**	**e**	$\mathbf{61.2^{+2.2}_{-2.2}}$	$\mathbf{45.6^{+0.25}_{-0.25}}$	$\mathbf{41.6^{+0.30}_{-0.30}}$	$\mathbf{46.3^{+4.8}_{-4.8}}$	$\mathbf{28.7^{+2.0}_{-2.0}}$	$\mathbf{51.0^{+4.5}_{-4.5}}$
391884	**49715**	**e**	$\mathbf{35.4^{+1.3}_{-1.3}}$	$\mathbf{22.6^{+0.22}_{-0.22}}$	$\mathbf{159.6^{+0.46}_{-0.46}}$	$\mathbf{29.5^{+2.6}_{-2.6}}$	$\mathbf{18.0^{+0.8}_{-0.8}}$	$\mathbf{69.2^{+7.6}_{-7.6}}$
378091	**20961**	**μ**	$\mathbf{12.5^{+28.5}_{-5.4}}$	$\mathbf{14.7^{+0.20}_{-0.20}}$	$\mathbf{50.0^{+0.13}_{-0.13}}$	$\mathbf{26.3^{+2.4}_{-2.4}}$	$\mathbf{15.6^{+26.9}_{-4.4}}$	$\mathbf{10.8^{+0.0}_{-0.0}}$
04-06 e^-p								
404346	**164**	**e**	$\mathbf{42.0^{+1.6}_{-1.6}}$	$\mathbf{42.0^{+0.25}_{-0.25}}$	$\mathbf{102.1^{+0.30}_{-0.30}}$	$\mathbf{31.2^{+2.5}_{-2.5}}$	$\mathbf{43.6^{+1.6}_{-1.6}}$	$\mathbf{86.1^{+7.6}_{-7.6}}$
404738	62148	e	$20.7^{+1.1}_{-1.1}$	$98.5^{+0.25}_{-0.25}$	$-7.5^{+0.30}_{-0.30}$	$23.7^{+1.6}_{-1.6}$	$44.4^{+2.0}_{-2.0}$	$4.4^{+0.0}_{-0.0}$
406539	**88131**	**e**	$\mathbf{39.8^{+1.3}_{-1.3}}$	$\mathbf{11.4^{+0.22}_{-0.22}}$	$\mathbf{49.7^{+0.59}_{-0.59}}$	$\mathbf{25.8^{+5.0}_{-5.0}}$	$\mathbf{51.7^{+3.5}_{-3.5}}$	$\mathbf{4.4^{+0.0}_{-0.0}}$
407425	56163	e	$38.8^{+1.6}_{-1.6}$	$51.3^{+0.25}_{-0.25}$	$8.8^{+0.30}_{-0.30}$	$7.5^{+2.7}_{-2.7}$	$38.5^{+1.6}_{-1.6}$	$89.6^{+2.4}_{-2.4}$
409714	171564	e	$37.0^{+1.4}_{-1.4}$	$25.6^{+0.22}_{-0.22}$	$100.2^{+0.46}_{-0.46}$	< 2	$37.0^{+1.4}_{-1.4}$	< 5
423369	104898	e	$41.5^{+1.5}_{-1.5}$	$25.4^{+0.22}_{-0.22}$	$-140.6^{+0.46}_{-0.46}$	$20.0^{+2.1}_{-2.1}$	$31.8^{+1.4}_{-1.4}$	$20.1^{+2.0}_{-2.0}$
423713	6544	e	$34.2^{+1.3}_{-1.3}$	$28.7^{+0.22}_{-0.22}$	$23.8^{+0.46}_{-0.46}$	$12.9^{+2.0}_{-2.0}$	$31.8^{+1.2}_{-1.2}$	$24.1^{+2.1}_{-2.1}$
431900	126061	e	$32.2^{+1.1}_{-1.1}$	$16.4^{+0.22}_{-0.22}$	$168.2^{+0.59}_{-0.59}$	$22.8^{+2.0}_{-2.0}$	$33.1^{+1.2}_{-1.2}$	$24.1^{+2.1}_{-2.1}$
450554	13348	e	$14.7^{+0.5}_{-0.5}$	$11.7^{+0.22}_{-0.22}$	$173.6^{+0.59}_{-0.59}$	$15.2^{+1.9}_{-1.9}$	$21.4^{+1.0}_{-1.0}$	$12.2^{+0.0}_{-0.0}$
455992	98112	e	$26.4^{+1.3}_{-1.3}$	$108.5^{+0.25}_{-0.25}$	$127.1^{+0.30}_{-0.30}$	$23.5^{+4.3}_{-4.3}$	$36.5^{+3.1}_{-3.1}$	$12.2^{+0.0}_{-0.0}$
464766	49134	e	$21.7^{+0.7}_{-0.7}$	$8.9^{+0.22}_{-0.22}$	$69.0^{+0.59}_{-0.59}$	< 2	$21.7^{+0.7}_{-0.7}$	< 5
433118	137816	μ	$28.9^{+15.5}_{-7.7}$	$40.5^{+0.39}_{-0.39}$	$-73.5^{+0.06}_{-0.06}$	$24.5^{+2.9}_{-2.9}$	$20.3^{+8.5}_{-4.1}$	$19.3^{+0.0}_{-0.0}$
450757	**67135**	**μ**	$\mathbf{10.8^{+9.4}_{-3.8}}$	$\mathbf{20.6^{+0.26}_{-0.26}}$	$\mathbf{178.7^{+0.09}_{-0.09}}$	$\mathbf{29.0^{+5.1}_{-5.1}}$	$\mathbf{29.5^{+6.0}_{-4.8}}$	$\mathbf{19.3^{+0.0}_{-0.0}}$
465670	**83634**	**μ**	$\mathbf{37.5^{+1.4}_{-1.3}}$	$\mathbf{40.6^{+0.39}_{-0.39}}$	$\mathbf{113.7^{+0.06}_{-0.06}}$	$\mathbf{26.7^{+3.1}_{-3.1}}$	$\mathbf{53.1^{+2.7}_{-2.6}}$	$\mathbf{26.5^{+1.7}_{-1.7}}$
06 e^+p								
476034	70877	e	$30.3^{+1.2}_{-1.2}$	$25.3^{+0.22}_{-0.22}$	$11.0^{+0.46}_{-0.46}$	< 2	$30.3^{+1.2}_{-1.2}$	< 5
476159	**34307**	**e**	$\mathbf{43.0^{+1.5}_{-1.5}}$	$\mathbf{15.8^{+0.22}_{-0.22}}$	$\mathbf{47.6^{+0.59}_{-0.59}}$	$\mathbf{26.3^{+2.5}_{-2.5}}$	$\mathbf{38.3^{+1.2}_{-1.2}}$	$\mathbf{11.5^{+0.0}_{-0.0}}$
483143	38308	e	$23.6^{+0.8}_{-0.8}$	$12.8^{+0.22}_{-0.22}$	$-175.7^{+0.59}_{-0.59}$	< 2	$23.6^{+0.8}_{-0.8}$	< 5
488878	6626	e	$42.3^{+1.4}_{-1.4}$	$15.0^{+0.22}_{-0.22}$	$-49.5^{+0.59}_{-0.59}$	$6.0^{+2.4}_{-2.4}$	$38.5^{+2.0}_{-2.0}$	< 5
473929	**107593**	**μ**	$\mathbf{51.0^{+8.9}_{-6.6}}$	$\mathbf{31.4^{+0.39}_{-0.39}}$	$\mathbf{-116.9^{+0.06}_{-0.06}}$	$\mathbf{48.5^{+5.4}_{-5.4}}$	$\mathbf{41.1^{+4.7}_{-3.7}}$	$\mathbf{< 5}$
477321	57947	μ	$40.9^{+30.2}_{-13.1}$	$24.6^{+0.26}_{-0.26}$	$-85.9^{+0.09}_{-0.09}$	$15.6^{+3.4}_{-3.4}$	$29.8^{+25.8}_{-11.8}$	$75.2^{+6.6}_{-6.6}$

Table 5.4.: Kinematical properties of the selected events in the electron and muon channels for the HERA-2 period. Events with $P_T^X > 25$ GeV are highlighted in bold font. The errors are calculated by propagating the experimental resolutions to the reconstructed variables.

5.2. Combined Results

Figure 5.3 shows the P_T^X distributions of the events in the electron, muon and electron+muon combined channels for the total available e^+p, e^-p and combined $e^\pm p$ data. Table 5.5 shows the numerical values for the same results over the whole P_T^X range and for $P_T^X > 25$ GeV. The signal and background expectation is indicated for every bin. The errors given are statistical and systematic uncertainties added in quadrature.

The overall agreement of the data with the SM expectation is very good, with 53 observed events and 53 ± 6 expected from the SM. About 70% of the data are attributed to W production. Figure 5.4 further demonstrates that the selected events are compatible with W production. It shows the polar angle of the lepton θ_l is typically low (a), the acoplanarity $\Delta\phi(l, X)$ distribution is mostly flat (b) and the transverse lepton-neutrino mass

$$M_T = \sqrt{(P_T^{\mathrm{miss}} + P_T^l)^2 - (\vec{P_T^{\mathrm{miss}}} + \vec{P_T^l})^2}$$

shows a Jacobian peak at $M_T \approx m_W$ typical for W-decays (c).

In the region $P_T^X > 25$ GeV the contribution from W production is predicted to be low. In this region a clear excess of the selected data over the SM expectation is seen in the e^+p data. Here, 9 events are observed in the electron channel where 3.7 ± 0.5 are expected from the SM. In the muon channel, 6 are observed where only 3.2 ± 0.4 are expected. A similar excess is not observed in the e^-p data, where only one event is seen in the electron channel, while 4.3 ± 0.6 are expected. Similarly in the muon channel only one event is observed and 3.3 ± 0.4 are expected. The significance of the excess at $P_T^X > 25$ GeV for all HERA data is only 0.5σ.

The observation of an excess of events at high P_T^X in e^+p was already made in the HERA-1 data. Figure 5.5 shows the rate of events at high P_T^X for all H1 data. The high rate in e^+p data up to 2004 is clearly visible, while the statistics in $2006 \, e^+p$ data are still too low to make a definitive statement on the rate there. Figure 5.6 shows the projected development of the significance of the excess in the e^+p data over the course of 2006 e^+p data taking. The significance of the excess is calculated by assuming that the events are Poisson-distributed fluctuations of the SM background. At the switch to e^+p running in 2006, the significance was $3.4 \, \sigma$ from the combined HERA-1 and 2003-04 e^+p data. The arrival of two events at high P_T^X brought the significance to a maximum of $3.7 \, \sigma$ in early September 2006, but since then no new event at high P_T^X has been observed. If the average rate of isolated leptons at high P_T^X stays at the level observed by H1 so far, the excess can be at the 3.2σ level at the end of data taking. If the rate continues at the level expected by the SM, the excess will decrease to 2.2σ until the end of data taking.

Figure 5.7 shows two events seleted in the HERA-2 e^+p data, a candidate for elastic W production (a) and an event with a prominent hadronic jet, contributing to the excess at high P_T^X (b). Figure 5.8 shows three muon events, one selected in HERA-1 data with high P_T^X (a), one selected in HERA-2 e^-p data close to the threshold of $P_T^X > 25$ GeV (b) and one event selected in the 2006 e^+p data with high P_T^X (c). These event displays demonstrate that the H1 detector at HERA measures spectacular topologies in HERA-1 and HERA-2.
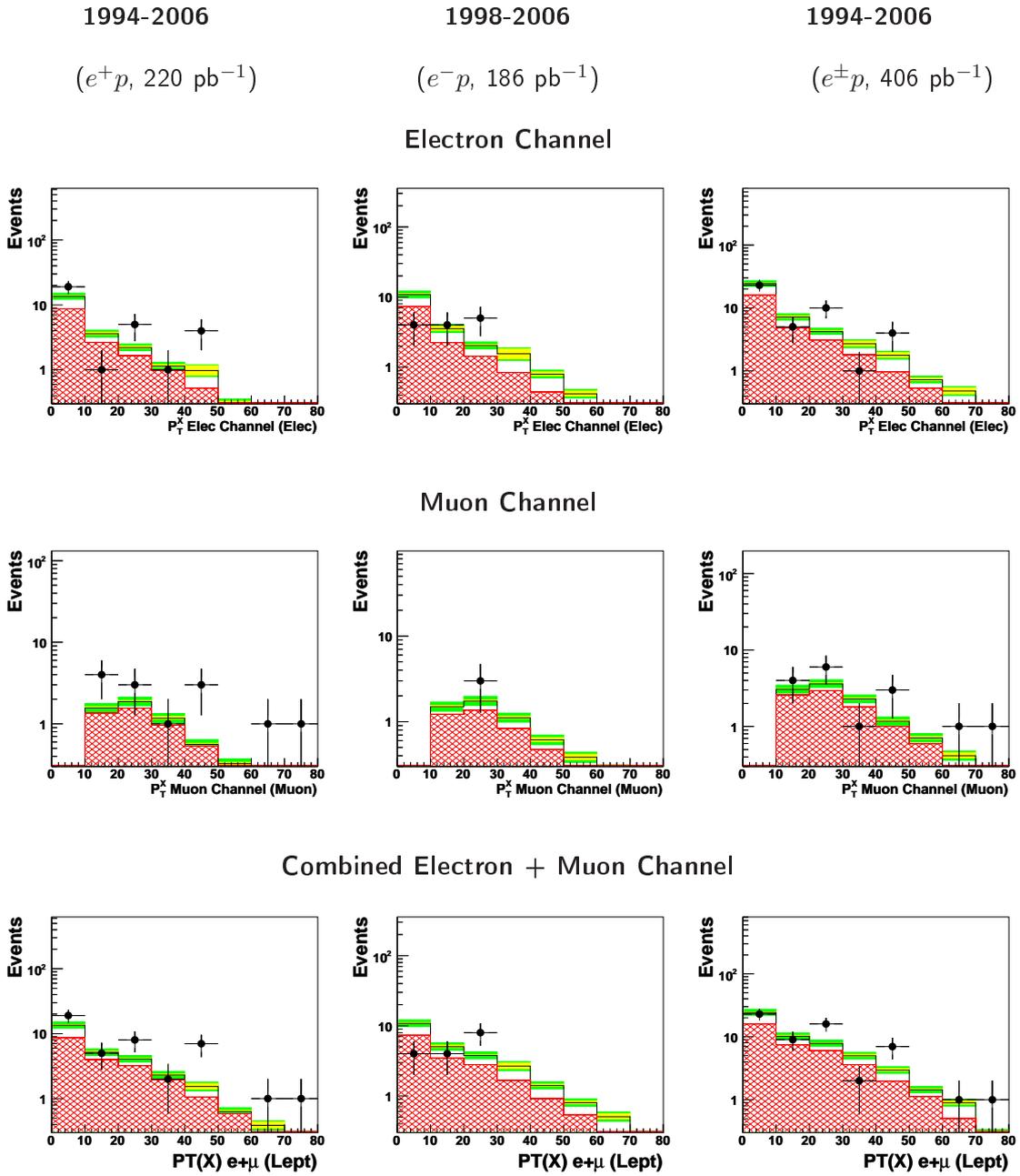
Figure 5.3.: Results in the electron, muon and combined electron+muon channels (arranged in rows) for all e^+p, all e^-p and all HERA $e^\pm p$ data (arranged in columns). The selected data (points) are compared to the SM expectation (open histogram). The statistical and systematic uncertainties added in quadrature are shown as the green band (containing the statistical error as yellow band). The signal component is shown as red hatched histogram. An excess at $P_T^X > 25$ GeV is seen in the e^+p data.

1994-2006 e^+p 220.2 pb^{-1}		H1 Data	SM Expectation	SM Signal	Other SM Processes
Electron	All P_T^X	26	22.41 $\pm$2.73	15.35 $\pm$2.33	7.06 $\pm$0.40
	$P_T^X > 25$ GeV	9	3.69 $\pm$0.51	2.78 $\pm$0.42	0.91 $\pm$0.09
Muon	All P_T^X	11	5.76 $\pm$0.78	4.97 $\pm$0.75	0.79 $\pm$0.03
	$P_T^X > 25$ GeV	6	3.17 $\pm$0.44	2.77 $\pm$0.42	0.39 $\pm$0.02
Combined	All P_T^X	37	28.18 $\pm$3.44	20.32 $\pm$3.08	7.85 $\pm$0.37
	$P_T^X > 25$ GeV	15	6.85 $\pm$0.91	5.55 $\pm$0.84	1.30 $\pm$0.07

1998-2006 e^-p 186.334 pb^{-1}		H1 Data	SM Expectation	SM Signal	Other SM Processes
Electron	All P_T^X	13	19.79 $\pm$2.48	13.04 $\pm$1.98	6.75 $\pm$0.51
	$P_T^X > 25$ GeV	1	4.31 $\pm$0.64	2.42 $\pm$0.37	1.89 $\pm$0.27
Muon	All P_T^X	3	5.76 $\pm$0.75	4.41 $\pm$0.67	1.35 $\pm$0.08
	$P_T^X > 25$ GeV	1	3.36 $\pm$0.44	2.47 $\pm$0.38	0.89 $\pm$0.06
Combined	All P_T^X	16	25.55 $\pm$3.19	17.44 $\pm$2.64	8.11 $\pm$0.55
	$P_T^X > 25$ GeV	2	7.67 $\pm$1.02	4.90 $\pm$0.74	2.78 $\pm$0.28

1994-2006 $e^{\pm}p$ 406.635 pb^{-1}		H1 Data	SM Expectation	SM Signal	Other SM Processes
Electron	All P_T^X	39	42.20 $\pm$5.12	28.39 $\pm$4.30	13.82 $\pm$0.83
	$P_T^X > 25$ GeV	10	8.00 $\pm$1.09	5.21 $\pm$0.79	2.79 $\pm$0.30
Muon	All P_T^X	14	11.52 $\pm$1.51	9.38 $\pm$1.42	2.14 $\pm$0.08
	$P_T^X > 25$ GeV	7	6.53 $\pm$0.85	5.25 $\pm$0.80	1.28 $\pm$0.06
Combined	All P_T^X	53	53.73 $\pm$6.54	37.77 $\pm$5.72	15.96 $\pm$0.83
	$P_T^X > 25$ GeV	17	14.53 $\pm$1.87	10.45 $\pm$1.58	4.07 $\pm$0.28

Table 5.5.: Results in the electron, muon and combined electron+muon channels for all e^+p, all e^-p and all HERA data. An excess at $P_T^X > 25$ GeV is seen in the e^+p data.

a) b) c)
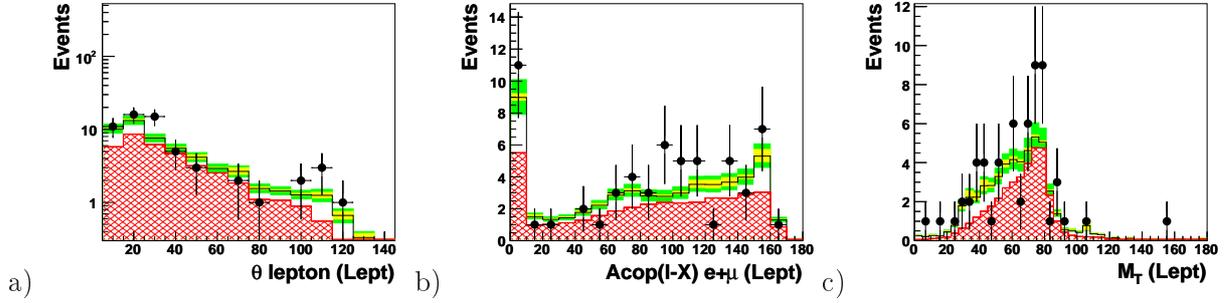
Figure 5.4.: The final data selection in the combined electron and muon channels for the complete 1994-2006 $e^{\pm}p$ HERA data compared to the SM expectation (open histogram). The signal component (red hatched histogram) dominates the SM expectation and follows the distributions of the data events: a) The polar angle of the lepton θ_l is typically low. b) The acoplanarity $\Delta\phi(l, X)$ distribution is mostly flat (the zero bin contains the events with low hadronic transverse momentum where acoplanarity is not defined). c) The transverse lepton-neutrino mass M_T shows a Jacobian peak at $M_T \approx m_W$ typical for W-decays.

▲ electrons   ▼ muons
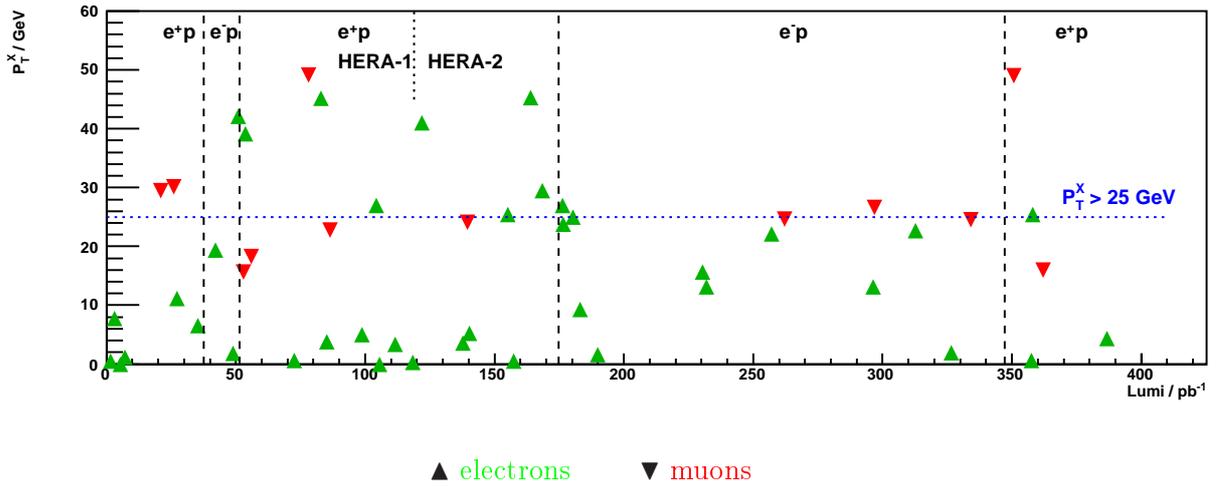
Figure 5.5.: Distribution of the P_T^X values of isolated lepton events in all HERA data.

55

Projected Development of H1 Excess Significance

Lumi extrapolation based on last 28 days

Significance [σ]

$p_T{}^X > 25$ GeV, $N_{obs} = 17$
in 240 pb^{-1} of e^+p data

● Observed Significance

today

● Future rate as observed by H1
  ± 1σ fluctuation on H1 rate

● Future rate as predicted by SM
  ± 1σ fluctuation on SM rate

Jul Aug Sep Oct Nov Dec Jan Feb Mar Apr May Jun
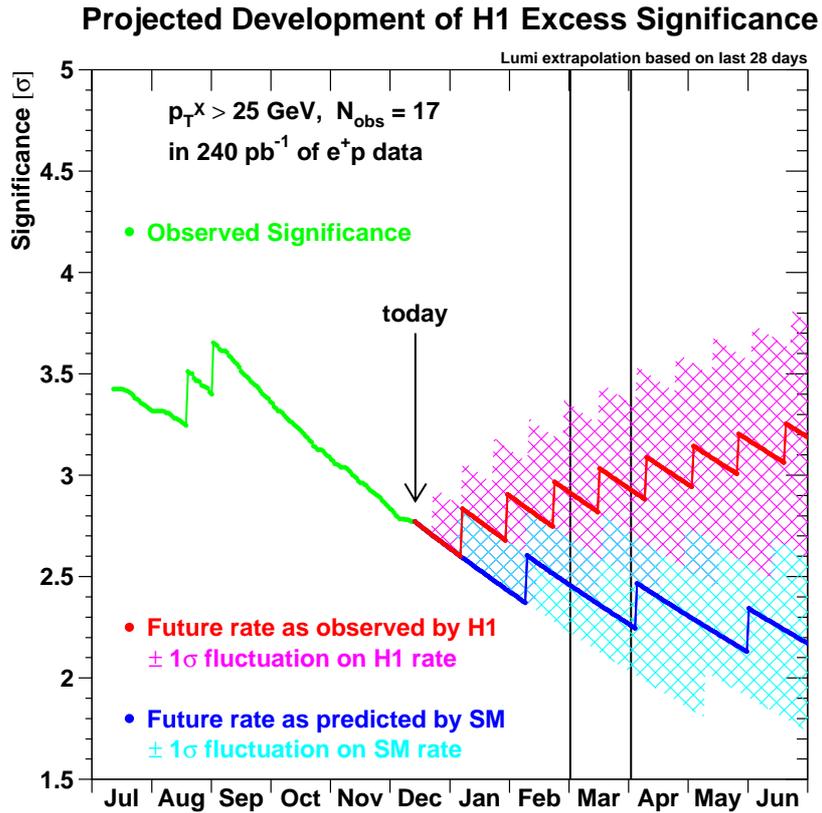
Figure 5.6.: Previous and projected development of H1 isolated leptons excess significance in e^+p during 2006-07 e^+p data taking. At the switch to e^+p in July 2006 the significance was 3.4σ from 1994-2004 e^+p data. "Today" marks 13 December 2006, where the excess in e^+p was 2.7σ. If the average rate of events at $P_T^X > 25$ GeV is upheld, the excess can be 3.2σ by the end of data taking (red line). If events at $P_T^X > 25$ GeV are only coming in at the rate expected from the SM, the excess will be of 2.2σ significance at the end of HERA (blue line).
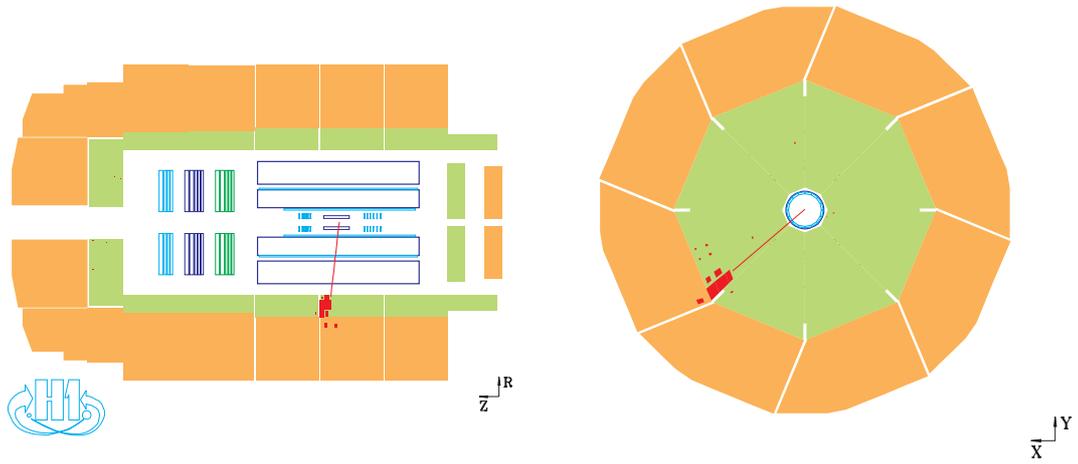
a) $e + P_T^{\mathrm{miss}}$ in HERA-2 e^+p data: $P_T^e = 47$ GeV, $P_T^{\mathrm{miss}} = 47$ GeV
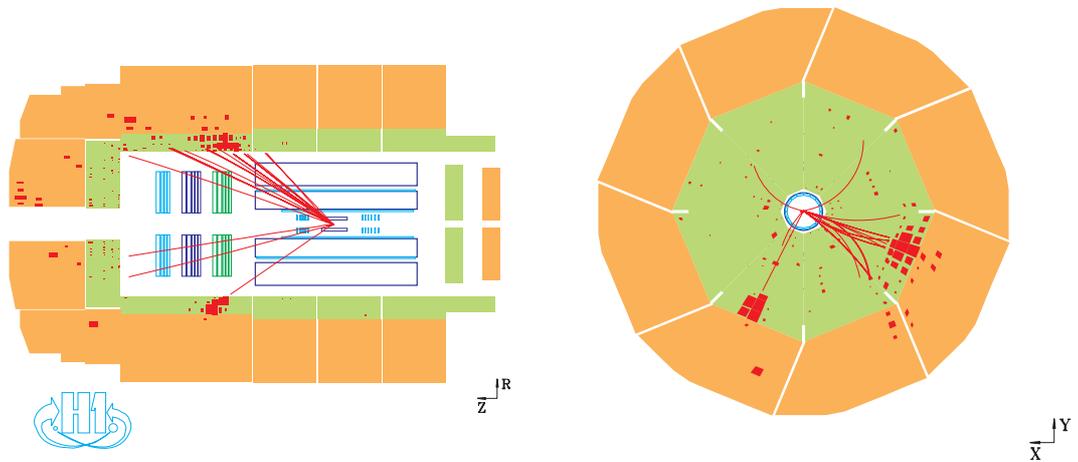
b) $e + P_T^{\mathrm{miss}}$ in HERA-1 e^+p data: $P_T^e = 37$ GeV, $P_T^{\mathrm{miss}} = 44$ GeV, $P_T^X = 29$ GeV

Figure 5.7.: Events with isolated electrons and missing transverse momentum at high P_T^X observed in HERA-2 e^+p data. a) A candidate for elastic W production. b) An event with a prominent hadronic jet.
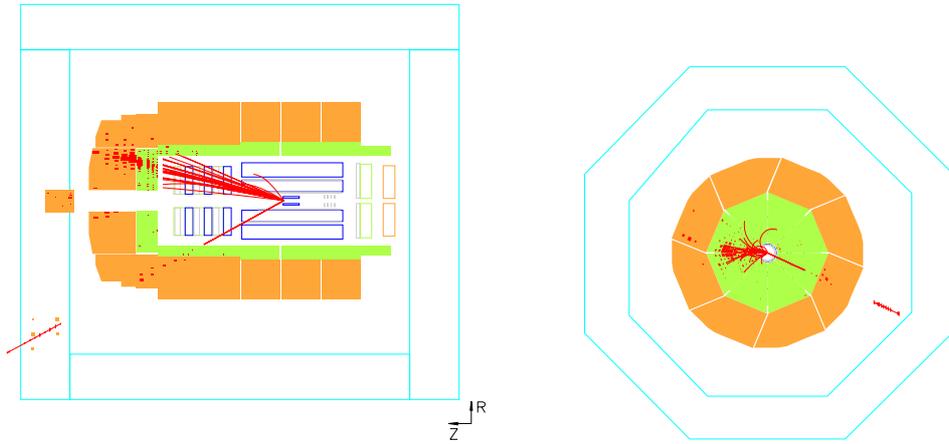
a) $\mu + P_T^{\mathrm{miss}}$ in HERA-1 e^+p data: $P_T^{\mu} = 28$ GeV, $P_T^{\mathrm{miss}} = 43$ GeV, $P_T^X = 67$ GeV
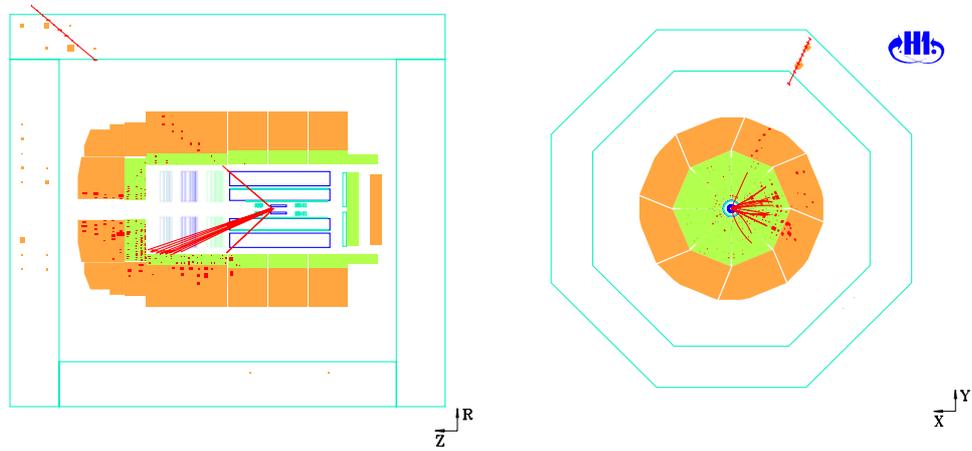
b) $\mu + P_T^{\mathrm{miss}}$ in HERA-2 e^-p data: $P_T^{\mu} = 38$ GeV, $P_T^{\mathrm{miss}} = 51$ GeV, $P_T^X = 24.7$ GeV
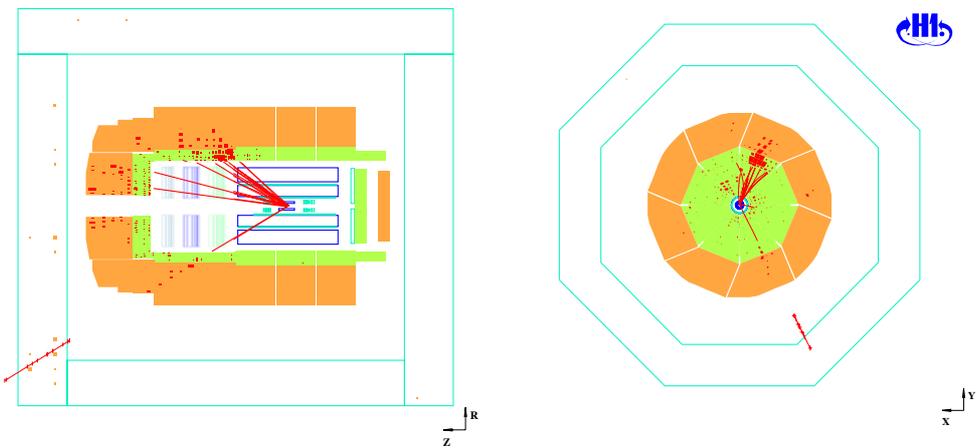
c) $\mu + P_T^{\mathrm{miss}}$ in HERA-2 e^+p data: $P_T^{\mu} = 51$ GeV, $P_T^{\mathrm{miss}} = 39$ GeV, $P_T^X = 48$ GeV

Figure 5.8.: Events with isolated muons and missing transverse momentum at high P_T^X observed in HERA-1 and HERA-2 data.

5.3. Background Studies

To verify that the background contributions are well under control special selections are made where large background sources are enriched so that the data can be compared with high statistics to the corresponding background prediction. For the electron channel, NC and CC enriched samples are used. For the muon channel lepton pair production (LP) and CC enriched samples are selected. The selection criteria for the control samples are summarised in Tab. 5.6. Also shown is the number of events selected in the 2004-06 e^-p data compared to the SM expectation. The percentage of the dominating background is given in parentheses and demonstrates for all control samples that they are indeed dominated by the selected background. The large errors in muon channel control samples are due to statistical limitations of the Monte Carlo samples.

Because the expected backgrounds and experimental conditions are different for the e^+p and e^-p data samples, all control distributions are shown for the 2003-06 e^+p and 2004-06 e^-p data samples separately, to demonstrate that any observed difference is not a systematic effect. The definition of the control samples also follows the HERA-1 definitions, expect for the muon CC enriched control sample. The cuts in this sample were relaxed to increase its statistical significance. It should be noted that the final selection of electron events is included in the electron NC enriched control samples, and the final selection of muon events is now included in the muon CC enriched control sample. The control samples are discussed in detail in the following.

5.3.1. NC in the Electron Channel

The NC enriched sample is used to control background where the electron is real but missing energy arises due to fluctuations in the energy measurement only. The selection of the sample is shown in Tab. 5.6. Figure 5.9 shows the data selected in the NC enriched samples for the 2003-06 e^+p period and Fig. 5.10 for the 2004-06 e^-p period. The P_T^{calo} (a), P_T^X (b) P_T^e (c) are well described to high values. The electron polar angle θ_e (d) is described within the errors also in the central and forward direction where the signal is expected. The longitudinal momentum balance $(E - P_z)$ (e) is well described in the main peak at 55 GeV and at lower values where longitudinal momentum in the event is not measured. This gives confidence, that the NC background is well estimated in the electron channel. Figure 5.11 shows the event yield for the enriched NC selection as function of the collected integrated luminosity. The yield is flat within the statistical errors over the whole data period, giving confidence that no time-dependent systematic effects are influencing the event yield in the electron channel.

5.3.2. CC in the Electron Channel

The CC enriched control sample is used to test background where the missing transverse momentum is real, but the electron candidate is falsely identified. The selection of the sample is shown in Tab. 5.6. Figures 5.12 and 5.13 show the data selected in the CC enriched control samples for the 2003-06 e^+p and 2004-06 e^-p data periods, respectively. P_T^{calo} (a) and P_T^X (b) are well described to high values. The transverse momentum P_T^e (c) and polar angle θ_e (d) of the falsely identified electron are well described within the errors where the signal is expected.

Control Samples	Common Phase Space		
	$P_T^{\mathrm{calo}} > 12$ GeV	$P_T^l > 10$ GeV	$5° < \theta_l < 140°$
Electron Channel	**NC Enriched**		**CC Enriched**
	e not in cracks		$V_{ap}/V_p < 0.15$
	e isolated from HFS		$\zeta_e^2 > 5000$ GeV^2
	$D_{\mathrm{track}} > 0.5$		$\Delta\varphi(e, X) < 160°$
	$D_{\mathrm{jet}} > 1.0$		$\delta^{\mathrm{miss}} > 5$ GeV
Data (04-06 e^-p)	4716		137
Total SM	4080 ± 1204		165 ± 44
	(98% NC)		(89% CC)
Muon Channel	**CC Enriched**		**LP Enriched**
	$P_T^{\mathrm{miss}} > 12$ GeV		$V_{ap}/V_p < 0.2$
	$P_T^X > 12$ GeV		μ isolated from HFS
	$V_{ap}/V_p < 0.5$ (< 0.15 if $\mathrm{P}_T^{\mathrm{calo}} < 25$ GeV)		$D_{\mathrm{jet}} > 1.0$
	$P_T^{\mathrm{calo}} > 25$ GeV		
	(if $\zeta_e^2 < 5000$ GeV^2)		
Data (04-06 e^-p)	21		28
Total SM	30 ± 8		37 ± 8
	(70% CC)		(67% LP)

Table 5.6.: Selection requirements for the electron and muon channel background control samples. The number of selected events compared to the SM expectation is shown exemplary for the 2004-06 e^-p data. The dominant contribution to the SM expectation is indicated as percentage.

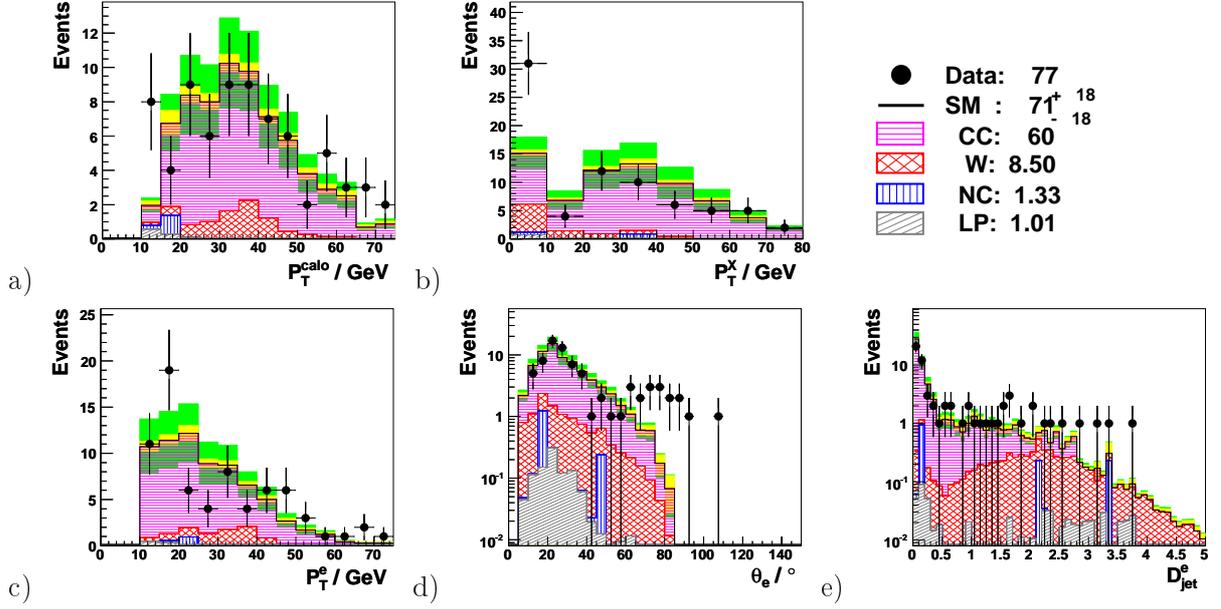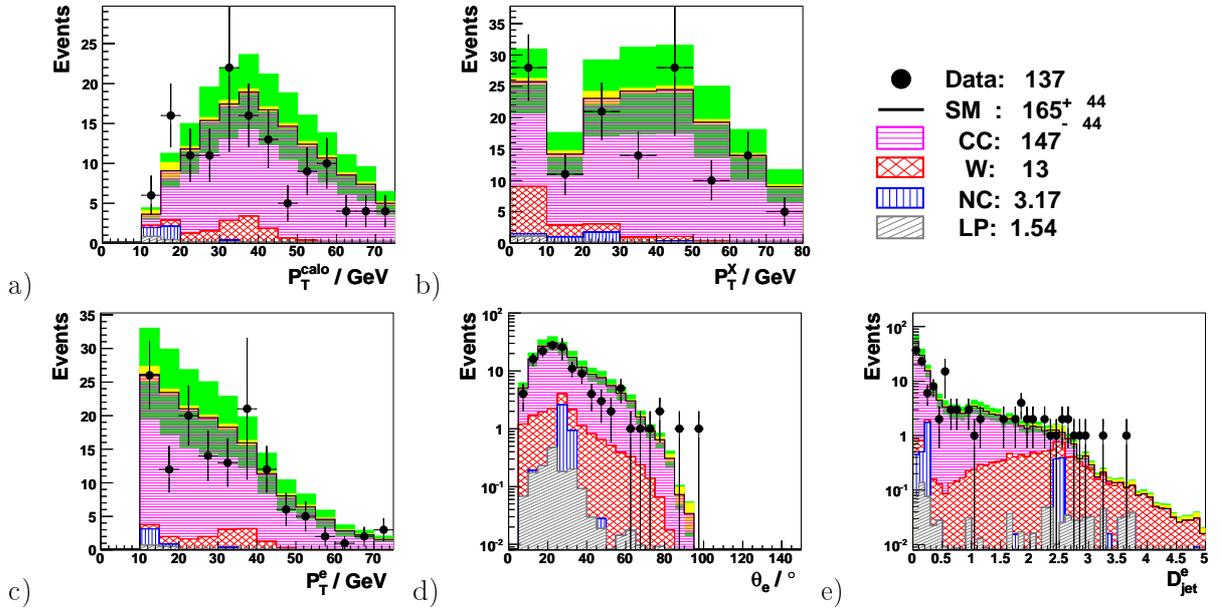Electron Channel – NC Enriched (2003-06, e^+p)
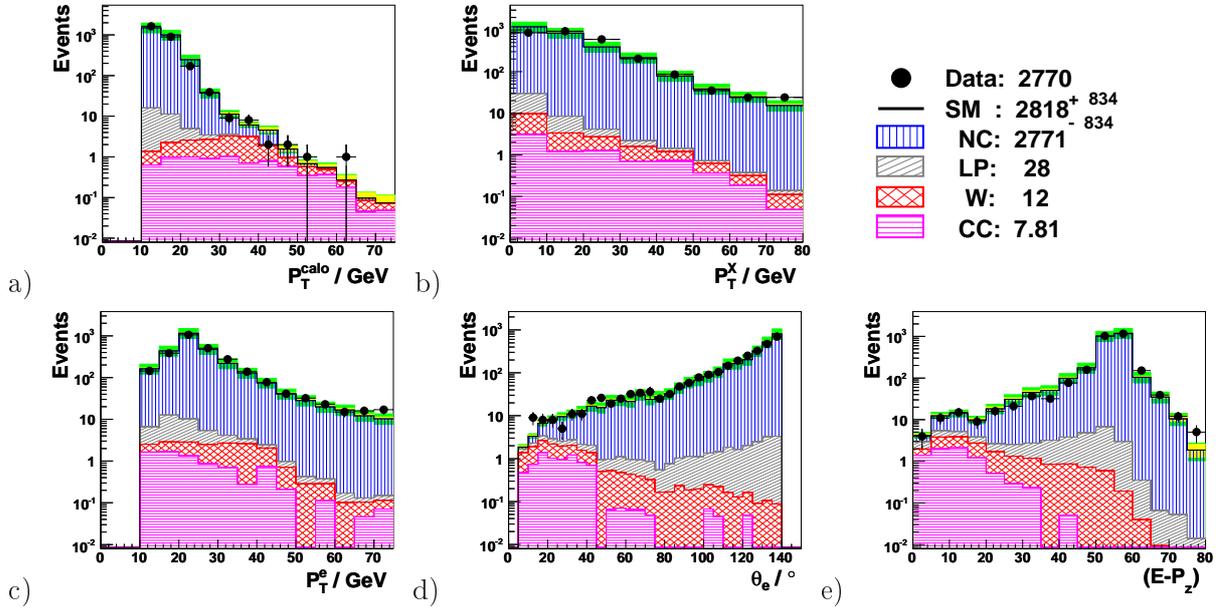
Figure 5.9.: Distributions of data selected in the electron channel NC enriched control sample for the 2003-06 e^+p period compared to the SM expectation.

Electron Channel – NC Enriched (2004-06, e^-p)
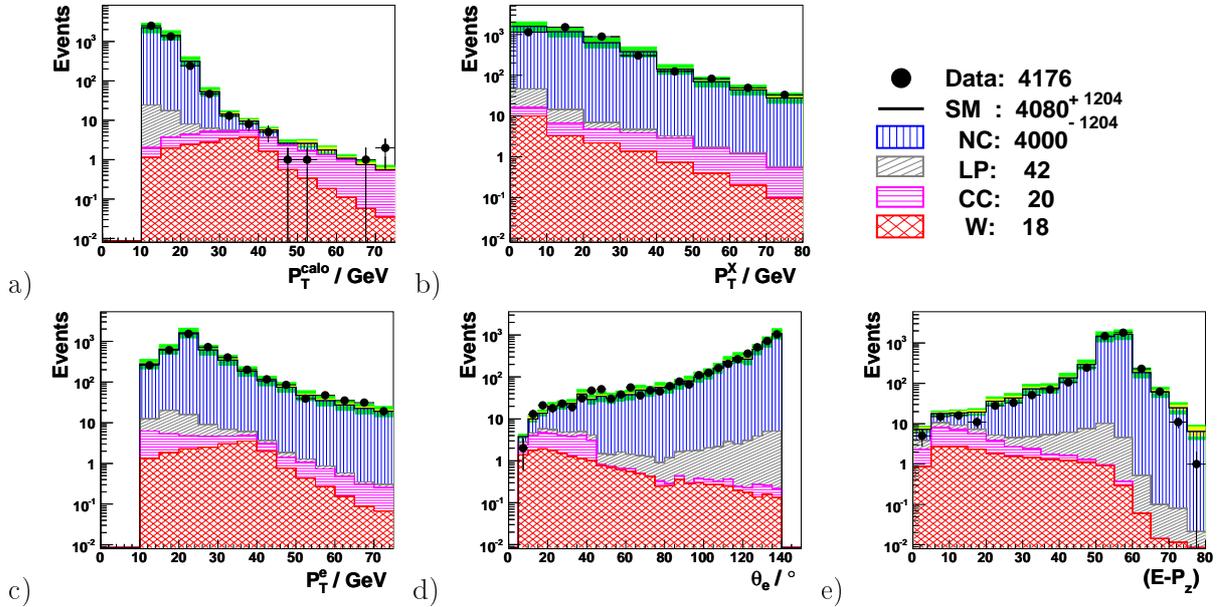
Figure 5.10.: Distributions of data selected in the electron channel NC enriched control sample for the 2004-06 e^-p period compared to the SM expectation.
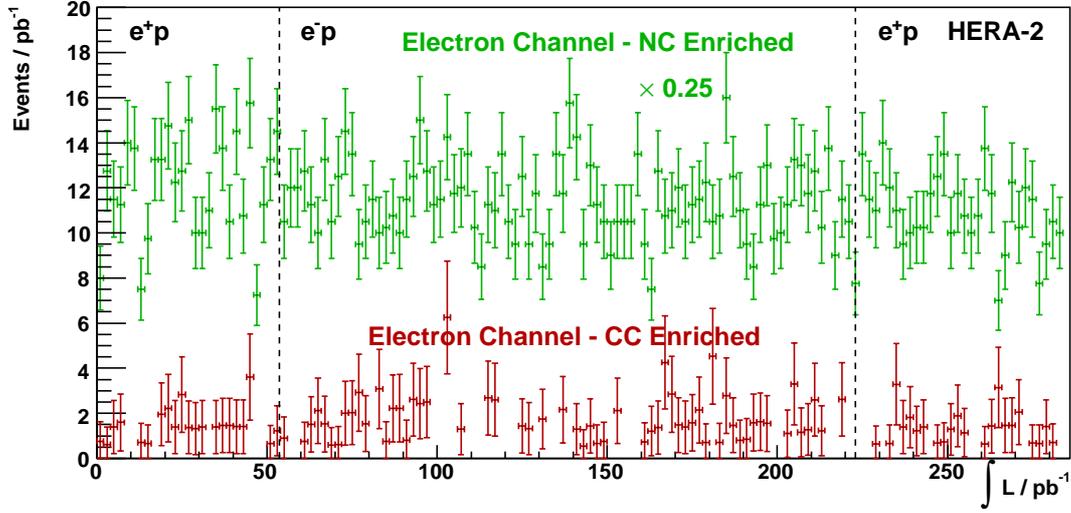
Figure 5.11.: Event yields in the electron channel control samples for the analysed HERA-2 $e^{\pm}p$ data. Shown is the number of events selected per 1 pb^{-1} for the NC enriched sample (green, scaled by $\times 0.25$) and the CC enriched sample (red) over the integrated luminosity. The yields are flat within the statistical errors (shown). The final electron sample is contained in the enriched NC sample.

The distance to jets D_{jet} (e) peaks at low values, which is more evidence that electrons in this sample are indeed misidentified hadrons. The excess of events at $P_T^X < 10$ GeV in the e^+p sample is due to remaining electronic noise in the data which is not included in the simulation. These events are ep collision events where a charged hadron from the vertex is falsely identified as an electron due to the same single hot cell overlaying nine of the events at $P_T^X < 10$ GeV. The same events are visible around $\theta_e \simeq 100°$. None of these events enters the final sample. Overall the description gives confidence that the CC contribution to the background in the electron channel is well estimated. The CC enriched sample does not fully include the final sample because the cut on V_{ap}/V_p is slightly relaxed in the final selection to maximise acceptance for events with large P_T^X.

5.3.3. CC in the Muon Channel

The CC enriched sample is used to control background from CC events where the muon is either falsely identified or part of the jet. The selection of the sample is shown in Tab. 5.6. Figures 5.14 and 5.15 show the data selected in the CC enriched control sample for the $2003 - 06$ e^+p and $2004 - 06$ e^-p periods, respectively. For both periods the NC prediction in the sample suffers from low statistics in the Monte Carlo sample, resulting in a statistical error of 50% on that contribution. This problem is most prominent at $\theta_\mu < 10°$. Within these errors, P_T^μ (a) and θ_μ (b) are reasonably well described. The distance of muons to jets D_{jet} (c) and the V_{ap}/V_p (d) both peak at low values as expected for muons that are part of the hadronic final state in CC events.

Figure 5.12.: Data selected in the electron channel CC enriched control sample for the 2003-06 e^+p period compared to the SM expectation. The excess at low P_T^X is due to electronic noise (see text).

Figure 5.13.: Data selected in the electron channel CC enriched control sample for the 2004-06 e^-p period compared to the SM expectation.
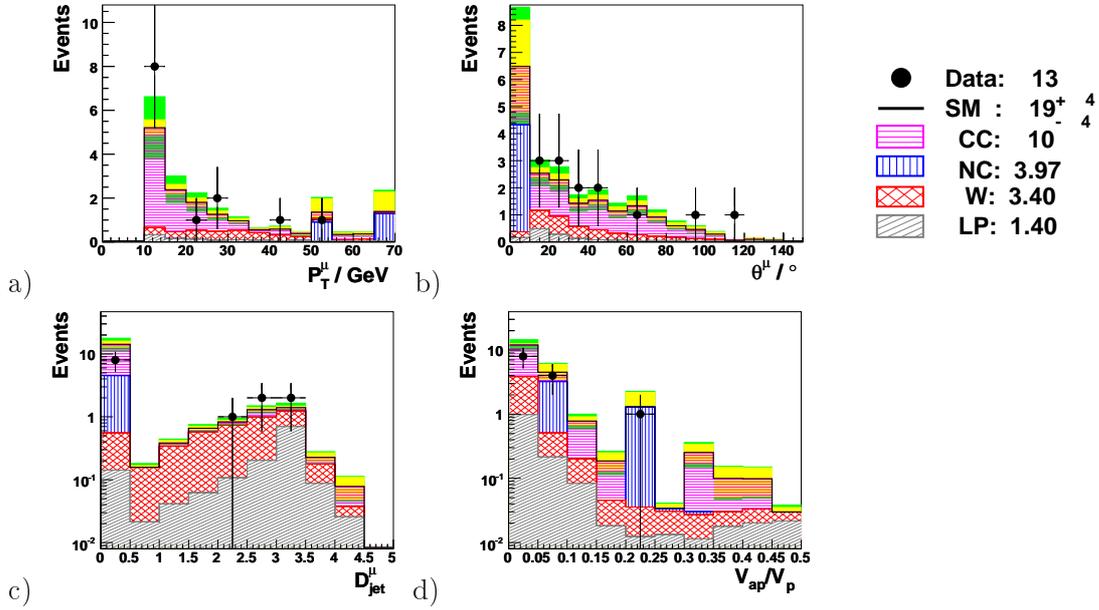
Figure 5.14.: Distribution of events selected in the muon channel CC enriched control sample for the $2003 - 06$ e^+p data. The description of forward muons has a large statistical error (yellow band) from the NC contribution.
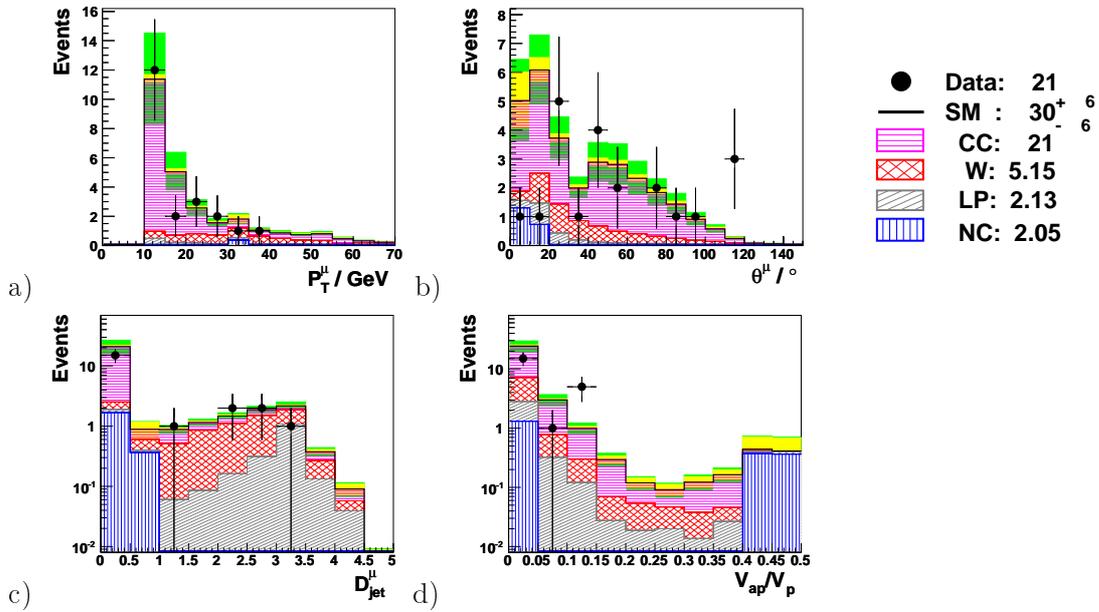
Figure 5.15.: Distribution of events selected in the muon channel CC enriched control sample for the $2004 - 06$ e^-p data.

Muon Channel – Lepton Pair Enriched, 2003-06 $\mathbf{e^+p}$

a)   b)
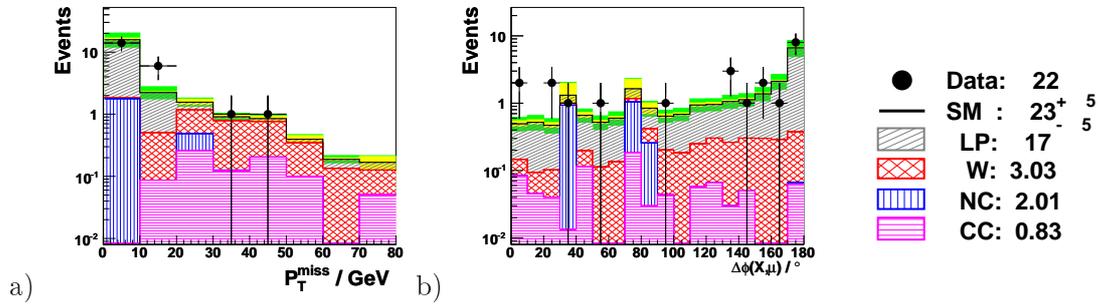
Figure 5.16.: Distribution of events selected in the muon channel lepton pair production enriched control sample for the 2003-06 e^+p data.

Muon Channel – Lepton Pair Enriched, 2004-06 $\mathbf{e^-p}$

a)   b)
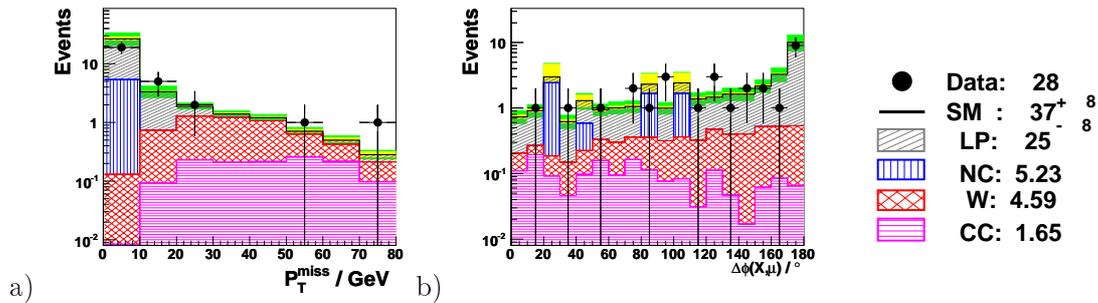
Figure 5.17.: Distribution of events selected in the muon channel lepton pair production enriched control sample for the 2004-06 e^-p data.

5.3.4. Lepton Pair Production in the Muon Channel

The lepton pair production enriched sample is used to estimate background from lepton pair production that enters the sample because one of the leptons is not detected, causing apparent missing transverse momentum. The selection of the sample is shown in Tab. 5.6. Figures 5.16 and 5.17 show the data selected in the lepton pair enriched sample for the 2003-06 e^+p and 2004-06 e^-p periods, respectively. The background prediction is dominated by lepton pair production. Again due to statistical limitations of the Monte Carlo the NC contribution seems large but has an error of 50%. P_T^{miss} is well described to high values (a). $\Delta\varphi(\mu, X)$ peaks at 180° as expected for lepton pair production (b). The expectation agrees well with the data within the high statistical errors, giving confidence that the pair production background is well understood.
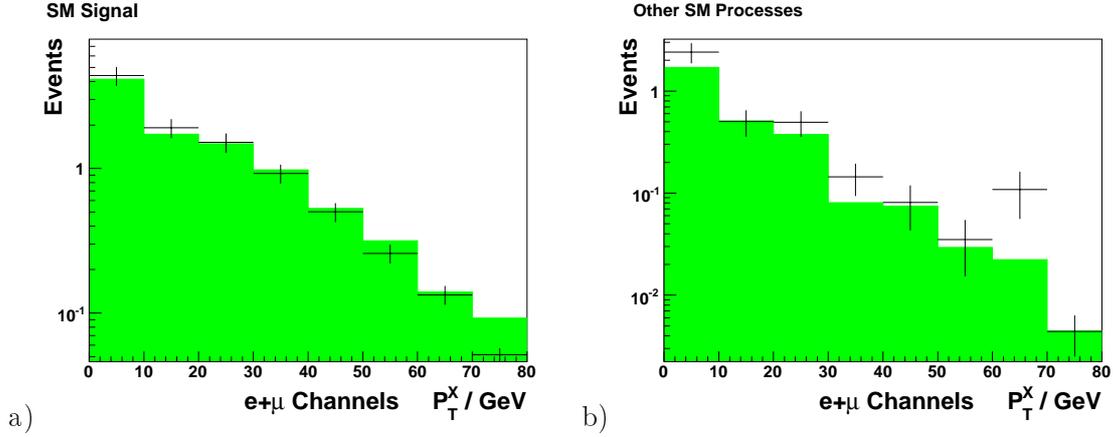
Figure 5.18.: Comparison of the predicted P_T^X distributions for HERA-1 e^+p data in the combined electron and muon channels in the reanalysis (black crosses) and the published results (filled histogram). a) The SM signal expectation. b) The SM background expectation. The errors shown on the reanalysis are total systematic and statistical errors combined in quadrature.

5.4. Reanalysis of HERA-1 Data

Since the publication of the H1 paper on isolated leptons in HERA-1 [4] the H1 analysis software has been completely rewritten. The new software takes into account progress in detector understanding and unifies calibrations and the lepton and final state identification algorithms. Also the full description of the HERA-2 experimental setup is only available in the new software. Because it is imperative for signature searches such as those presented in this thesis to present additional data in a phase space compatible with the previous phase space, the HERA-1 data were fully reanalysed.

The reanalysed HERA-1 results where obtained by running the analysis identically to the HERA-2 analysis described in this chapter with the only differences coming from changes in the experimental setup. For an overall comparison of the previous and new final rates the integrated tables for the electron and muon event selections from the paper and this reanalysis are shown in Tab. 5.7. Compared to the paper, no events selected previously are lost. Five new electron events enter the HERA-1 e^+p sample, and one event enters the e^-p sample, all at low P_T^X. One muon event previously at $P_T^X > 25$ GeV is now reconstructed at $P_T^X < 25$ GeV.

In Fig. 5.18 the published distributions of P_T^X for the combined electron and muon channels are compared to the reanalysis for the signal prediction (a) and the background prediction (b). The signal prediction is compatible between the two analyses within the errors. From Tab. 5.7 it is visible that the background prediction for the muon channel is compatible within the errors between the two analyses. The total background prediction for the electron channel increases roughly by a factor of ~ 1.3 compared to the paper, which explains the increase in event yield in this region for the reanalysis.

Table 5.8 shows the recalculated kinematics of all electron and muon events selected in HERA-1 data. The new events are emphasised. Errors on the kinematical values are calculated by

Previously published event yields

1994-2000 e^+p 104.7 pb^{-1}		H1 Data	SM expectation	SM Signal	Other SM processes
Electron	Total	10	9.85 ± 1.27	7.17 ± 1.17	2.68 ± 0.49
	$P_T^X > 25$ GeV	4	1.48 ± 0.25	1.27 ± 0.24	0.22 ± 0.06
Muon	Total	8	2.55 ± 0.44	2.23 ± 0.43	0.33 ± 0.08
	$P_T^X > 25$ GeV	6	1.44 ± 0.25	1.29 ± 0.25	0.15 ± 0.04
Combined	Total	18	12.40 ± 1.69	9.40 ± 1.60	3.00 ± 0.53
	$P_T^X > 25$ GeV	10	2.92 ± 0.49	2.55 ± 0.49	0.37 ± 0.09

Reanalysis

1994-2000 e^+p 106.5 pb^{-1}		H1 Data	SM Expectation	SM Signal	Other SM Processes
Electron	All P_T^X	15	10.82 ± 1.33	7.44 ± 1.13	3.38 ± 0.20
	$P_T^X > 25$ GeV	4	1.70 ± 0.24	1.31 ± 0.20	0.40 ± 0.04
Muon	All P_T^X	8	2.63 ± 0.36	2.28 ± 0.35	0.35 ± 0.02
	$P_T^X > 25$ GeV	5	1.41 ± 0.20	1.26 ± 0.19	0.15 ± 0.01
Combined	All P_T^X	23	13.45 ± 1.65	9.72 ± 1.47	3.73 ± 0.18
	$P_T^X > 25$ GeV	9	3.11 ± 0.42	2.57 ± 0.39	0.54 ± 0.03

Table 5.7.: HERA-1 1994-2000 e^+p results on isolated electrons and muons from the paper [4] (upper table) and the reanalysis (lower table). The number of observed events is compared to the SM expectation. The statistical and systematic uncertainties added in quadrature are indicated. The total background prediction for the electron channel of 2.68 ± 0.49 in the publication increases to 3.38 ± 0.2 in the reanalysis.

propagating the experimental resolutions to the reconstructed variables. To compare the recalculated kinematics easily with the previously published kinematics, Fig. 5.19 shows so-called parallel coordinate plots comparing the kinematics of HERA-1 candidates as published in the HERA-1 paper to the recalculated kinematics of the same events. Parallel coordinate plots were developed to make trends in multi-dimensional data sets quickly visible [52]. Here, 540 numerical values are visualised: mean and errors for five variables of 18 events comparing results from two analyses. The red line showing the $P_T > 25$ GeV threshold demonstrates that all events are reconstructed in the same P_T^X bin except for one muon event[1]. Two muon events have been reconstructed with very large errors in the previous analysis. It is suspected, that this comes from a change in the track reconstruction, leading to a different track hypothesis. One muon event has a larger error in the reanalysis. For two events at high P_T^X, the inclusive hadronic angle γ_h points to a different region of the detector. For two other events where this is also the case the P_T^X is very low which is likely caused by stronger noise suppression in the new software. The details of these differences remain to be investigated.

In summary, the previously published results and the results of this thesis agree well within the errors. No isolated lepton event selected in HERA-1 is lost. Five new electron events enter the HERA-1 e^+p sample at low P_T^X were the new signal prediction is also slightly higher. One new electron enters the e^-p sample, also at low P_T^X. In summary, the previous analysis of isolated leptons in HERA-1 and this reanalysis are fully comparable and reliable updates with HERA-2 data can be made.

---

[1] Run 270132 event 73115.

Run	Event	Lepton	P_T^l / GeV	θ_l / $^\circ$	φ_l / $^\circ$	P_T^X / GeV	P_T^{miss} / GeV	γ_h / $^\circ$
94-97 e^+p								
87226	*82972*	*e*	$14.2^{+0.5}_{-0.5}$	$5.3^{+0.22}_{-0.22}$	$-75.2^{+0.59}_{-0.59}$	< 2	$14.2^{+0.5}_{-0.5}$	< 5
90264	313	e	$39.0^{+1.4}_{-1.4}$	$27.0^{+0.22}_{-0.22}$	$157.7^{+0.46}_{-0.46}$	$7.0^{+0.9}_{-0.9}$	$32.7^{+1.6}_{-1.6}$	$11.7^{+1.6}_{-1.6}$
123443	*99268*	*e*	$24.8^{+1.2}_{-1.2}$	$121.3^{+0.25}_{-0.25}$	$-54.0^{+0.30}_{-0.30}$	< 2	$25.8^{+1.2}_{-1.2}$	< 5
130611	*35015*	*e*	$35.8^{+1.2}_{-1.2}$	$15.5^{+0.22}_{-0.22}$	$84.3^{+0.59}_{-0.59}$	$2.6^{+0.5}_{-0.5}$	$36.8^{+1.2}_{-1.2}$	< 5
186729	**702**	**μ**	$\mathbf{76.2^{+233.3}_{-33.8}}$	$\mathbf{30.0^{+0.39}_{-0.4}}$	$\mathbf{-154.7^{+0.06}_{-0.06}}$	$\mathbf{76.1^{+5.4}_{-5.4}}$	$\mathbf{31.0^{+226.1}_{-15.2}}$	< 5
188108	**5066**	**μ**	$\mathbf{41.7^{+5.3}_{-4.2}}$	$\mathbf{35.1^{+0.39}_{-0.39}}$	$\mathbf{162.5^{+0.06}_{-0.06}}$	$\mathbf{29.7^{+2.4}_{-2.4}}$	$\mathbf{44.8^{+4.1}_{-3.3}}$	< 5
192227	**6208**	**μ**	$\mathbf{74.3^{+13.8}_{-10.0}}$	$\mathbf{28.6^{+0.26}_{-0.26}}$	$\mathbf{-1.7^{+0.09}_{-0.09}}$	$\mathbf{66.0^{+6.8}_{-6.8}}$	$\mathbf{21.1^{+7.2}_{-5.4}}$	< 5
195308	**16793**	**μ**	$\mathbf{61.2^{+20.0}_{-12.1}}$	$\mathbf{30.9^{+0.39}_{-0.39}}$	$\mathbf{149.0^{+0.06}_{-0.06}}$	$\mathbf{29.5^{+2.9}_{-2.9}}$	$\mathbf{35.5^{+17.1}_{-11.3}}$	$\mathbf{27.4^{+2.6}_{-2.6}}$
196406	38438	e	$13.9^{+0.5}_{-0.5}$	$7.2^{+0.22}_{-0.22}$	$-89.1^{+0.59}_{-0.59}$	$10.9^{+2.0}_{-2.0}$	$20.4^{+1.6}_{-1.6}$	$59.6^{+12.1}_{-12.1}$
201082	*2759*	*e*	$22.2^{+0.8}_{-0.8}$	$13.0^{+0.22}_{-0.22}$	$90.8^{+0.59}_{-0.59}$	$6.3^{+1.0}_{-1.0}$	$41.8^{+1.3}_{-1.3}$	< 5
98-99 e^-p								
236176	3849	e	$10.2^{+0.4}_{-0.4}$	$12.0^{+0.22}_{-0.22}$	$134.7^{+0.59}_{-0.59}$	$20.9^{+3.0}_{-3.0}$	$21.4^{+2.7}_{-2.7}$	$27.4^{+2.6}_{-2.6}$
240951	*4932*	*e*	$38.9^{+1.4}_{-1.4}$	$24.6^{+0.22}_{-0.22}$	$84.9^{+0.46}_{-0.46}$	$1.3^{+0.2}_{-0.2}$	$39.3^{+1.4}_{-1.4}$	$47.5^{+13.7}_{-13.7}$
99-00 e^+p								
248207	**32134**	**e**	$\mathbf{32.6^{+1.3}_{-1.3}}$	$\mathbf{32.2^{+0.25}_{-0.25}}$	$\mathbf{-31.3^{+0.30}_{-0.30}}$	$\mathbf{42.9^{+4.1}_{-4.1}}$	$\mathbf{44.3^{+3.0}_{-3.0}}$	$\mathbf{47.5^{+13.7}_{-13.7}}$
251415	43944	μ	$22.6^{+2.5}_{-2.0}$	$18.8^{+0.20}_{-0.20}$	$174.0^{+0.13}_{-0.13}$	$16.0^{+3.6}_{-3.6}$	$12.8^{+2.0}_{-1.7}$	$57.4^{+0.0}_{-0.0}$
252020	**30485**	**e**	$\mathbf{25.6^{+1.2}_{-1.2}}$	$\mathbf{110.2^{+0.25}_{-0.25}}$	$\mathbf{-94.5^{+0.30}_{-0.30}}$	$\mathbf{40.0^{+3.3}_{-2.6}}$	$\mathbf{38.3^{+2.6}_{-2.6}}$	$\mathbf{20.0^{+1.1}_{-1.1}}$
253700	90241	μ	$168.1^{+18.8}_{-15.4}$	$17.0^{+0.20}_{-0.20}$	$-106.1^{+0.13}_{-0.13}$	$16.6^{+2.6}_{-2.6}$	$175.7^{+18.8}_{-15.4}$	$67.3^{+10.1}_{-10.1}$
264453	*69912*	*e*	$19.1^{+0.7}_{-0.7}$	$17.1^{+0.22}_{-0.22}$	$-109.5^{+0.59}_{-0.59}$	< 2	$19.1^{+0.7}_{-0.7}$	< 5
266336	**4126**	**μ**	$\mathbf{19.8^{+0.6}_{-0.6}}$	$\mathbf{67.3^{+0.39}_{-0.39}}$	$\mathbf{102.0^{+0.06}_{-0.06}}$	$\mathbf{50.4^{+3.9}_{-3.9}}$	$\mathbf{67.2^{+3.8}_{-3.8}}$	$\mathbf{20.0^{+1.1}_{-1.1}}$
268338	**70014**	**e**	$\mathbf{32.2^{+1.2}_{-1.2}}$	$\mathbf{29.7^{+0.22}_{-0.22}}$	$\mathbf{-125.1^{+0.46}_{-0.46}}$	$\mathbf{47.2^{+3.4}_{-3.4}}$	$\mathbf{67.6^{+3.2}_{-3.2}}$	< 5
269672	66918	e	$17.3^{+0.7}_{-0.7}$	$18.7^{+0.22}_{-0.22}$	$14.5^{+0.59}_{-0.59}$	$3.7^{+0.7}_{-0.7}$	$19.9^{+0.9}_{-0.9}$	< 5
270132	73115	μ	$12.5^{+8.1}_{-3.7}$	$18.4^{+0.20}_{-0.20}$	$48.6^{+0.13}_{-0.13}$	$21.9^{+4.5}_{-4.5}$	$29.2^{+7.7}_{-4.9}$	$68.0^{+0.0}_{-0.0}$
274357	6157	e	$40.0^{+1.3}_{-1.3}$	$14.9^{+0.22}_{-0.22}$	$15.9^{+0.59}_{-0.59}$	$3.4^{+0.6}_{-0.6}$	$40.7^{+1.4}_{-1.4}$	$5.3^{+0.1}_{-0.1}$
275991	**29613**	**e**	$\mathbf{37.5^{+1.5}_{-1.5}}$	$\mathbf{41.7^{+0.25}_{-0.25}}$	$\mathbf{-53.5^{+0.30}_{-0.30}}$	$\mathbf{27.9^{+1.9}_{-1.9}}$	$\mathbf{40.6^{+1.4}_{-1.4}}$	$\mathbf{5.2^{+0.0}_{-0.0}}$
276220	76295	e	$52.1^{+2.0}_{-2.0}$	$54.9^{+0.25}_{-0.25}$	$18.3^{+0.30}_{-0.30}$	< 2	$52.1^{+2.0}_{-2.0}$	< 5
277699	91265	e	$28.2^{+1.0}_{-1.0}$	$17.6^{+0.22}_{-0.22}$	$-144.0^{+0.59}_{-0.59}$	$2.9^{+1.5}_{-1.5}$	$25.4^{+1.9}_{-1.9}$	< 5

Table 5.8.: Kinematical properties of the events selected in HERA-1 data in the electron and muon channels. New events with respect to the paper are *emphasised*. Events with $P_T^X > 25$ GeV are highlighted in bold font. Kinematics for previously published events are derived with the reanalysis and shown for comparison.
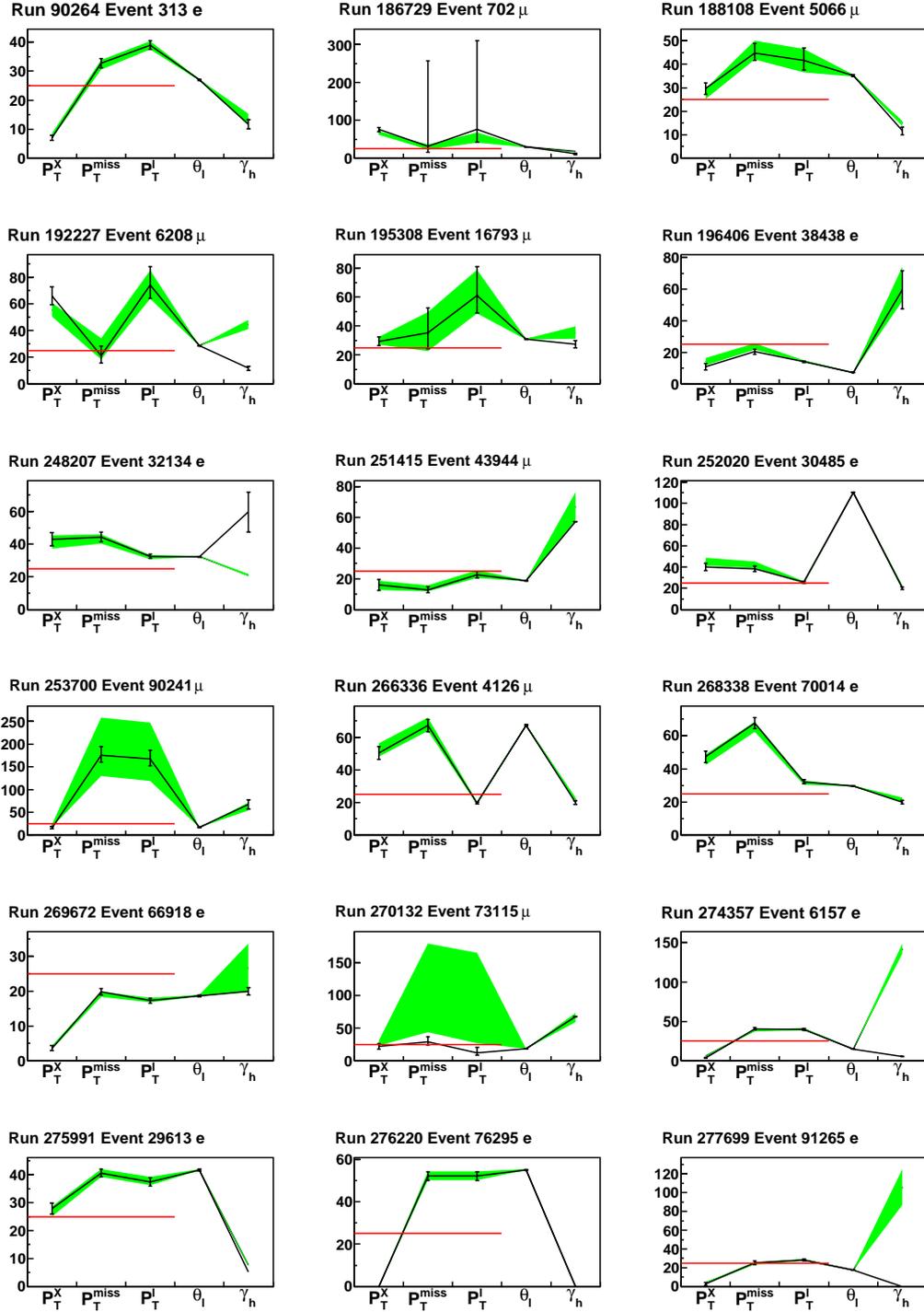
Figure 5.19.: Comparative parallel coordinates plots for the previously published HERA-I candidates. The original kinematics are shown as green shaded band. The new kinematics are shown as black line with error bars. Arranged along the abscissa are P_T^X, P_T^{miss}, P_T^l, θ_l and γ_h for each event. The ordinate has units GeV for the transverse momenta and degrees for the polar angles. The endpoints of the error bands and error bars pass through the total error on the respective kinematic value. The red line shows the $P_T > 25$ GeV threshold which is shown to highlight eventual migrations in this region.

6. Analysis of Isolated Tau Leptons

6.1. Introduction

The observation of events with isolated electrons and muons in events with missing transverse momentum motivates the search for events with tau leptons and missing transverse momentum. In addition, some BSM scenarios favour effects related to the third generation which lead to the idea that the observed electron and muon events may come from leptonic decays of tau leptons which would be produced with an anomalous rate due to new physics processes. It is therefore interesting to search for unambigous signatures of isolated tau events and to compare with the findings in the electron and muon channels.

Tau leptons decay before penetrating the active region of the detector. They are therefore detected via their decay products. Table 6.1 recalls the main decay modes of tau leptons. Leptonic tau decays with a total branching ratio of about 35% are identified by the final state electron or muon. In this case tau events cannot be distinguished from electron and muon events. This topology is therefore included in the analysis presented in the previous chapter and hadronic tau decays are used to unambigously tag tau events.

Tau leptons have been measured at HERA in elastic tau pair production [14]. Using the HERA-1 data sample, H1 has observed 30 $\tau^+\tau^-$ candidate events with 27.1 ± 4.1 expected from the SM of which 60% come from the $\gamma\gamma \to \tau^+\tau^-$ signal process. The tau identification algorithm used in that analysis is adapted to low P_T tau leptons. Other algorithms were used in a higher P_T regime, for instance in searches for lepton flavour violation [53] and for doubly charged Higgs bosons $H^{\pm\pm}$ [54]. The tau identification algorithm used here focuses on 1-prong hadronic tau decays (50% of the tau branching ratio) and is similar to the one developed for the previously published analysis of events with isolated tau leptons and missing transverse momentum based on HERA-1 data [44, 47].

The selection is performed searching for narrow jets corresponding to hadronic 1-prong tau decays in events with significant missing transverse momentum. In this chapter this selection

Mode		Branching Ratio
leptonic	$\mu\bar{\nu}_\mu\nu_\tau$	17%
	$e\bar{\nu}_e\nu_\tau$	18%
hadronic	1-prong	50%
	3-prong	15%

Table 6.1.: Summary of tau lepton decay modes [16]. This analysis covers hadronic 1-prong tau decays.

Tau Channel Selection	
Inclusive CC	$P_T^{\mathrm{calo}} > 12$ GeV
	$P_T^{\mathrm{had}} > 12$ GeV
	$P_T^{\mathrm{miss}} > 12$ GeV
	$\delta^{\mathrm{miss}} > 5$ GeV
	$V_{ap}/V_p < 0.5$
	$(< 0.15$ if $P_T^{\mathrm{miss}} < 25$ GeV$)$
Narrow Jets	$P_T^{jet} > 7$ GeV
	$20° < \theta^{jet} < 120°$
	$R^{jet} < 0.12$
	$N_{tracks}^{jet} \geq 1$, $\max(P_T^{track}) > 5$ GeV
Isolation	$D_{em,\mu,jet} > 1.0$
Acoplanarity	$\Delta\varphi(\tau, X) < 170°$ if $P_T^X > 5$ GeV
1-Prong Jets	$N_{tracks}^{Djet<1.0} = 1$
Final Selection	$N_{\mathrm{DTNV}}^{D_{track}<0.3} = 1$

Table 6.2.: Summary of selection requirements for the tau channel. Tau jet candidates are searched in an inclusive CC sample. Narrow jets depend mainly on calorimetric measurements. 1-Prong tau jets add strict tracking requirements and depend on good track description. The details of the selection are described in the text.

is described together with control analyses defined such that the background description and the quality of the signal simulation are demonstrated.

6.2. CC Selection

The selection of events with significant missing transverse momentum corresponds to the selection of inclusive CC events and is summarised in Tab. 6.2. The P_T^{miss} distribution for all HERA-2 data is shown in Fig. 6.1. The data and the SM prediction agree well for e^+p and e^-p collisions. More control distributions can be found in Appendix A.2. Figure 6.2 shows the CC event yield versus integrated luminosity for the analysed HERA-2 data period. The expected increase in the CC cross section for e^-p data with respect to e^+p data is visible. The event yield is otherwise constant in time and no systematic effect related to special running conditions is observed.

Inclusive CC Sample (2003-06, $e^{\pm}p$)
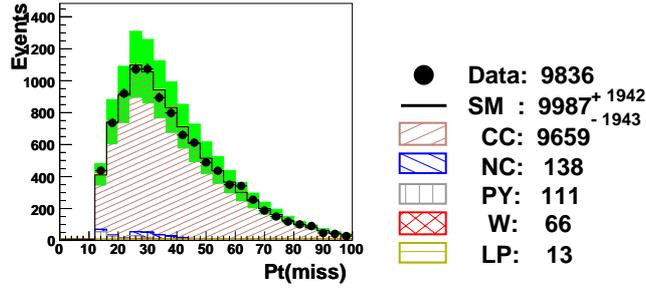
Figure 6.1.: Missing transverse momentum in the CC inclusive selection for all HERA-2 data.
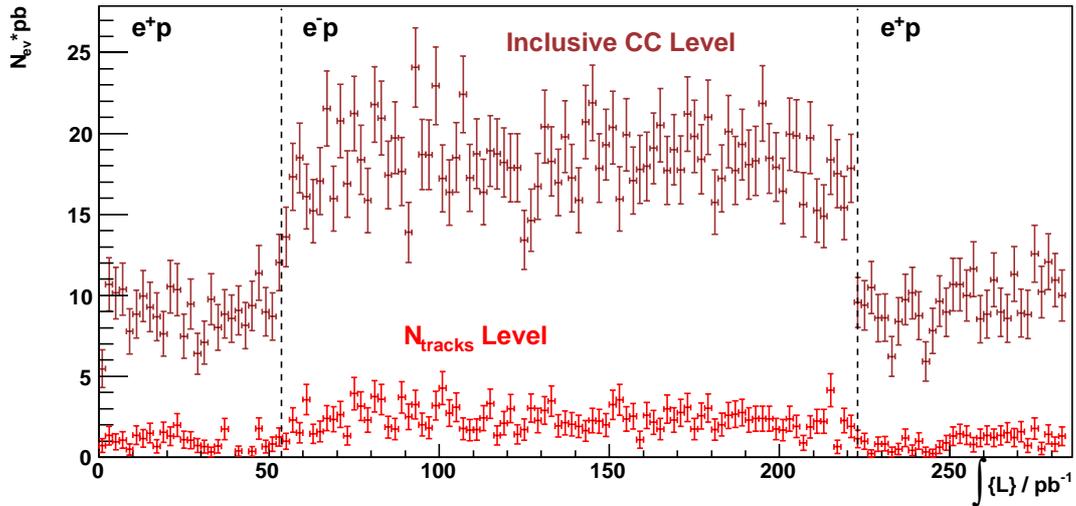
Figure 6.2.: Event yields in intermediate steps of the tau channel selection for the analysed HERA-2 data. Shown is the number of events selected per 1 pb^{-1} in the inclusive CC sample and events in the same sample with narrow jets (labelled "N_{tracks}"). The increase in the CC cross section from e^+p to e^-p running is well visible. Apart from this expected feature the distributions are compatible with a flat yield over the whole sample within the statistical errors (shown).

73

6.3. Identification of Tau Jets

Tau jet candidates are based on jets found in the hadronic final state. The tau jet four-vector is attributed to the four-vector of the tau lepton and subtracted from the hadronic final state to obtain the transverse momentum of the remaining hadronic system X:

$$\vec{P}_T^X = \vec{P}_T^{had} - \vec{P}_T^\tau.$$

The requirements for tau jet candidates are summarised in Tab. 6.2 and are discussed in the following.

Narrow Jet Selection

- $P_T^{jet} > 7$ GeV. The transverse momentum of the jet is required to be above 7 GeV to reduce the amount of QCD jets misidentified as tau jet candidates.

- $20° < \theta_{jet} < 120°$. For polar angles $\theta_{jet} < 20°$ the track multiplicity cannot be reliably measured. At polar angles $\theta_{jet} > 120°$ the scattered electron from NC events is expected and sometimes falsely identified as jet.

- The jet radius has to be $R_{jet} < 0.12$. The jet radius is used as measure for the collimation of the jet and is calculated as

$$R_{jet} = \frac{1}{E_{jet}} \sum_h E_h \sqrt{\Delta\eta(\text{jet},h)^2 + \Delta\varphi(\text{jet},h)^2}$$

  where E_{jet} is the jet energy and E_h is the energy of jet daughter hadronic final state particle h.

- $N_{\text{track}}^{P_T > 5\,\text{GeV}} > 0$. There has to be at least one charged jet daughter hadronic final state particle with an associated central track that has a transverse momentum $P_T^{\text{track}} > 5$ GeV. This ensures the typical "prong" signature of a stiff track. If there are several suitable tracks, the track with the highest transverse momentum is defined as the tau track. Forward tracks are also counted to serve as isolation veto, but may not be the tau track (hence, a tau candidate is not accepted if it has only forward tracks).

- $D_{e,\mu,\text{jet}} > 1.0$ in the $\eta\varphi$-plane. The distance of the tau candidates to identified muons, electromagnetic particles and other jets in the event is ensured to avoid any overlap of the final states.

- Containment of the tau candidate in the LAr calorimeter fiducial volume is tested by extrapolating the track helix from the measured vertex to the calorimeter face taking into account the track charge and the octagonal LAr face geometry. The azimuthal impact angle of the tau track is required to be at least 2° from cracks between LAr calorimeter octants. The impact z-position z_{imp} of the tau track on the LAr calorimeter face is required to be at least 2 cm from the center of cracks between the LAr calorimeter barrels at $z = [-211.14, -151.43, -64.63, 110.12]$ cm and outside the range $15 < z_{imp} < 30$ cm of the CB2-CB3 crack which is impacted at steep angles.
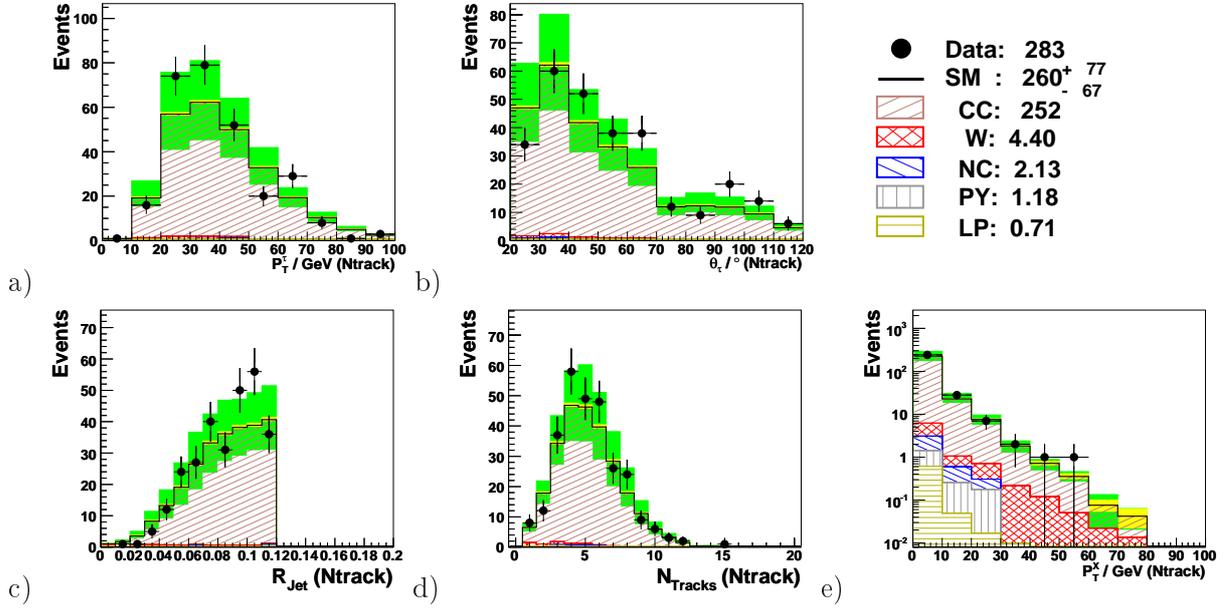
Figure 6.3.: Distributions of the 2003-06 e^+p data with narrow tau jet candidates in the inclusive CC sample.
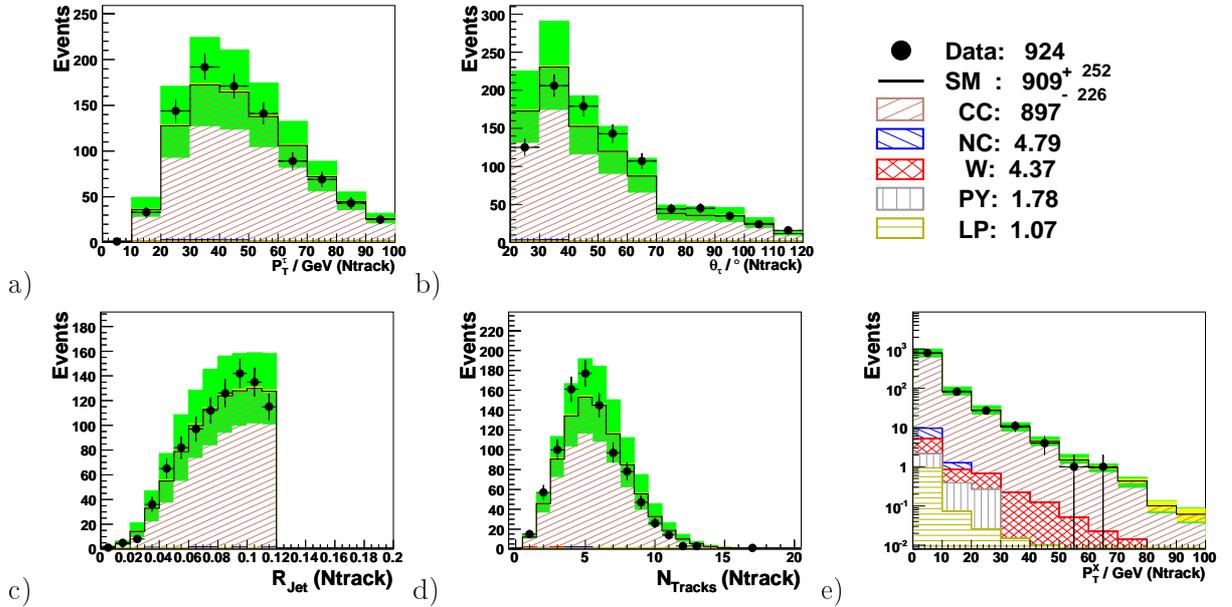
Figure 6.4.: Distributions of the 2004-06 e^-p data with narrow tau jet candidates in the inclusive CC sample.

1-Prong Tau Jets (as in Paper) in CC (2003-06, e^+p)

a)

b)
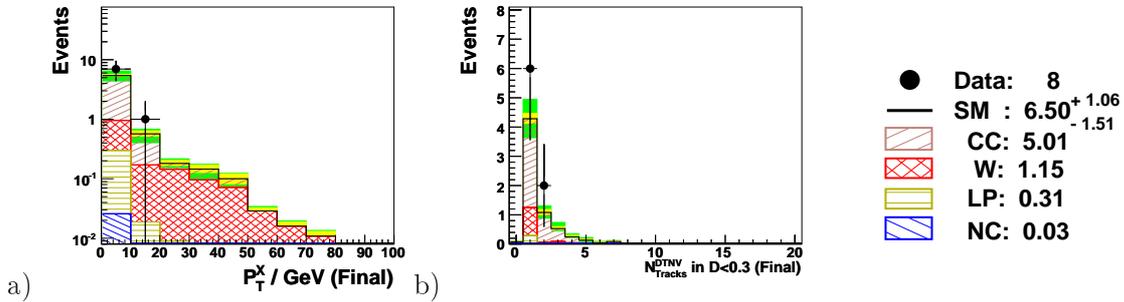
Figure 6.5.: Distribution of 1-prong tau jets (as in the HERA-1 paper) selected in the 2003-06 e^+p CC sample. a) No candidates are observed at $P_T^X > 25$ GeV. b) The distribution of non-vertex-fitted tracks around the tau track $N_{\mathrm{DTNV}}^{D<0.3}$ shows that the signal is expected for $N_{\mathrm{DTNV}}^{D<0.3} = 1$.

1-Prong Tau Jets (as in Paper) in CC (2004-06, e^-p)

a)

b)
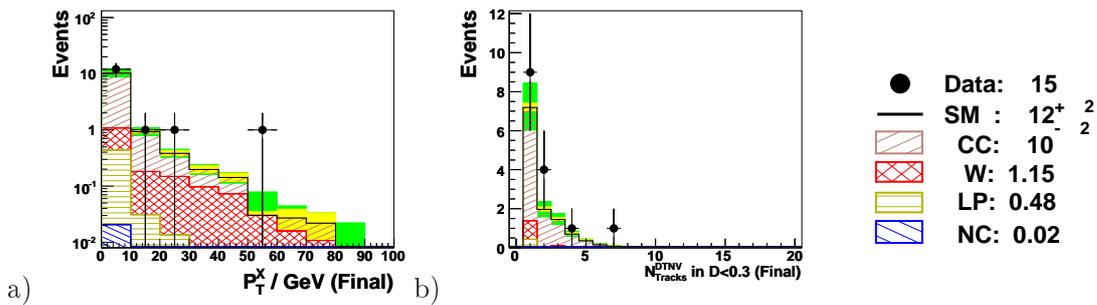
Figure 6.6.: Distribution of 1-prong tau jets (as in the HERA-1 paper) selected in the 2004-06 e^-p CC sample. One candidate is observed at $P_T^X > 25$ GeV.

- $\Delta\varphi(jet, X) < 170°$. This rejects back-to-back topologies such as the $e - jet$ system in NC and the $jet - jet$ system of dijets in photoproduction. The cut is only applied if there is significant hadronic activity with $P_T^X > 5$ GeV.

Only one tau jet candidate per event is allowed to suppress tau pair production. Figures 6.3 and 6.4 show the description of narrow jets in the CC sample. The data are still dominated by CC events, with a signal contribution of only $\sim 2\%$. This sample is shown as CC control sample in Tab. 6.4. The transverse momentum (a), polar angle (b) and radius (c) of narrow jets is described within the errors. The number of selected tracks N_{tracks} (d) in the isolation cone of radius 1.0 in the $\eta\varphi$-plane around the jet axis is also described. This is the most important feature of this selection step. P_T^X (e) is well described to high values. Figure 6.2 also shows the event yield of events with such narrow jets over the whole HERA-2 data (Labelled "Ntracks", red). No statistically significant deviations from flat distributions within the e^-p and e^+p samples are visible. This gives confidence that the background from CC events is well estimated, and the selected tracks are well described.

$$P_T^{miss} = 59 \text{ GeV} \qquad P_T^\tau = 14 \text{ GeV} \qquad P_T^X = 51 \text{ GeV}$$
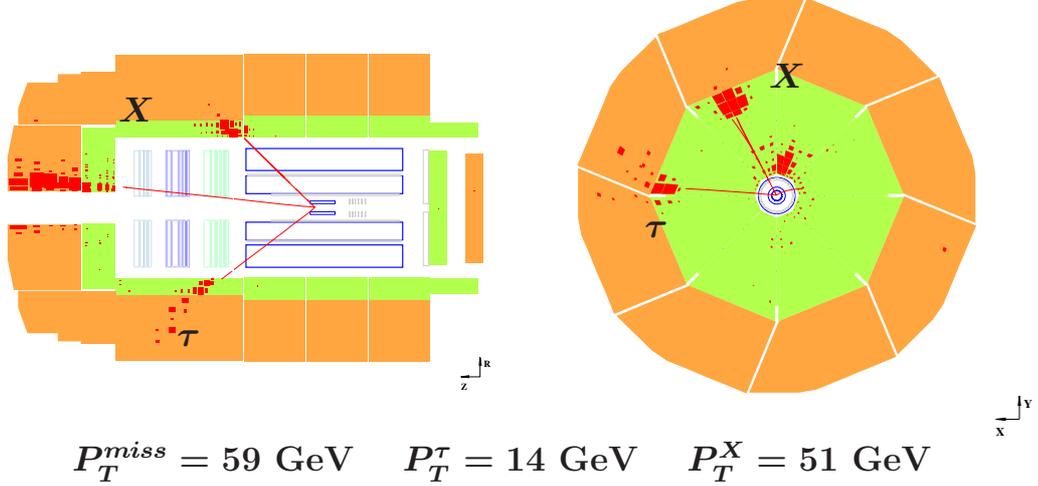
Figure 6.7.: The selected tau candidate at high P_T^X.

1-Prong Jets

1-Prong jets are selected from narrow jets by the following requirement:

- $N_{\text{track}}^{D<1.0} = 1$. There must be exactly one selected track within a distance of $D_{\text{track}} < 1.0\,\eta\varphi$ around the **jet** axis. This is the tau track previously defined. Forward tracks in the isolation cone are also counted to act as isolation veto.

Figures 6.5 and 6.6 show the distribution of events with 1-prong jets in the inclusive CC sample. This selection corresponds to the final selection of the HERA-1 paper. The P_T^X distributions show good agreement with the SM at this level (a). One event is selected at high P_T^X in the e^-p data, in a region where 0.55 ± 0.1 events are predicted by the SM. This event is shown in Fig. 6.7.

Final Selection

The scanning of the events obtained after the previous selection step revealed that a large fraction of tau candidates have more than one non-vertex-fitted track close to the selected track. The distribution of the number of non-vertex-fitted tracks in a cone of $D < 0.3$ in the $\eta\varphi$-plane around the tau track $N_{\text{DTNV}}^{D<0.3}$ are shown in Figs. 6.5b and 6.6b. Figure 6.8 shows an example of an event with $N_{\text{DTNV}}^{D<0.3} > 1$ selected in the previous selection step. Most of the signal (hadronically decaying tau leptons from W decays) is contained in the bin $N_{\text{DTNV}}^{D<0.3} = 1$. In order to improve the purity, a final requirement is applied:
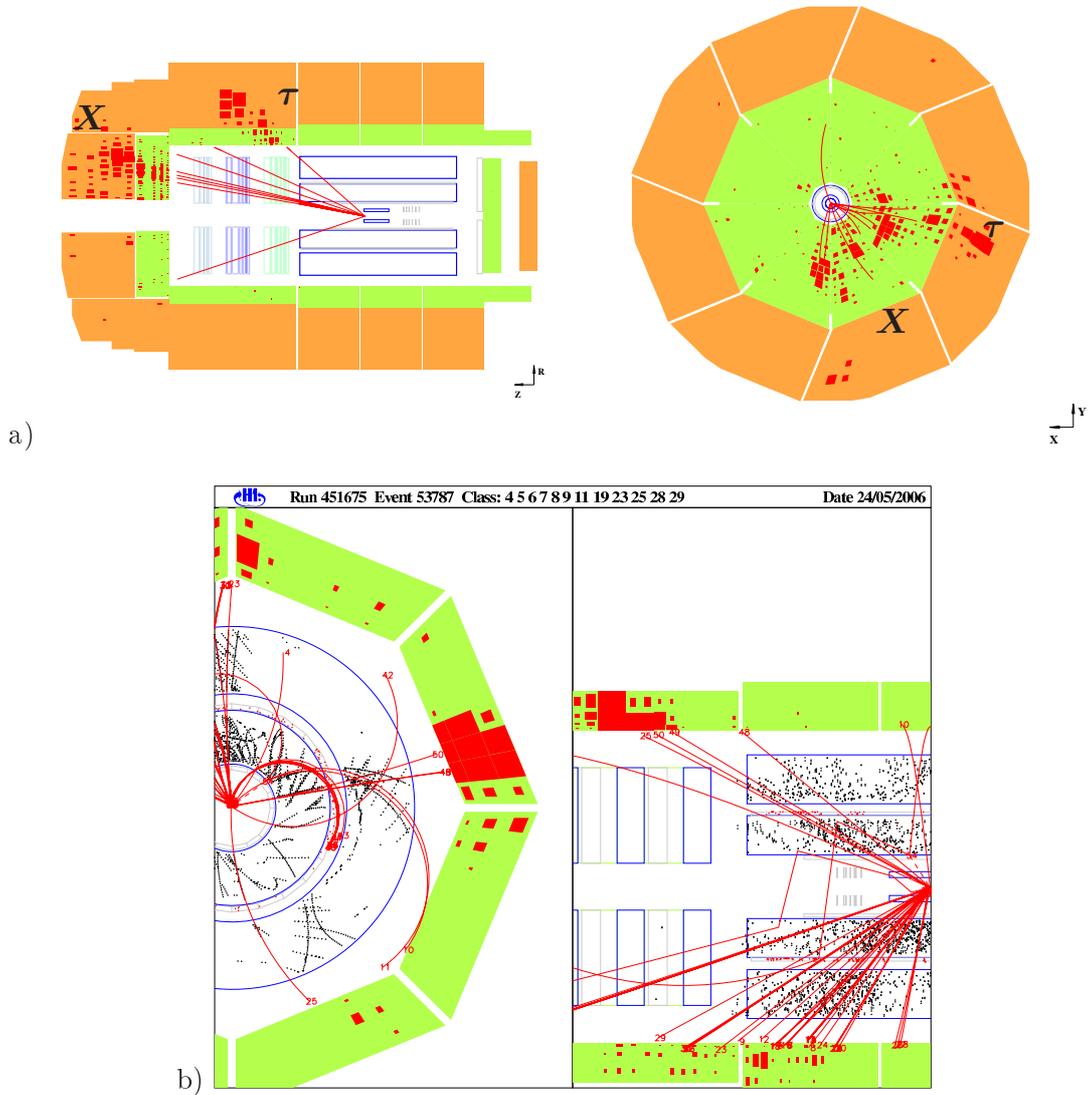
Figure 6.8.: Example for a preliminary tau candidate selected in HERA-2 data [15] using the cuts from the HERA-1 paper [14]. a) Using selected tracks only, the tau jet candidate is well isolated. b) The close-up showing all vertex-fitted tracks demonstrates that the selected track (vertex-fitted track no. 48) has two more low-quality tracks close to it (no. 48, 50), spoiling the isolation.

- $N_{\text{DTNV}}^{D<0.3} = 1$. The number of non-vertex-fitted tracks within a distance of $D_{\text{DTNV}} <$ $0.3\,\eta\varphi$ around the **tau track** axis must be exactly one. Only non-vertex-fitted tracks with a length greater than 10 cm, and their start- and endpoints in the cone defined by $D_{\text{DTNV}} < 0.3\,\eta\varphi$ are considered to ensure that only reasonably well measured tracks roughly parallel to the selected track are counted.

This cut alone reduces the signal expectation in total by about 15%, while the background is reduced by 60% for all data, leading to a significant improvement in the signal to noise ratio of the final sample.

6.4. Results

Table 6.3 shows the observed data compared to the SM expectation over the whole P_T^X range and for $P_T^X > 25$ GeV obtained using the full HERA data, corresponding to an integrated luminosity of 398 pb^{-1}. Figure 6.9 shows the distributions of P_T^{miss}, P_T^X and the kinematics of the tau jet candidate, P_T^τ and θ_τ, for the final selection. The signal and background expectation is indicated for every bin. The errors given are statistical and systematic uncertainties added in quadrature.

The overall agreement with the SM is very good with a total of 18 events observed for 20 ± 3 predicted. The SM prediction is dominated by the irreducible CC background, with a total signal contribution of only 22%. One event is observed at high $P_T^X > 25$ GeV where 1.4 ± 0.4 are expected. In this region, the signal contribution to the SM expectation is 74%. The selected event can therefore be interpreted as $W \to \tau\nu_\tau$, $\tau \hookrightarrow h\bar{\nu}_\tau$.

A cross check of the results in the electron and muon channels using the tau channel is impeded by the much lower efficiency. While 10.4 ± 1.6 signal events are expected in the combined electron and muon channels at $P_T^X > 25$ GeV in the full HERA data (see Tab. 5.5), only 1.04 ± 0.16 events are expected in the same region in the tau channel, which is one order of magnitude less. If 8 of the 15 events observed in the total e^+p data in the electron and muon channel at $P_T^X > 25$ GeV are attributed to an excess over the total SM prediction of 6.8 ± 0.9 events, an excess of less than one event is expected in the tau channel.
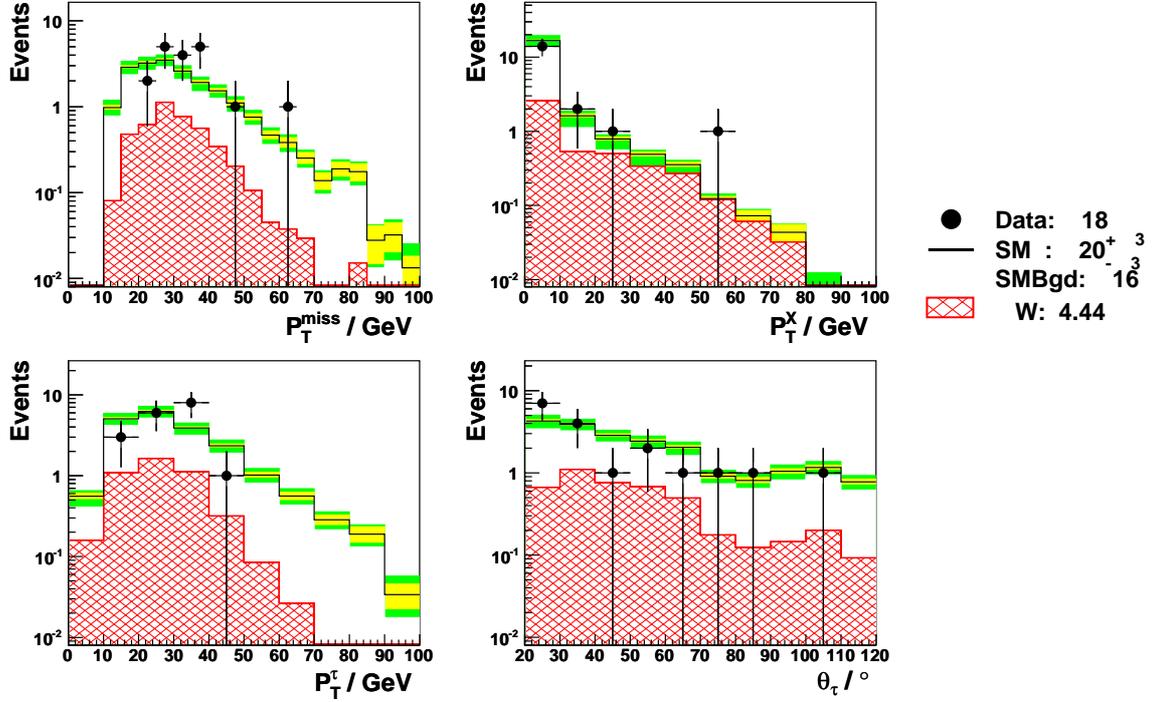
Figure 6.9.: Results in the tau channel for the full HERA data set. The selected data (points) are compared to the SM prediction (open histogram). The statistical and systematic uncertainties added in quadrature are shown as green band (containing the statistical error as yellow band). The signal component is shown as red hatched histogram.

Tau Channel		H1 Data	SM Expectation	SM Signal	Other SM Processes
1994-2006 e^+p	All P_T^X	8	10.69 $^{+1.59}_{-1.68}$	2.34 $^{+0.35}_{-0.36}$	8.35 $^{+1.23}_{-1.33}$
214.6 pb^{-1}	$P_T^X > 25$ GeV	0	0.69 $^{+0.09}_{-0.30}$	0.54 $^{+0.08}_{-0.09}$	0.14 $^{+0.01}_{-0.21}$
1998-2006 e^-p	All P_T^X	10	9.40 $^{+1.45}_{-1.55}$	2.01 $^{+0.31}_{-0.31}$	7.39 $^{+1.14}_{-1.24}$
183.6 pb^{-1}	$P_T^X > 25$ GeV	1	0.69 $^{+0.10}_{-0.21}$	0.47 $^{+0.07}_{-0.08}$	0.21 $^{+0.02}_{-0.14}$
1994-2006 $e^\pm p$	All P_T^X	18	20.18 $^{+3.02}_{-3.26}$	4.44 $^{+0.67}_{-0.68}$	15.74 $^{+2.35}_{-2.58}$
398.2 pb^{-1}	$P_T^X > 25$ GeV	1	1.40 $^{+0.18}_{-0.53}$	1.04 $^{+0.16}_{-0.16}$	0.36 $^{+0.02}_{-0.37}$

Table 6.3.: Results in the tau channel for all e^+p data, e^-p data and the full HERA data.

Period	Run	Event	P_T^l / GeV	θ_l / $^\circ$	φ_l / $^\circ$	P_T^X / GeV	P_T^{miss} / GeV
94-97 e^+p	226096	700	38.7 ± 13.2	22.7 ± 0.22	-12.0 ± 0.46	4.1 ± 0.5	39.6 ± 13.1
98-99 e^-p	269752	26130	26.4 ± 4.5	20.5 ± 0.22	81.6 ± 0.46	0.3 ± 0.1	26.1 ± 4.5
99-00 e^+p	275073	99491	22.4 ± 7.0	33.1 ± 0.25	99.1 ± 0.30	4.1 ± 0.4	26.1 ± 7.0
03-04 e^+p	359926	8460	38.3 ± 5.0	20.3 ± 0.22	-149.6 ± 0.46	0.2 ± 0.1	38.2 ± 5.0
	391464	198	36.7 ± 7.7	23.5 ± 0.22	-71.6 ± 0.46	0.5 ± 0.2	36.3 ± 7.7
04-06 e^-p	408237	72126	29.0 ± 6.5	105.8 ± 0.25	90.9 ± 0.30	7.3 ± 0.9	34.2 ± 6.4
	413245	56825	33.0 ± 6.4	49.0 ± 0.25	67.6 ± 0.30	1.3 ± 0.3	31.7 ± 6.4
	414321	20053	38.4 ± 7.1	28.4 ± 0.22	145.3 ± 0.46	3.0 ± 0.7	38.2 ± 7.1
	414431	30536	21.1 ± 8.6	38.6 ± 0.25	-13.1 ± 0.30	9.6 ± 1.2	29.4 ± 8.6
	417955	**105857**	**14.4 ± 7.5**	**35.2 ± 0.25**	**3.5 ± 0.30**	**61.3 ± 4.5**	**68.0 ± 6.2**
	429534	168739	13.2 ± 4.9	70.0 ± 0.25	-62.6 ± 0.30	24.5 ± 3.0	21.3 ± 2.6
	432747	3734	25.8 ± 8.0	82.6 ± 0.25	3.4 ± 0.30	1.4 ± 0.4	27.1 ± 8.0
	452520	13568	38.2 ± 11.7	35.3 ± 0.25	120.9 ± 0.30	0.6 ± 0.2	38.6 ± 11.7
	466285	58750	13.8 ± 5.4	28.9 ± 0.22	-159.3 ± 0.46	13.1 ± 1.6	24.6 ± 5.1
06 e^+p	476252	73465	34.0 ± 9.6	50.3 ± 0.25	90.3 ± 0.30	1.8 ± 0.3	32.5 ± 9.6
	478423	118795	36.1 ± 11.4	65.2 ± 0.25	107.9 ± 0.30	8.2 ± 1.2	26.5 ± 10.5
	474329	44930	25.1 ± 15.7	50.6 ± 0.25	142.3 ± 0.30	15.9 ± 1.4	29.4 ± 12.9
	483023	126100	47.8 ± 6.0	23.4 ± 0.22	128.3 ± 0.46	0.4 ± 0.1	48.0 ± 6.0

Figure 6.10.: Kinematics of selected events with tau candidate jets in all HERA data. The errors are obtained by propagating the experimental resolutions to the reconstructed variables.

6.5. Study of Narrow Hadronic Jets

The inclusive NC sample provides the sample of QCD jets with the highest statistics. To test the misidentification of QCD jets as tau jets, clean 1-prong tau jet candidates are selected in the inclusive NC sample (section A.1). Figures 6.11 and 6.12 show distributions in this selection. The kinematics, P_T (a) and θ (b), of the tau-like jet are well described. The jet radius is well described including the contribution from misidentified electrons visible at the lowest jet radii (c). Also the kinematics, P_T (d) and θ (e), of the tau track are well described. This gives confidence that the misidentification of QCD jets as tau jets is under control for the calorimeter measurement and the track measurement within the errors. Tau jet candidates in CC and photoproduction are shown directly in the background control samples.

Clean 1-prong Tau Candidates in NC, 2003-06 $\mathbf{e^+p}$

a)

b)

Data: 481
SM : $575^{+\ 91}_{-\ 102}$
NC: 571
LP: 3.81
W: 0.07
PY: 0.00

c)

d)

e)
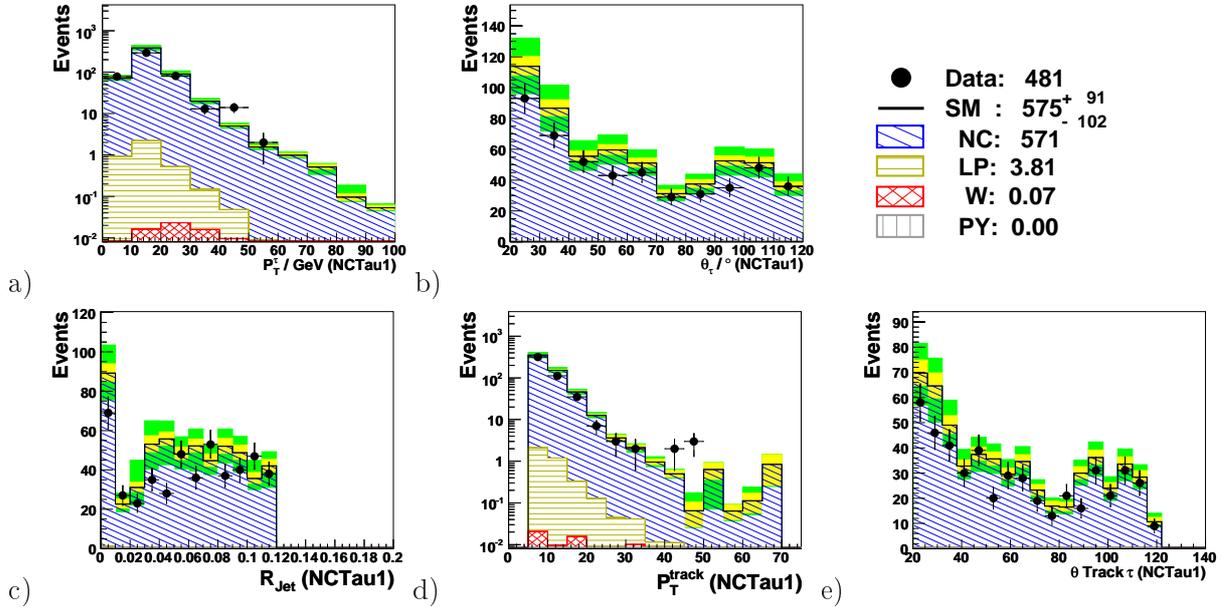
Figure 6.11.: Clean 1-prong tau jet candidates in the 2003-06 e^+p inclusive NC sample.

Clean 1-prong Tau Candidates in NC, 2004-06 $\mathbf{e^-p}$

a)

b)

Data: 639
SM : $851^{+\ 139}_{-\ 156}$
NC: 845
LP: 5.77
W: 0.07
PY: 0.00

c)

d)

e)
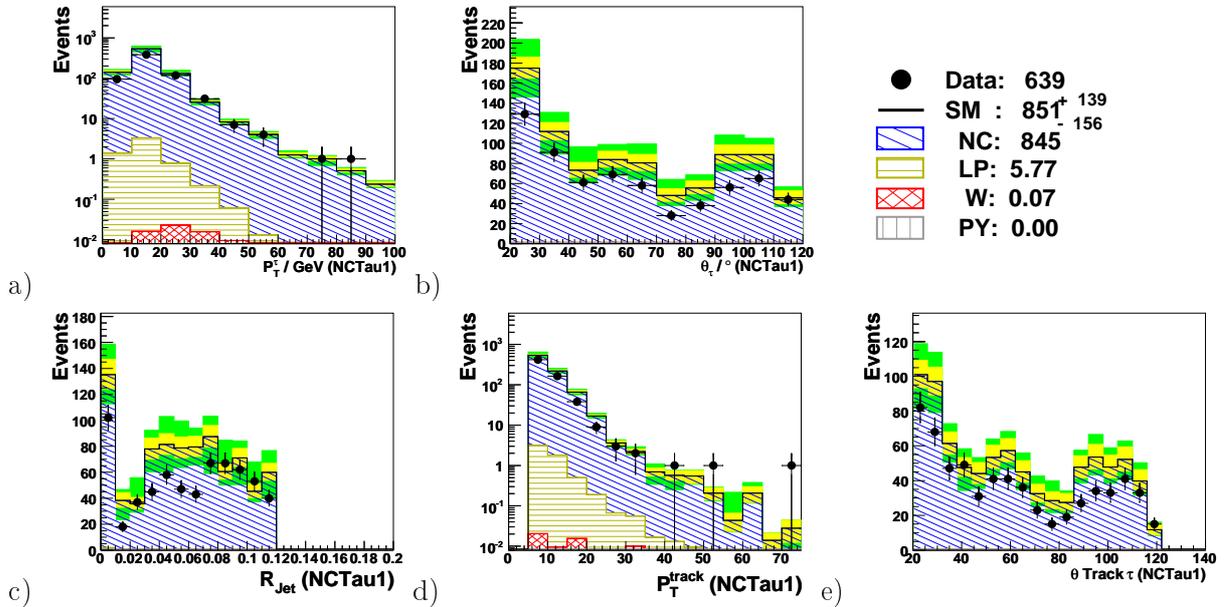
Figure 6.12.: Clean 1-prong tau-jet candidates in the 2004-06 e^-p inclusive NC sample.

Tau Channel	Control Samples $P_T^{\text{calo}} > 12$ GeV		
	CC	**NC**	**Photoproduction**
	$\delta^{\text{miss}} > 5$ GeV	$\delta^{\text{miss}} < 8$ GeV	$\delta^{\text{miss}} > 5$ GeV
	$P_T^{\text{had}} > 12$ GeV	$Q_e^2 > 90 \text{GeV}^2$	$Q_e^2 < 1$ GeV^2
	$P_T^{\text{miss}} > 12$ GeV	$E_e > 11$ GeV	$V_{ap}/V_p > 0.15$
	$V_{ap}/V_p < 0.5$ (<0.15 if		
	$P_T^{\text{miss}} < 25$ GeV)		
Tau Jet Selection	narrow	1-prong	1-prong
(isolated+acoplanar)	yes	no	no
Data (04-06, e^-p)	924	157	164
Total SM	909 ± 240	137 ± 30	142 ± 40
	(98% CC)	(96% NC)	(67% γP)

Table 6.4.: Selection requirements for the tau channel CC, NC and photoproduction background control samples. The number of selected events compared to the SM expectation is shown exemplary for the 2004-06 e^-p data. The strictest possible tau jet defnition is used while keeping the statistical significance of the sample high.

6.6. Background Studies

6.6.1. NC Enriched Sample

NC events may enter the final selection if the jet or the electron are misidentified as tau jet and fake missing transverse momentum is measured in the event. To check the NC background in the phase space of the final selection, 1-prong tau candidates without isolation and acoplanarity requirements were selected in the inclusive NC sample in the $P_T^{\text{calo}} > 12$ GeV phase space. Figures 6.13 and 6.14 show the distribution of the events selected in that sample in the 2003-06 e^-p and 2003-06 e^+p data. The transverse momentum (a) and pseudorapidity (b) of the candidates are well described. This gives confidence that the NC background is well under control. If the full requirements for the tau candidates are applied, the NC background is very effectively suppressed. In the whole HERA-2 data 4 clean 1-prong candidates are selected for 3.8 ± 1 expected from the SM.

6.6.2. Photoproduction Enriched Sample

Photoproduction events may enter the sample if false missing transverse momentum is measured and QCD jets are misidentifed as tau jets. This background should be well under control because its total cross section is large, but not very well known. The inclusive photoproduction sample at $P_T^{\text{calo}} > 12$ GeV is described in appendix A.3. Figures 6.15 and 6.16 show

1-prong Tau Candidates in NC at $P_T^{\mathrm{calo}} > 12$ GeV, (2003-06, $\mathbf{e^+ p}$)

a)

b)
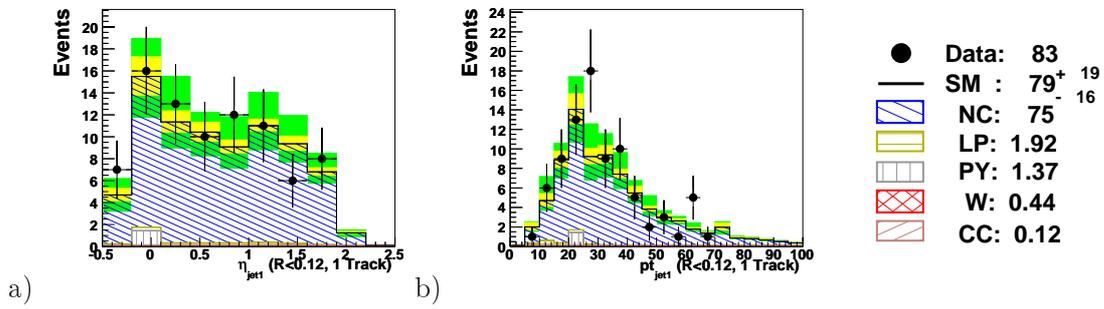
Figure 6.13.: 1-prong tau jet candidates in the 2003-06 $e^+ p$ NC sample at $P_T^{\mathrm{calo}} > 12$ GeV. Isolation and acoplanarity are not required.

1-prong Tau Candidates in NC at $P_T^{\mathrm{calo}} > 12$ GeV (2004-06, $\mathbf{e^- p}$)

a)

b)
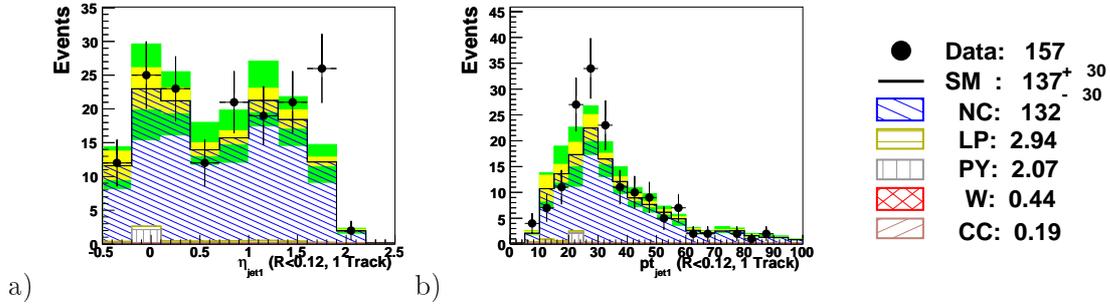
Figure 6.14.: 1-prong tau jet candidates in the 2004-06 $e^- p$ NC sample at $P_T^{\mathrm{calo}} > 12$ GeV. Isolation and acoplanarity are not required.

1-prong Tau Jet Candidates in γP at $P_T^{calo} > 12$ GeV (2003-06, $\mathbf{e^+p}$)

a)   b)

Data: 111
SM : 88^{+32}_{-22}
PY: 63
NC: 15
CC: 7.83
W: 1.07
LP: 1.00
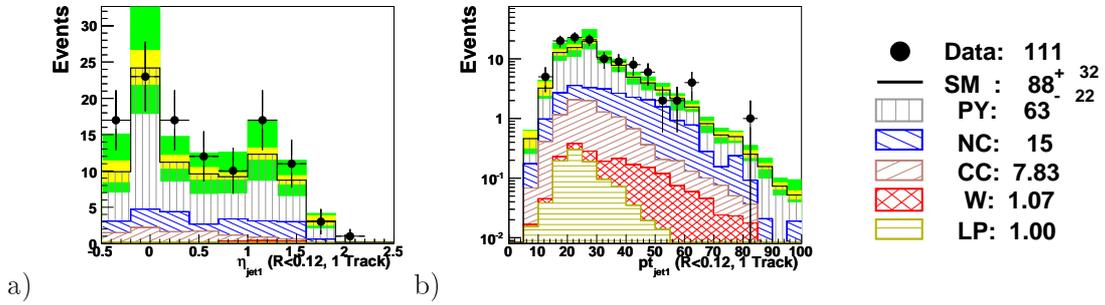
Figure 6.15.: 1-prong tau-jet candidates in the 2003-06 e^+p photoproduction sample at $P_T^{calo} > 12$ GeV.

1-prong Tau Jet Candidates in γP at $P_T^{calo} > 12$ GeV (2004-06, $\mathbf{e^-p}$)

a)   b)

Data: 164
SM : 142^{+49}_{-35}
PY: 96
NC: 23
CC: 21
LP: 1.52
W: 1.06
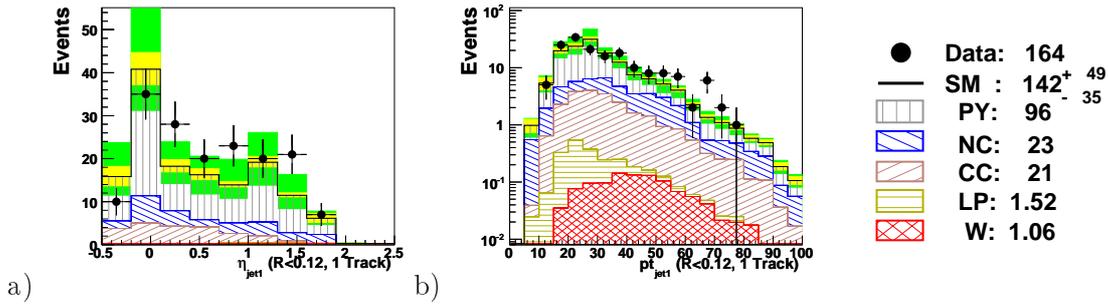
Figure 6.16.: 1-prong tau-jet candidates in the 2004-06 e^-p photoproduction sample at $P_T^{calo} > 12$ GeV.

the pseudorapidity distribution of non-isolated 1-prong tau jet candidates in this sample for the 2003-06 e^+p and 2004-06 e^-p data, respectively. In both periods, the distribution is well described. Selecting isolated, clean 1-prong tau jets in the sample yields only 4 events for 5.5 expected from the SM in the 2004-06 e^-p data. This gives confidence that the inclusive photoproduction contribution to the background is well predicted and can be effectively suppressed.

Tau Channel – HERA-1 Reanalysis

Previously published results [14]

1994-2000 $e^{\pm}$ 115.2 pb^{-1}		H1 Data	SM Expectation	SM Signal	Other SM Processes
Tau	All P_T^X	6	9.9 $^{+2.5}_{-3.6}$	0.89 $^{+0.15}_{-0.26}$	9.0 $^{+2.5}_{-3.6}$
	$P_T^X > 25$ GeV	0	0.39 $^{+0.09}_{-0.11}$	0.20 $^{+0.04}_{-0.05}$	0.19 $^{+0.08}_{-0.10}$

This Reanalysis

1994-2000 $e^{\pm}p$ 115.9 pb^{-1}		H1 Data	SM Expectation	SM Signal	Other SM Processes
Tau	All P_T^X	6	8.69 $^{+1.56}_{-1.51}$	0.80 $^{+0.12}_{-0.12}$	7.89 $^{+1.44}_{-1.39}$
(Previous Cuts)	$P_T^X > 25$ GeV	0	0.33 $^{+0.05}_{-0.04}$	0.18 $^{+0.03}_{-0.03}$	0.14 $^{+0.02}_{-0.02}$

Table 6.5.: Comparison of HERA-1 data selected in HERA-1 paper and the pre-final selection step in the new analysis corresponding to a reanalysis. The results agree within the errors. The SM expectation for signal and background are slightly lower in the reanalysis due to stricter preselection requirements.

6.7. Reanalysis of HERA-1 Data

Because of the additional cut with respect to the previous publication, the HERA-1 data had to be reanalysed also in the tau channel to get the full result for all HERA data. Also the preselection requirements (chapter 4) are tighter than those used for HERA-1 to cope with the higher non-ep-background in the HERA-2 data. Preselection requirements like the topological background finders have to be applied consistently for all data. Table 6.5 shows the results published in the HERA-1 paper [14] (top) compared to the results in the equivalent phase space of the reanalysis (bottom). The SM expectation for signal and background is slightly lower in the reanalysis due to the stricter preselection requirements. The SM predictions agree within the errors and the same events are selected in the data.

7. Summary

Events with rare topologies constitute an ideal tool to search for new physics effects. Spectacular events with isolated electrons, muons or tau leptons and missing transverse momentum are measured in e^+p and e^-p collisions at HERA and compared to the SM prediction. In the SM framework, such events are produced predominantly from single W production, with a cross section of the order of 1 pb. In this thesis, a total integrated luminosity of about 400 pb^{-1} is used to investigate this event topology. The analysis covers the data taken at HERA by the H1 experiment until mid-November 2006.

The observation of an excess at the 3σ level of events which contain in addition a prominent hadronic jet has been reported from HERA-1 data, predominantly collected in e^+p collisions. The events continue to be measured in excess of the SM prediction at HERA-2 in e^+p collisions in a data sample corresponding to a similar luminosity as the HERA-1 data. In e^-p collisions, for a total luminosity similar to the e^+p sample, a good agreement with the SM prediction is observed overall. Events with tau leptons have been searched for and a good purity achieved for events with large P_T^X, but no significant excess is observed. More data will be collected in e^+p collisions until the end of the HERA programme at high energy in March 2007.

If the discrepancy between e^+p and e^-p samples is attributed to a statistical fluctuation, the W production cross section in ep collisions can be measured with a statistical precision of 15%. The measurement can be done differentially as a function of P_T^X and θ_l. This measurement is currently ongoing and will be finalised using the full HERA data [55].

A possible interpretation of the excess at high P_T^X is the production of single *top*-quarks [56]. The leptonic and hadronic signatures from that process have been analysed and limits have been set which are competitive to limits on anomalous *top* production set at other colliders [8, 9, 10, 11, 12]. However, this hypothesis cannot explain the asymmetry between e^+p and e^-p collisions.

This asymmetry could be explained by the existence of a new particle N with fermion number $F = 0$ coupling to an electron-quark vertex. If such a particle had a high mass m_N it would have to be produced at large $x = m_N^2/s$. In this region the parton density of valence quarks in the proton is much larger than the density of sea quarks, hence the production cross section for such a particle is much larger in e^+p running than in e^-p running. For example, in the framework of R-parity violating supersymmetry, such particles could be resonantly produced *stop*-squarks, or *sbottom*-squarks produced in the t-channel [57].

At present the ZEUS experiment does not confirm the excess observed by H1. The ZEUS analysis was performed in a more restricted phase space, at $17° < \theta_e < 86°$ and $17° < \theta_\mu < 115°$. Studies that were done comparing the analyses in both experiments have shown the signal efficiencies to be comparable in the region at high P_T^X [5]. Most of the events observed by H1 at high P_T^X fall into the phase space which is common for the two experiments. A combination of the two analyses in a common phase space is in progress and will be used to

qualify the significance of an excess or to extract a precise measurement of single W production at HERA.

A. Inclusive Selections

A.1. NC

NC in DIS is the process with the lowest background and simultaneous highest cross section at HERA. An inclusive NC sample is used for many purposes throughout this thesis. The sample is selected utilising the selection used for the inclusive NC cross section measurement [51]. In summary the cuts are:

- $\delta^{\mathrm{miss}} < 8$ GeV to reject CC and photoproduction background.

- $E_e > 11$ GeV .

- $Q_e^2 > 90$ GeV^2 to select electrons in the LAr calorimeter.

- Electron isolated from the HFS.

- Selected electron track with electron cluster dca < 12 cm.

- Electron measured in fiducial volume of LAr calorimeter (not in cracks).

Figure A.1 shows distributions of the NC inclusive sample exemplary for the 2004-06 $e^- p$ data. The Q_e^2 distribution (a) shows that the electron is well measured in all regions of the LAr calorimeter. Mismeasured missing transverse momentum P_T^{miss} (b) in the event is described well up to high values. The P_T (c), η (d) and radius (e) of the first jet is well described. If present, a second jet is also well described (f-h).

A.2. CC

The selection of inclusive CC events follows largely the selection used in the inclusive CC cross section measurement [51]:

- $P_T^{\mathrm{calo}} > 12$ GeV.

- $P_T^{\mathrm{miss}} > 12$ GeV.

- $P_T^X > 12$ GeV.

- $\delta^{\mathrm{miss}} > 5$ GeV.

- $0.03 < y_h < 0.85$ and $Q_h^2 > 100$ GeV. These cuts are used in the inclusive CC cross section measurement to ensure high trigger efficiency and good kinematic resolution, because the hadron method has to be used to reconstruct the DIS kinematics (see Tab. 1.2). In this analysis the cuts ensure a well measured hadronic final state.

- $V_{ap}/V_p < 0.5$. This cut suppresses NC and photoproduction events in which transverse momentum is missing due to fluctuation in the detector response or undetected particles. If $P_T^{\mathrm{miss}} < 25$ GeV it is required that $V_{ap}/V_p < 0.15$ to ensure the missing transverse momentum is real. With respect to the CC cross section measurement, the V_{ap}/V_p requirements are relaxed in order to increase acceptance of topologies with a tau jet and a hadronic system with a high transverse momentum. In the ANOTOP template for such topologies, the tau candidate and its neutrino are expected to recoil against the b-jet giving rise to a higher V_{ap}/V_p value.

Figures A.2 and A.3 show the distributions of the data selected in the inclusive CC sample for the 2003-06 e^+p and 2004-06 e^-p period, respectively. The missing transverse momentum is well described up to high values (a). The $(E - P_z)$ balance is well described down to small values (b). The vertex z-position distributions show no conspicuous tails hinting at remaining non-ep-background in the sample (c). The transverse momentum (d), pseudorapidity (e) and radius (f) of the jet with the highest transverse momentum in the event are also well described.

The charged current cross section σ_{CC} depends linearly on the longitudinal electron beam polarisation P_e like

$$\sigma_{CC} = \sigma_{CC}^0 (1 + q \cdot P_e),$$

where σ_{CC}^0 is the unpolarised CC cross section and q is the charge of the electron beam. Polarisation values for Monte Carlo events can be drawn randomly from the applicable polarisation profile shown in Fig. 2.2 for each event.

CC events with more than one jet are a potentially large background to events with a tau jet and a large hadronic system. Figures A.4 and A.5 show the distributions of CC events with a second jet for the 2003-06 e^+p and 2004-06 e^-p data, respectively. The transverse momentum (a), pseudorapidity (b) and radius (c) of second jets are well described, giving confidence that this background is correctly estimated.

A.3. Photoproduction

Photoproduction events may enter the phase space $P_T^{\mathrm{calo}} > 12$ GeV due to mismeasured missing energy. In this phase space inclusive photoproduction events are selected by applying the following requirements:

- $Q_e^2 < 1$ GeV^2 to ensure the scattered electron is not detected.

- $(E - P_z) < 50$ GeV to suppress remaining NC events.

- $V_{ap}/V_p > 0.15$ to suppress CC events.

- $0 < x_h < 1$ and $0.1 < y_h < 0.9$ to ensure the hadronic final state is well measured using the hadron method (see Tab. 1.2).

Figures A.6 and A.7 show that the pseudorapidity (a) and radius (b) of the first jet are well described. If a second jet is present, its pseudorapidity is also well described (c). The azimuthal angle difference of the two jets $\Delta\phi(jet1, jet2)$ is well described also in the region $\Delta\phi_{12} < 160°$ where it extends due to the missing transverse momentum (d).

Inclusive NC (2004-06, e^-p)

Dijets in NC
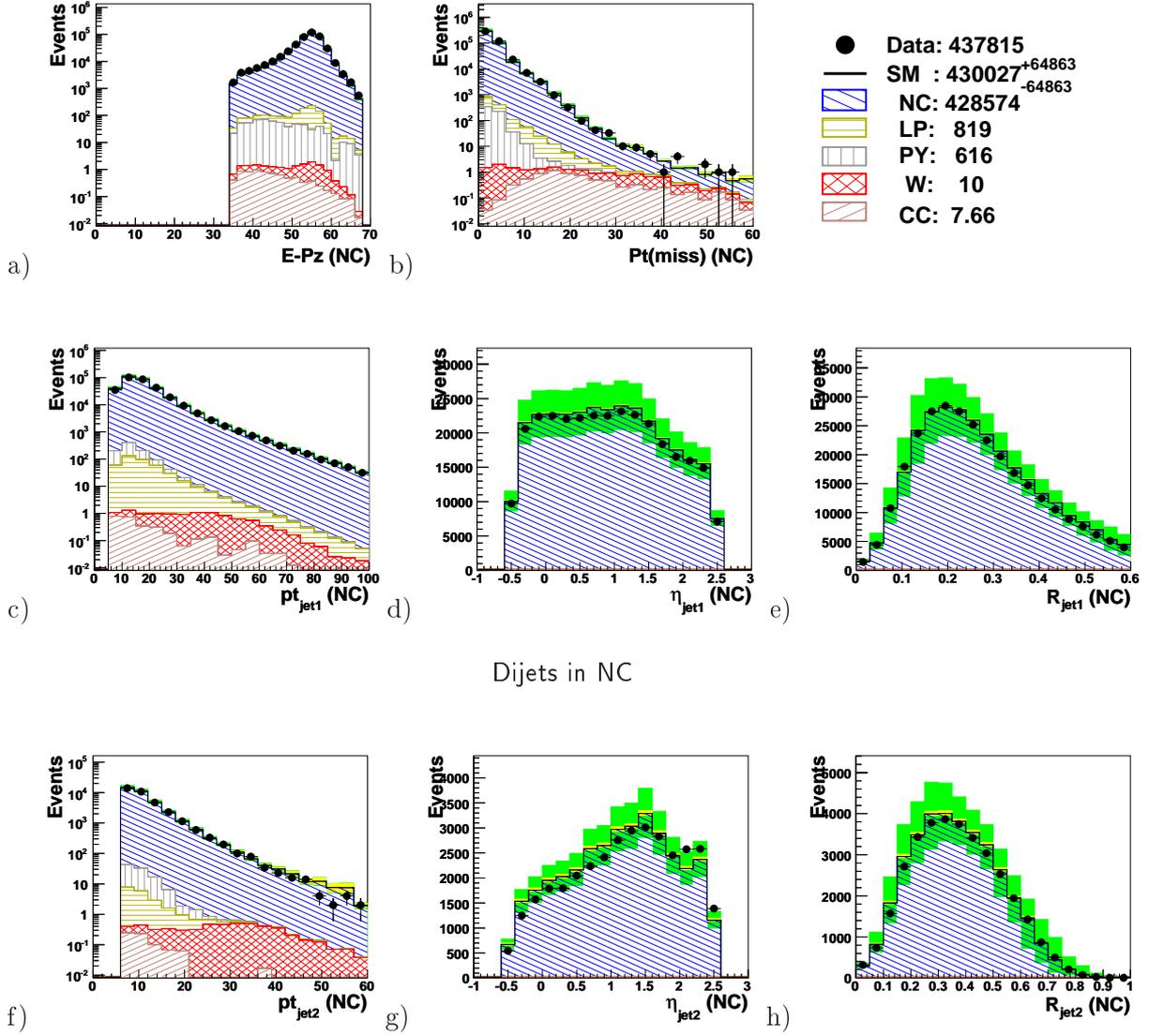
Figure A.1.: Distributions of the 2004-06 e^-p data selected in the inclusive NC samples (a-e) and NC dijet samples (f-h).

Inclusive CC (2003-06, $\mathbf{e}^+\mathbf{p}$)
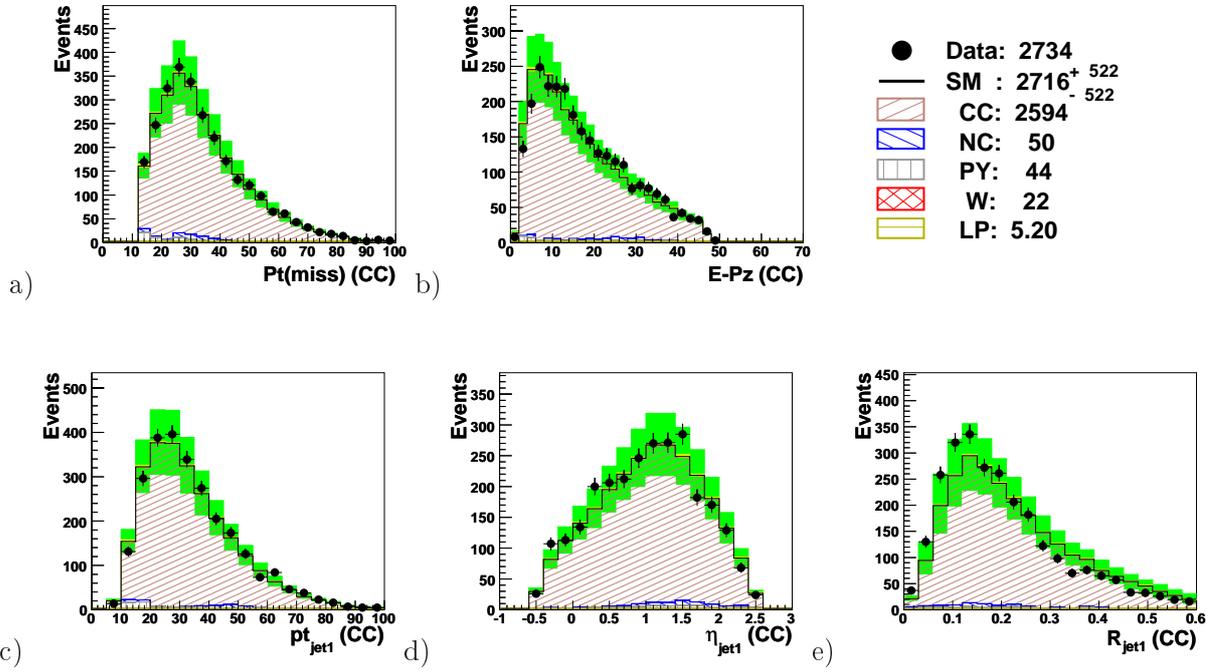
Figure A.2.: Distributions of the 2003-06 e^+p data selected in the inclusive CC sample.

Inclusive CC (2004-06, $\mathbf{e}^-\mathbf{p}$)
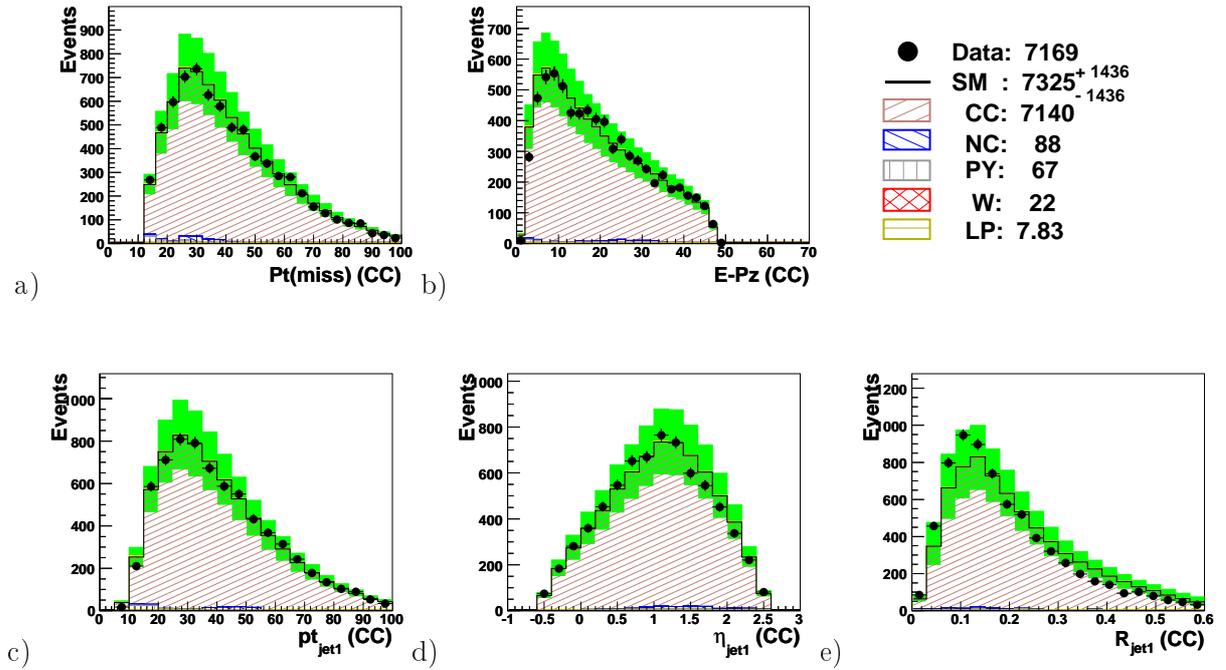
Figure A.3.: Distributions of the 2004-06 e^-p data selected in the inclusive CC sample.

CC Dijets (2003-06, e^+p)

Data: 375
SM : $389^{+\ 71}_{-\ 71}$
CC: 352
NC: 23
PY: 11
W: 3.12
LP: 0.54

a)   b)
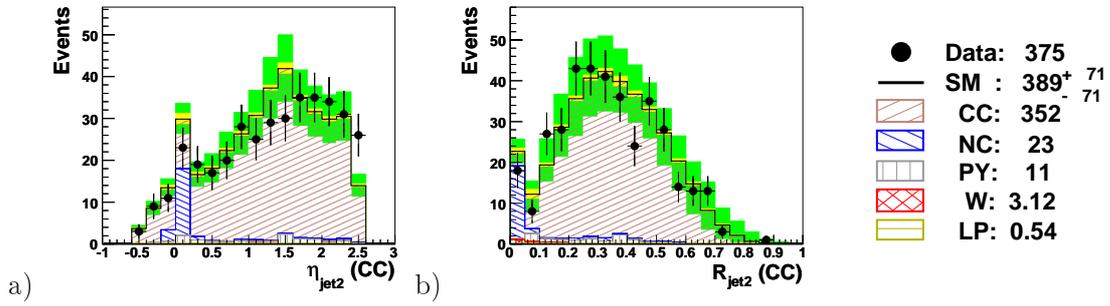
Figure A.4.: Distributions of the 2003-06 e^+p data of in inclusive CC sample with a second jet.

CC Dijets (2004-06, e^-p)

Data: 1033
SM : $1141^{+\ 217}_{-\ 217}$
CC: 1078
NC: 42
PY: 16
W: 3.10
LP: 0.80

a)   b)
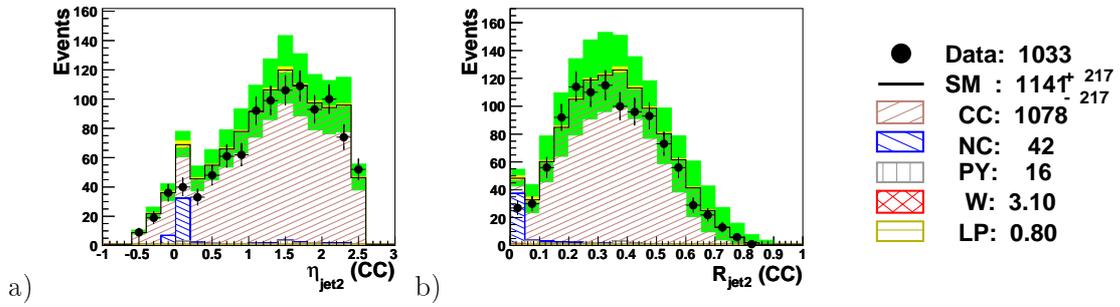
Figure A.5.: Distributions of the 2004-06 e^-p data in an inclusive CC sample with a second jet.

96

Jets in Photoproduction at $P_T^{\mathrm{calo}} > 12$ GeV (2003-06, $\mathbf{e^+p}$)
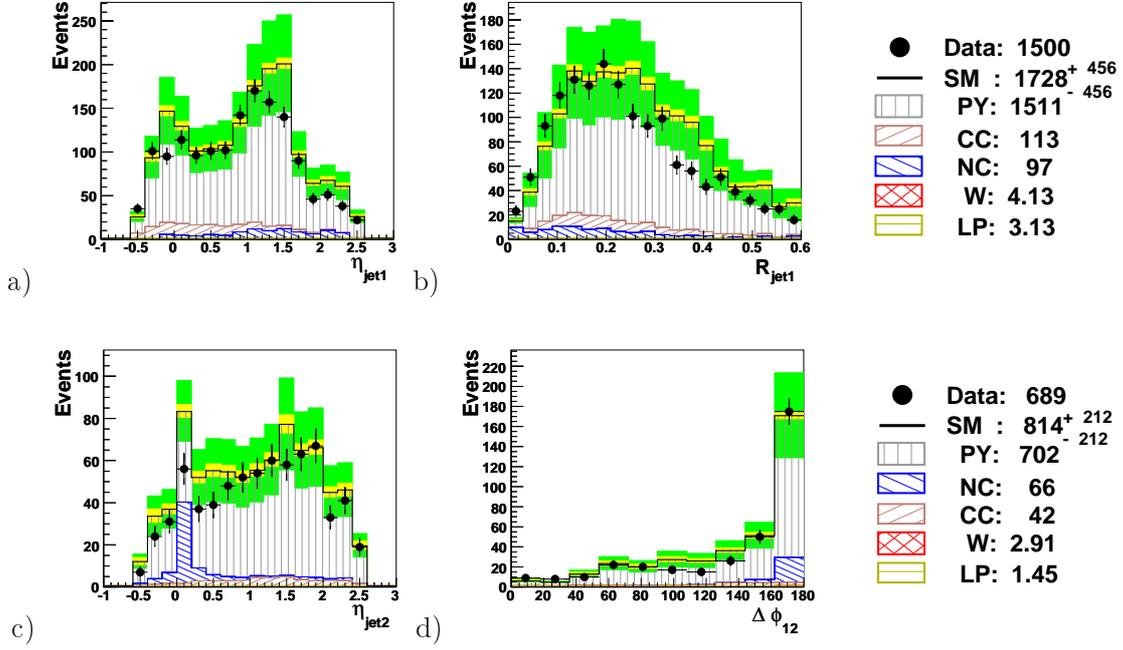
Figure A.6.: Photoproduction control distributions in 2003-06 e^+p data. a)

Jets in Photoproduction at $P_T^{\mathrm{calo}} > 12$ GeV (2004-06, $\mathbf{e^-p}$)
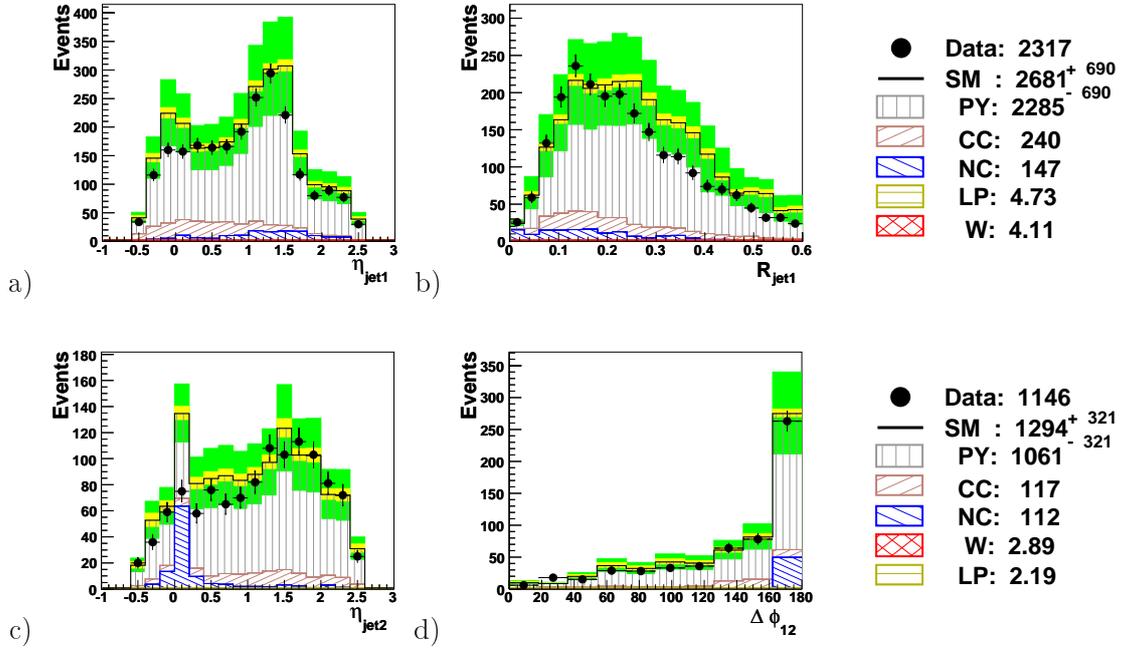
Figure A.7.: Photoproduction control distributions in 2004-06 e^-p data

B. Systematic Uncertainties

The influence of systematic uncertainties on the total predicted rates in the final selections are estimated by rerunning the analysis with a variation of ± 1 standard deviations applied in the Monte Carlo events on the quantity to study. All variations are added in quadrature, where care is taken that the effect on the result has the same direction (increased or decreased expectation) to estimate the full range of the systematic effects. Table B.1 summarises the contributions to the total error from the different sources detailed below. In the lepton and muon channels the total error is dominated by the model uncertainties. In all plots presented in this thesis the uncertainties associated with leptonic and hadronic quantities are included in these errors. In the tau channel, the total error is dominated by the model uncertainties and the uncertainty on the jet radius measurement.

B.1. Reconstruction Uncertainties

B.1.1. Leptonic Quantities

- The uncertainty on central track θ is 3 mrad and on ϕ 1 mrad. They determine the uncertainty on electron and muon angles taken from the associated track.

- The uncertainty on the electromagnetic energy scale is 1% in the central region and 2% in the forward region (taken from Fig. 3.1).

B.1.2. Hadronic Quantities

- The uncertainty on the hadronic energy scale is 2% (taken from Fig. 3.4).

- The uncertainty on the tau jet energy scale is estimated by combining uncertainties on the electromagnetic and hadronic components of the tau jet in quadrature.

- The uncertainties on ϕ and θ angles measured by the hadronic final state are 10 mrad. This applies to the inclusive angles γ_h and ϕ_h, the direction of $\vec{P_T^{\text{miss}}}$ and $\vec{P_T^X}$, and jet angles, including the tau jet angle.

- The relative uncertainty on the variable V_{ap}/V_p is 10%, estimated by comparing different reconstruction methods for V_{ap}/V_p.

- The error on the jet radius R_{jet} is 10%, estimated from R_{jet} distributions in the tau channel control samples.

| Source of Systematic | Abs. error on predicted total SM rate in | |
Uncertainty	Electron and Muon Channel	Tau Channel
Leptonic quantities	$< 1\%$	$< 1\%$
Hadronic quantities	3%	3%
Triggering / Identification	4%	17%
Model	10%	20%
Luminosity	2%	

Table B.1.: Summary of experimental systematic errors. Shown is the size of the effect on the total SM rates (signal + background) predicted by the Monte Carlo in the final selections. The error on tau identification is dominated by the uncertainty on the jet radius of $\pm 10\%$. The model uncertainty is dominated by the uncertainty on the CC cross section.

B.1.3. Triggering and Identification

- The uncertainty on the electron finding efficiency is 3%.

- The uncertainty on muon finding efficiency is 5% for $\theta_\mu > 20°$.

- The uncertainty on the jet radius is 10%, derived by looking at the radius of NC jets without considering any other errors and scaling the jet radius up and down until the description was fully contained in the jet radius error.

- The error on the track reconstruction efficiency is 3%.

- The uncertainty on the muon trigger efficiency is 10% for $\theta_\mu > 20°$.

B.2. Model Uncertainties

The model uncertainties for the SM background processes were estimated by comparison of data and Monte Carlon in the control samples.

- The uncertainty on the W production cross section calculated by EPVEC after applying NLO corrections is 15% [20].

- In the electron and muon channel phase space the model uncertainty on CC and NC cross sections calculated by DJANGO are estimated to 30%.

- In the tau channel phase space the model uncertainty on the CC cross section calculated by RAPGAP is estimated to 20%, and on the NC cross section 15%.

- The uncertainty on the photoproduction cross section calculated by PYTHIA is estimated to 50% in the electron and muon phase space and 30% in the tau channel phase space.

- The uncertainty on the lepton pair production cross section calculated by GRAPE is estimated to 30%.

B.3. Global Uncertainties

- The uncertainty of the luminosity measurement at HERA-2 is 2%.

- The uncertainty on the polarisation measurement is typically 5%. Since the polarisation measurement only influences the CC cross section, it is included in the CC model uncertainty.

List of Figures

List of Tables

References

[1] C. Diaconu, *Isolated Lepton Production at Colliders*, Habilitation, Marseille 2003.

[2] T. Ahmed *et al.*, [H1 Collaboration], DESY preprint 94-248 (1994).

[3] C. Adloff *et al.*, [H1 Collaboration], *Observation of events with an isolated high energy lepton and missing transverse momentum at HERA*, Eur. Phys. J. C **5** (1998) 575 [hep-ex/9806009].

[4] V. Andreev *et al.* [H1 Collaboration], *Isolated Electrons and Muons in Events with Missing Transverse Momentum at HERA*, Phys. Lett. B **561** (2003) 241 [hep-ex/0301030].

[5] H1 Collaboration, *Events with an isolated lepton and missing transverse momentum at HERA*, ICHEP 06 - PRC update H1prelim-06-162.

[6] J. Breitweg *et al.* [ZEUS Collaboration], Phys. Lett. B **471** (2000) 411 [hep-ex/9907023].

[7] S. Chekanov *et al.* [ZEUS Collaboration], Phys. Lett. B **559** (2003) 153 [hep-ex/0302010].

[8] H1 Collaboration., A. Aktas *et al.*, Eur. Phys. J. C33 (2004) 9 , 10/03 [hep-ex/0310032].

[9] ZEUS Collaboration, *Search for single-top production in ep collisions at HERA*, Phys .Lett. B **559** (2003) [hep-ex/0302010].

[10] CDF Collaboration, Phys. Rev. Lett. **80** (1998) 2525.

[11] CDF Collaboration, *Single-Top-Quark Search with 0.7 fb^{-1}*, CDF note 8185.

[12] L3 Collaboration, *Search for Single Top Production at LEP*, Phys. Lett. B, Vol **549** (2002) pp. 290-300 [hep-ex/0210041].

[13] S. Chekanov *et al.* [ZEUS Collaboration], Phys. Lett. B **583** (2004) 41 [hep-ex/0311028].

[14] A. Aktas *et al.* [H1 Collaboration], *Tau Production in* ep *Collisions* , Eur. Phys. J. C. **4** 06 [hep-ex/0604022].

[15] H1 Collaboration, *Search for events with tau leptons in ep collisions at HERA*, H1prelim-06-064.

[16] W.-M. Yao *et al.* [Particle Data Group], J. Phys. G **33**, 1 (2006).

[17] U. Baur, J. A. M. Vermaseren and D. Zeppenfeld, Nucl. Phys. B **375** (1992) 3.

[18] C. Diaconu *et al.*, *H1EPVEC - W$^{\pm}$ and Z Production Monte Carlo Generator Based on EPVEC*, CPPM Marseille (1999).

[19] K.-P. Diener, C. Schwanenberger and M. Spira , Eur. Phys. J. C **25** (2002) 405 [hep-ph/0203269];
P. Nason, R. Rückl and M. Spira, J. Phys. G **25** (1999) 1434 [hep-ph/9902296];
M. Spira, Proc. of the Workshop "Monte Carlo Generators for HERA Physics" (1991), Eds. A. T. Doyle, G. Grindhammer, G. Ingelman, H. Jung, p. 623 [hep-ph/9905469].

[20] K.-P. Diener, C. Schwanenberger and M. Spira, *Photoproduction of W Bosons at HERA: Reweighting Method for Implementing QCD Corrections in Monte Carlo Programs*, [hep-ex/0302040].

[21] D. South, *Events with Isolated Leptons and Missing Transverse Momentum in e^+p Collisions at HERA*, Dissertation, Univ. of Manchester 2003.

[22] PYTHIA 5.7, T. Sjöstrand, Comput. Phys. Commun. **82** (1994) 74.

[23] ANOTOP, E. Perez.

[24] E. E. Boos *et al.*, [hep-ph/9503280].

[25] F. Jacquet and A. Blondel, *Proceedings of the study of an* ep *facility for Europe*, ed. U. Amaldi, 79/48 (1979) 391.

[26] DJANGO 2.1, G. A. Schüler and H. Spiesberger, Proc. of the Workshop "Physics at HERA" (1991), Eds. W. Buchmüller and G. Ingelman., Vol. 3, p. 1419.

[27] H. Jung, Comput. Phys. Commun. **86** (1995) 147, RAPGAP program manual (1998)http://www-h1.desy.de/~jung/RAPGAP.html.

[28] A. Aktas *et al.* [H1 Collaboration], Phys. Lett. B **602** (2004) 14-30 [hep-ex/0408044].

[29] T. Abe, *GRAPE 1.1*, Comput. Phys. Commun. **136** (2001) 126 [hep-ph/0012029].

[30] C. Berger and P. Kandel, prepared for the Workshop on Monte Carlo Generators for HERA Physics, Hamburg, 27-30 April 1998.

[31] I. Abt *et al.* [H1 Collaboration], *The H1 Detector at HERA*, Nucl. Instr. and Meth. A **386** (1997) 310 and 348.

[32] B. Andrieu *et al.* [H1 Calorimeter Group], Nucl. Instr. and Meth. A **336** (1993) 460;

[33] B. Andrieu *et al.* [H1 Calorimeter Group], Nucl. Instr. and Meth. A **336** (1993) 499;
B. Andrieu *et al.* [H1 Calorimeter Group], Nucl. Instr. and Meth. A **344** (1994) 492;
B. Andrieu *et al.* [H1 Calorimeter Group], Nucl. Instr. and Meth. A **350** (1994) 57.

[34] R. D. Appuhn *et al.* [H1 SpaCal Group], Nucl. Instr. and Meth. A **386** (1997) 397.

[35] I. R. Kenyon *et al.* [H1 FMD Group], Nucl. Instr. and Meth. A **340** (1994) 304.

[36] GEANT 3, R. Brun *et al.*, CERN-DD/EE/84-1.

[37] H1 OO Group, The H1OO Physics Analysis Project, unpublished;
H1 OO Group, H1OO User Guide, unpublished https://www-h1.desy.de/icas/oop.

[38] R. Brun and F. Rademakers, *ROOT - An Object Oriented Data Analysis Framework*, Proceedings AIHENP'96 Workshop, Lausanne, Sep. 1996, Nucl. Inst. & Meth. in Phys. Res. A **389** (1997) 81 `http://root.cern.ch/`.

[39] M. Peez *et al.*, *An Energy Flow Algorithm for Hadronic Reconstruction In OO: Hadroo2*, CPPM Marseille, LAL Orsay, H1 note H1-01/05-616;
M.Peez, *Recherche de deviations au–dela du Modele Standard dans les processus de grande energie transverse sur le collisionneur electron-proton HERA*, Dissertation, Universtie Paris-Sud XI (2005).

[40] P. Bruel, *Recherche d'interactions au-del'a du Mod'ele Standard a HERA*, Dissertation, Universtie Paris-Sud XI (1998).

[41] C. Adloff *et al.* [H1 Collaboration], Eur. Phys. J. C **13** (2000) 609 [hep-ex/9908059].

[42] B. Heinemann, *Measurement of Charged Current and Neutral Current Cross Sections in Positron Proton Collisions at $\sqrt{s} \approx 300 GeV^2$*, Dissertation, University of Hamburg (1999).

[43] S. Bentvelsen *et al.*, *Reconstruction of (x, Q^2) and Extraction of Structure Functions in Neutral Current Scattering at HERA*, Proceedings of the workshop Physics at HERA, Vol. 1, eds. W. Buchmueller, G. Ingelman, DESY (1991) 23.

[44] C. Veelken, *Search for Events with Isolated Leptons and Large Missing Transverse Momentum in ep Collisions at HERA*, Dissertation, University of Liverpool (2005).

[45] S. D. Ellis and D. E. Soper, Phys. Rev. D **48** (1993) 3160 [hep-ph/9305266];
S. Catani, Y. L. Dokshitzer, M. H. Seymour and B. R. Webber, Nucl. Phys. B **406** (1993) 187;
C. Adloff *et al.* [H1 Collaboration], Nucl. Phys. B **545** (1999) 3 [hep-ex/9901010].

[46] M. Jacquet *et al.*, *Absolute Hadronic Jet Calibration of the H1 Liquid Argon Calorimeter*, Orsay, Marseille, H1 note H1-IN-571(04/1999).

[47] G. Brandt, *Suche nach isolierten Tau-Leptonen bei HERA*, Diplomarbeit, Univ. of Heidelberg (2003).

[48] A. Pieuchot, J. Marks, C. Vallee, *Pile-Up Energy Detection Using the Liquid Argon Big Tower Timing Information*, Marseille, H1 note h1-0195-423

[49] G. Brandt, H1 note, *in preparation*

[50] C. Veelken, *H1NonepBgFinder - Rejection of Cosmic Muon and Beam-Halo Events in the H1OO Framework*, Liverpool University, H1 note H1-IN-603(09/2002);
E. Chabert *et al.*, *QBGFMAR: An Updated Phan Package for Cosmic and Halo Muon Topological Rejection in High P_T Physics Analysis*, Marseille, H1 note H1-IN556(11/1998).

[51] B. Portheault, *Première mésure des sections efficaces de courant charge et neutre avec le faisceau de positrons polarise a HERA II et analyses QCD- electrofaibles*, Orsay 2005.

[52] A. Inselberg, *n-dimensional graphics, part I–lines and hyperplanes*, Technical Report G320-2711, IBM Los Angeles Scientific Center, IBM Scientific Center, 9045 Lincoln Boulevard, Los Angeles (CA), 900435, 1981.

[53] L. Lindfeld, Dissertation, University of Zürich (2006).

[54] A. Aktas *et al.* [H1 Collaboration], Phys. Lett. B **638** (2006) 432 [hep-ex/0604027]

[55] Y. de Boer, Dissertation, IHEP Moscow, *in preparation*

[56] J. Dingfelder, *Search for Anomalous Production of Single Top Quarks with the H1 Experiment at HERA*, Dissertation, Univ. of Heidelberg 2003.

[57] E. Perez, *private communication*

- All H1 thesis are available at:
  `http://www-h1.desy.de/publications/theses_list.html`

- H1 Preliminary results can be retrieved from:
  `http://www-h1.desy.de/publications/H1preliminary.short_list.html`

Acknowledgements

There are many people to thank for helping me complete this thesis. I will list but a few:

- F. Eisele for providing me with the opportunity to conduct this thesis at DESY.

- J. Stachel for accepting to act as second referee for this thesis.

- C. Diaconu for providing lots of advice, files, legacy code of the electron and muon channels, useful scripts and plane tickets to conferences over the years, and for extensive comments on the draft.

- E. Sauvan for providing help and service on countless analysis aspects, in particular plots 3.1 and 3.4 (or, rather, most of chapter 3 ...).

- D. South for cross checking the results in the electron and muon channel, refereeing the tau channel and comments on the draft.

- H. Meyer for refereeing the tau channel and keeping me updated on latest results in astroparticlephysics and cosmology.

- J. Meyer for scanning incoming isolated leptons and pointing at details like the ones in Fig. 6.8b.

- C. Niehbur for Figs. 4.1b and 5.6, even though they don't show what we all had hoped for.

- O. Behnke for professional comments on the draft.

- Y. de Boer for providing plots 4.2 and teaching me essential Dutch.

- M. Mozer for useful comments on the draft and the rest of the HE group, esp. C. Werner and J. Kessler, for warm welcomes when visiting the home institute in Heidelberg.

- R. Wolf for putting the draft over the edge.